Design and Optimization of Piezoelectric MEMS Vibration Energy Harvesters

By

©Seyedfakhreddin Nabavi, BSc, MSc

A dissertation submitted to the School of Graduate Studies
in partial fulfillment of the requirements for the degree of

Doctor of Philosophy

Faculty of Engineering & Applied Science
Memorial University of Newfoundland

April 2019

St. John's, Newfoundland, Canada

Abstract

Low-power electronic applications are normally powered by batteries, which have to deal with stringent lifetime and size constraints. To enhance operational autonomy, energy harvesting from ambient vibration by micro-electromechanical systems (MEMS) has been identified as a promising solution to this universal problem. In this thesis, multiple configurations for MEMS-based piezoelectric energy harvesters are studied. To enhance their performances, automated design and optimization methodologies with minimum human efforts are proposed. Firstly, the analytic equations to estimate resonant frequency and amplitude of the harvested voltage for two different configurations of unimorph MEMS piezoelectric harvesters (i.e., with and without integration of a proof mass) are presented with their accuracy validated by using finite element method (FEM) simulation and prototype measurement. Thanks to their high accuracy, we use these analytic equations as fitness functions of genetic algorithm (GA), an evolutionary computation method for optimization problems by mimicking biological evolution. By leveraging the micro-fabrication process, we demonstrate that the GA can optimize the mechanical geometry of the prototyped harvester effectively and efficiently, whose peak harvested voltage increases from 310 mV to 1900 mV at the reduced resonant frequency from 886 Hz to 425 Hz with the highest normalized voltage density of 163.88 among the alternatives.

With an intention of promoting uniform stress distribution along the piezoelectric cantilever and providing larger area for placing proof masses, in this thesis a T-shaped cantilever structure with two degrees-of-freedom (DOF) is proposed. Thanks to this special configuration, a considerable amount of stress/strain can be obtained from the tip part of the structure during the vibration, in addition to the anchor region. An analytic model for computing the frequency

response of the proposed structure is derived, and the harvester performance is studied analytically, numerically and experimentally.

The conventional MEMS energy harvesters can only generate voltage disadvantageously in a narrow bandwidth at higher frequencies. Therefore, in this thesis we further propose a piezoelectric MEMS harvester with the capability of vibrating in multiple DOF, whose operational bandwidth is enhanced by taking advantage of both multimodal and nonlinear mechanisms. The proposed harvester has a symmetric structure with a doubly-clamped configuration enclosing three proof masses in distinct locations. Thanks to the uniform mass distribution, the energy harvesting efficiency can be considerably enhanced. To determine the optimum geometry for the preferred nonlinear behavior, we have also used optimization methodology based on GA. The prototype measurements demonstrate that our proposed piezoelectric MEMS harvester is able to generate voltage at 227 Hz (the first mode), 261.8 Hz (the second mode), and 286 Hz (the third mode). When the device operates at its second mode frequency, nonlinear behavior can be obtained with extremely small magnitude of base excitation (i.e., 0.2 m/s^2). Its normalized power density (NPD) of 595.12 ($\mu W \cdot cm^{-3} \cdot m^{-2} \cdot s^4$) is found to be superior to any previously reported piezoelectric MEMS harvesters in the literature.

In this dissertation, we also propose a piezoelectric MEMS vibration energy harvester with the capability of oscillating at ultralow (i.e., less than 200 Hz) resonant frequency. The mechanical structure of the proposed harvester is comprised of a doubly clamped cantilever with a serpentine pattern associated with several discrete masses. In order to obtain the optimal physical aspects of the harvester and speed up the design process, we have utilized a deep neural network, as an artificial intelligence (AI) method. Firstly, the deep neural network was trained, and then this trained network was integrated with the GA to optimize the harvester geometry to enhance its

performance in terms of both resonant frequency and generated voltage. Our numerical results confirm that the accuracy of the network in prediction is above 90%. As a result, by taking advantage of this efficient AI-based performance estimator, the GA is able to reduce the device resonant frequency from 169Hz to 110.5Hz and increase its efficiency on harvested voltage from 2.5V to 3.4V under 0.25g excitation.

To improve both durability and energy conversion efficiency of the piezoelectric MEMS harvesters, we further propose a curve-shaped anchoring scheme in this thesis. A doubly clamped curve beam with a mass at its center is considered as an anchor, while a straight beam with proof mass is integrated to the center of this anchor. To assess the fatigue damage, which is actually critical to the micro-sized silicon-based piezoelectric harvesters, we have utilized the Coffin-Manson method and FEM to study the fatigue lifetime of the proposed geometry comprehensively. Our proposed piezoelectric harvester has been fabricated and its capability in harnessing the vibration energy has been examined numerically and experimentally. It is found that the harvested energy can be enlarged by a factor of 2.66, while this improvement is gained by the resonant frequency reduction and failure force magnitude enlargement, in comparison with the conventional geometry of the piezoelectric MEMS harvesters.

Acknowledgments

I would like to express my sincere gratitude to my supervisor Dr. Lihong Zhang for his continuous support in my PhD study, research, motivation, enthusiasm, immense knowledge and his assistance in writing papers and thesis. I also intend to thank the other members of my supervisor committee, Dr. Masek and Dr. Pope, for their guidance and suggestions.

This work was supported in part by the Natural Sciences and Engineering Research Council of Canada, in part by Canada Foundation for Innovation, in part by the Research and Development Corporation of Newfoundland and Labrador through its Industrial Research and Innovation Fund and ArcticTECH R&D Award, Memorial University of Newfoundland, and CMC Microsystems.

To my lovely parents

Table of Contents

Table of Contents

List of Tables

List of Figures

Chapter 1 Introduction

Energy harvesting has become an interesting field of research in recent few years with a target of meeting energy requirements for low-power electronic applications, such as implantable biosensors [1][2], consumer electronics [3], military equipment [4], and wireless sensor networks (WSN) [5][6]. Normally only batteries are used to power the aforementioned devices that feature low power consumption. However, size limitation and recharging necessity prevent a capability of autonomy. Due to these concerns, more efforts are striving to replace the batteries with more efficient power solutions that have no lifetime worries. The energy harvesting from ambient resources is the key of this technology.

Portability, as an important factor in many practical applications, is strongly demanded. The level of portability is identified by device dimension and lightness. High portability promises easy deployment and reduced interfacing cost. The micromachining technology is known as one major method for producing portable devices. By using lithography and etching techniques to expose the designed patterns on silicon surface, this technology can manufacture micrometer-sized or even smaller mechanical parts. Several processing methods for micromachining fabrication, such as bulk micromachining [7], surface micromachining [8], and LIGA [9], have been proposed. Micromachining has been interpenetrating several disciplines (e.g. medicine, optics, mechanical and electrical engineering). Likewise, integrated circuits (IC) can be fabricated with similar procedures. Advanced design automation methods can enhance the fabrication quality and circuit performance by considering the electronic device parasitic effects [10] and manufacturability issues [11]. Due to similarity in the fabrication, micromachining and microelectronics can be

integrated to offer micro-electro-mechanical-system (MEMS), a practical micro-system with high portability and reliability [12].

The available natural harvestable energy in outdoor environment includes solar, thermal and vibrations. Solar power system is one of the most usual methods of energy harvesting [13]. Since high solar energy conversion efficiency is highly dependent on surface area of solar cells in addition to availability of sunlight, MEMS or other portable devices, which may not gain the best profit from solar energy due to their inherent tiny physical size, require other ambient energy sources. Electricity generation associated with thermal is another approach for MEMS or other portable energy harvesters. The temperature difference between two various materials can offer electrical power, for example thermocouples [14]. However, large temperature gradient is not feasible for the MEMS or other portable devices with miniature sizes [15].

Table 1 presents ambient harvestable energy sources including solar, wind, thermal, and fluid (i.e., water drop) [16][17]. As an important factor for expressing power conversion capability, power density is also listed in Table 1 for evaluation purpose. The comparison among power densities of ambient energy sources shows that solar cells have the highest power conversion potential when sunshine is abundant. Nevertheless, it may deliver unsatisfactory performance in some applications due to lack of sufficient sunlight [18]. Furthermore, because of low power conversion efficiency in thermal and fluid flow sources as well as difficulty in fabrication, they are not highly qualified for popular energy harvesting. Under such a condition, wind flow (i.e., vibration) may be considered as one promising candidate. A successful example of wind energy harvesting is wind farms. The large-scale wind turbines, which have been known for centuries, can generate kilowatts or even higher electrical power for on-grid systems or even form wind power plants [19].

Table 1. The harvestable ambient energy sources.

Ambient Source	**Power Density**
Solar in outdoor	100 mW/cm^2
Wind at 4.47 meter/second (m/s) speed	10.4 mW/cm^3
Thermal at $\Delta T = 5\ ^{\circ}C$	60 uW/cm^2
Water drop with size of 0.35 mL at 3.43 m/s speed	30.67 uW/cm^2

The vibrations may be harvested from wind flow [20], water stream [21], blood pressure [22], or road traffic [23]. To convert vibrations to electricity, electromagnetic-, electrostatic-, and piezoelectric-based techniques have been proposed as feasible solutions to MEMS or portable vibration energy harvesters. Since the functionality of the electromagnetic generators is based on magnetic field strength, a big permanent magnet, which may unfortunately degrade device portability degree [24], is normally required to achieve high energy conversion efficiency. The electrostatic-based technique can offer a highly compact energy harvester. However, for polarization of capacitor's plates, utilizing a high external bias voltage [25] or electret material [26] seems to be necessary, which virtually prevents them from forming standalone energy harvesters. In contrast, the piezoelectric-based technique, thanks to the piezoelectric material deposition compatibility with micromachining process and the independence from external voltage supply, has attracted more attention in building up MEMS-based vibration energy harvesters [27][28].

The regular MEMS process flows, such as sputtering, material deposition, etching, etc., can readily build a tiny integrated vibration energy harvester with ultra-light weight based on piezoelectric-base technique. Thus, the portability can be significantly improved. Fig. 1 illustrates a complete MEMS process flow for manufacturing a piezoelectric-based micro-scale wind (i.e.,

vibration) energy harvester [29]. Firstly, silicon oxide is grown on silicon wafer (Fig. 1A). At the next step, Pt/Ti is deposited as a bottom electrode by DC magnetron. The PZT material, which is commercially available as sol-gel, is deposited. Then on its top, Pt/Ti is deposited again for top electrode as shown in Fig. 1B. Afterwards certain required shape can be patterned by etching process to form a whole chip as depicted in Figure 1C. In Fig. 1D, the final chip structure of the energy harvester after several backside and frontside silicon etching steps is depicted.

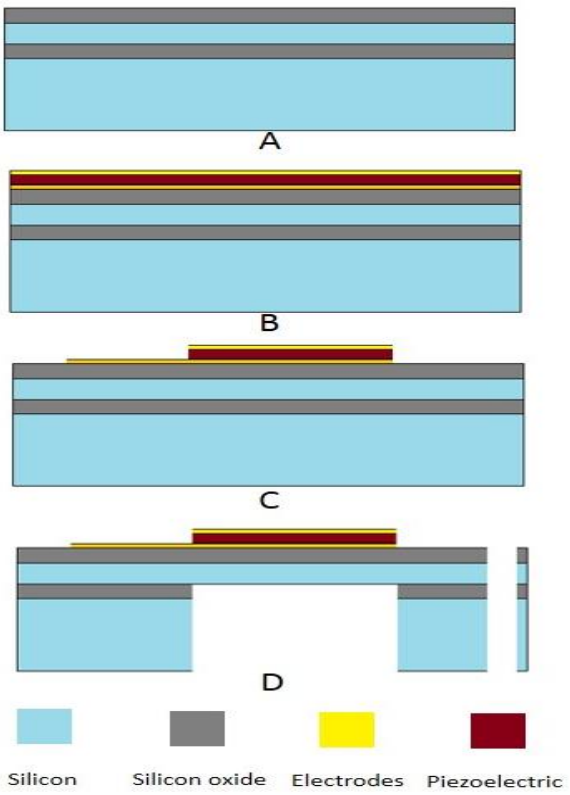

Fig. 1. MEMS process fabrication flow. (A) Silicon on insulator (SOI) wafer with buried oxide layers. (B) Bottom and top electrodes deposited and piezoelectric material sandwiched between them. (C) Required pattern on electrodes. (D) Backside and frontside silicon etching has been performed with piezoelectric cantilever structure and proof mass released.

The rest of the thesis is organized as follows. Chapter 2 reviews vibration-based energy harvesting techniques by the portable and MEMS harvesters for low-power applications. Chapter 3 describes a design and optimization method for efficiency improvement of the unimorph piezoelectric energy harvesters. In Chapter 4, a multi-objective optimization methodology, which can enhance the harvested voltage and reduce the operational resonant frequency of the MEMS harvesters, is proposed. In Chapter 5, a T-shaped piezoelectric structure with the capability of harnessing a considerable amount of stress/strain from the tip part of the structure besides the anchor region is proposed. In order to broaden the operational frequency of MEMS harvesters, in Chapter 6 we present a nonlinear multi-mode structure. In Chapter 7 a design automation technique based on artificial intelligence is discussed. And a new structure for improving fatigue lifetime and the corresponding analysis method is presented. Conclusions are drawn in Chapter 8, which is followed by a discussion about future work in Chapter 9.

Chapter 2 Portable Energy Harvesters for Low-Power Applications

In this chapter, the recent developments of portable vibration energy harvesters for low-power electronic applications, which include energy harvesting techniques, energy harvesting mechanical mechanisms and their physical dimensions, will be discussed in Sections 2.1-2.3, respectively. Then in Section 2.4 the power management systems, which make the portable energy harvesting devices usable in real applications, will be discussed. The major work in this chapter has been formally documented in one journal paper (as listed in the Appendix [Journal-1]).

2.1. Agile Vibration Energy Harvesting Techniques

The generation of milliwatt electrical power from vibration (e.g., wind flow energy) is relatively new compared to the conventional high power generating techniques. The wind harvesting devices normally consist of fixed components and active parts, which are vibrated by mechanical power of wind flow. Scalable in size, these energy harvesters can offer milliwatt output power. The quantity of generated power depends on system size and wind flow velocity in the ambient environment. Theoretically the mechanical power available from a cross sectional area between wind flow and energy harvesting devices can be expressed by [30]:

$$P = \frac{1}{2} A \rho V^3 , \qquad (1)$$

where A is the cross sectional area in m^2, ρ is the density of flow that might be air or water density in kg/m^3, and V is the velocity of the flow in m/s. Albert Betz concluded that a wind turbine theoretically cannot convert more than 59% of the kinetic energy of wind to mechanical energy,

which is known as Betz limitation [31]. Considering this limitation, power coefficient (C_p) and efficiency (η_g) of a generator can be inserted into (1), which can be rewritten as follows,

$$P = \frac{1}{2} A \rho V^3 C_p \eta_g . \quad (2)$$

To realize the energy conversion modelled in (2), the following three main steps during electric power generation should be completed by an energy harvester:

(1) Collect the mechanical stresses from ambient sources, which are applied to the mechanical active part of the harvester;

(2) The kinetic energy offered by wind as vibration sources is converted to electrical energy;

(3) Process the generated power to make it as DC voltage and store it in a super-capacitor cell.

A variety of performance metrics have been utilized for evaluating the capability of energy harvesting in terms of energy conversion from mechanical to electrical power. Some of these Figure of Merits (FOMs), such as charge constant (d) and voltage constant (g), are only related to piezoelectric materials, while the geometry size of energy harvesters is not taken into account [32]. To include more factors, Aktakka *et al.* [33] proposed normalized power density times bandwidth as a FOM. Although this metric indeed is a comprehensive FOM, most of the published papers in the literature provide insufficient information about bandwidth that their proposed devices can achieve. A straightforward multiplication between normalized power density and bandwidth may fail to provide a comparison for the largest pool of the existing harvesters. Therefore, in this chapter we use the normalized power density, which is defined below, as one FOM:

$$P_{density} = \frac{P_m}{Volume \times V} , \quad (3)$$

where P_m is the measured electrical peak power, *Volume* is the volume of the harvester, and V is the wind speed. Moreover, the power coefficient C_p, which is more relevant in the context of non-linear wind velocity with reference to the amount of harvested power, is considered as another FOM in this chapter. It can be defined as [34]:

$$\mathrm{C_p} = \frac{\mathrm{P}_m}{0.5 \times \rho_{\mathrm{air}} \times \mathrm{A} \times \mathrm{V}^3}. \quad (4)$$

To convert ambient vibration (including wind energy) to electricity, piezoelectric- [18], electromagnetic- [35], and electrostatic-based [36] techniques have been introduced in the previous research. Among them, each technique has its distinct advantages as well as disadvantages. The electrostatic-based technique can build up a tiny energy harvester if using micromachining process. Therefore, this technique is quite useful for MEMS-based energy harvesters. Certain analytic modeling methods [37] can be used to formulate the coupling and substrate capacitance in the micrometer or nanometer technologies. However, to function well, such energy harvesters need to manage a large initial voltage (as bias voltage) or electret [25] for supplying electrical charges between capacitor plates. In contrast, the piezoelectric- and electromagnetic-based techniques, which are more often used for portable wind energy harvesting, need no external power sources.

Theoretically the power produced by the piezoelectric-based technique can be expressed by:

$$\frac{1}{2} \times \sigma^2 \times \frac{\mathrm{K}^2}{2\mathrm{c}}, \quad (5)$$

where σ is the applied stress, K is the coupling coefficient, and c is the elastic constant. As shown in the analytic equation above, amount of the harvested power is dependent on several parameters, such as the applied stress on piezoelectric materials provided from ambient vibrations, the coupling coefficient and the elastic constant. Both the coupling coefficient and elastic constant are related

to piezoelectric material properties. It is obvious that enhancing the applied stress on piezoelectric materials can produce more energy [38].

Similarly, power generation with the electromagnetic-based technique can be theoretically estimated by:

$$\frac{1}{2} \times \frac{B^2}{\mu_0}, \quad (6)$$

where B is the magnetic field and μ_0 is the magnetic permeability constant of free space. Since there is a nonlinear relationship between the generated power and electromagnetic field, enhancing the magnetic field strength is one effective way for increasing the produced power [39]. Arroyo *et al.* [40] investigated both piezoelectric- and electromagnetic-based techniques theoretically and experimentally. According to the provided information in this study, the piezoelectric generators have low coupling coefficient and low loss coefficient, while the electromagnetic generators have high coupling coefficient and high resistive loss coefficient. Furthermore, the study of scaling effect in this work shows that, different from the commonly accepted hypothesis, the power density of the electromagnetic-based generators does not necessarily decrease in proportion to their volumes.

The amount of the produced power by the electrostatic-based generators can be calculated by (7):

$$\frac{1}{2} \times \varepsilon_0 \times E^2, \quad (7)$$

where ε_0 is the electrical permittivity of free space and E is the electric field. Therefore, magnitude of the generated power is strongly determined by the strength of the electric field, which is in turn up to the magnitude of bias voltage or electret [41]. The comparison between electrostatic- and

piezoelectric-based generators, as presented by Elliot *et al.* in [42], shows that the electrostatic-based technique performs better than the piezoelectric-based technique at low acceleration scenarios due to lower energy losses, while the piezoelectric-based technique outperforms the electrostatic-based technique at high acceleration operating conditions. However, the MEMS scale piezoelectric-based energy harvesters at very high accelerations may have lower performance due to the dielectric breakdown limit of piezoelectric materials. Thus, the electrostatic-based technique is preferred for MEMS energy harvesters if a very high acceleration operating condition is expected. In the following sub-sections, each power generation technique will be discussed in more detail.

2.1.1. Piezoelectric-Based Generators

Due to dichotomy behaviour, piezoelectric materials have been utilized in many type of sensors and actuators [43][44]. There are different natural crystal classes capable of piezoelectricity, among which three are more commonly utilized in micromechanical systems. They include zinc oxide (ZnO) as a MEMS transducer [45], aluminium nitride (AlN) for thin film depositing [46], and $Pb(Zr_xTi_{1-x})O_3$ (PZT) as an active material [47]. Among them, PZT is the most popular option for power conversion due to its high electromechanical coupling factor as defined below,

$$K^2 = \frac{\text{Electrical Energy converted}}{\text{Mechanical energy applied}} \cong \frac{\left(\frac{d_{31}}{s_{11}}\right)^2}{\varepsilon_{33}}, \qquad (8)$$

where K is the electromechanical coupling factor, d_{31} is the piezoelectric constant, ε_{33} is the dielectric constant, and s_{11} is the mechanical compliance coefficient. For a better comparison, the relative electromechanical coupling factors for three major types of piezoelectric materials are

listed in Table 2 [48]. We can see that PZT has more than double electromechanical coupling factor over AIN or ZnO. Therefore, this type of piezoelectric materials has been widely used for power generation in portable energy harvesting devices [49]:

Table 2. Relative electromechanical coupling factors for three different piezoelectric materials.

ZnO	AlN	PZT
0.34	0.47	1

The equivalent circuit of piezoelectric generators, which expresses both mechanical and electrical parts, is depicted in Fig. 2 [50]. At input of this circuitry, external excitation force F is applied. The mechanical branch has one resonant impedance element (Z), which is dependent on stiffness of mechanical resonator and mechanical branch mass. The transformation ratio is equal to $N=C_{pz}h_{33}$, where C_{pz} is the clamped capacitance of piezoelectric material mainly measured when piezoelectric layer is not deformed and h_{33} is the ratio between piezoelectric coefficient and mechanical compliance. On the right side, the transformer and clamped capacitance illustrate power conversion in energy harvesters with U (voltage) presented as output [51].

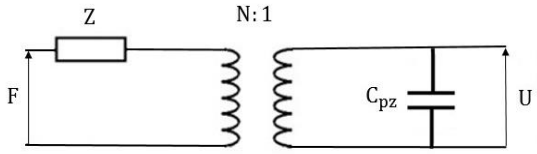

Fig. 2. Equivalent circuit of the piezoelectric-based generators.

For the first time, Carroll introduced a small energy harvester for collecting energy from water flow based on piezoelectric material [30]. In comparison with the conventional energy harvesters such as wind turbines [52], its size, which was significantly reduced, can offer great portability to a variety of applications. Equation (2) theoretically and the experimental data from [30] empirically show that the amount of the generated electrical power is highly dependent on

harvester dimension and flow speed. In parallel with size reduction for a goal of increasing portability, drop of the output power amplitude is prevalent. To overcome this issue, some research has been conducted to apply different structures or materials to magnify the conversion results [53][54].

2.1.2. Electromagnetic-Based Generators

The amount of induced voltage in the electromagnetic coil can be computed by [55]:

$$\mathrm{U} = -\mathrm{N}\frac{\mathrm{d}\phi}{\mathrm{dt}}, \tag{9}$$

where *U* is the generated voltage, *N* is the number of turns, and ϕ is the total flux linkage. The flux density is highly dependent on magnetic field, which is given by

$$\phi = \mathrm{B\,A}\sin\theta\,, \tag{10}$$

where *B* is the magnetic field, *A* denotes the perpendicular area to the magnetic field, and θ is the angle at which the magnetic field contacts the coil.

The equivalent circuit for explaining the working principle of the electromagnetic-based generators is displayed in Fig. 3 [56]. Similar to the piezoelectric equivalent circuit, a mechanical force *F* as input is applied to a mechanical resonator with resonant impedance *(Z)*. A transformer can convert mechanical power to electrical power with ratio *N* following $N = BL/Z_e$, where *L* is the length of the wire that constitutes the coil and Z_e is the coil impedance. The coil impedance is relevant to the inductance and resistance of the coil [51]. The conversion result from mechanical energy to electricity is depicted by *U* (voltage) in Fig. 3.

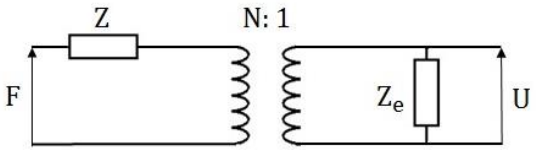

Fig. 3. Equivalent circuit of the electromagnetic-based generators.

The interaction between wind flow and moveable part of an electromagnetic energy harvester can provide relative motion, which is bound to produce electrical power. Based on the flux density change in proportion to the conductor location change, several wind flow energy harvesters have been devised. Weimer *et al*. [57] proposed a circular electromagnetic wind energy harvester for the axial-flux alternator, where the rotor included 8 neodymium magnets in an alternating pole configuration (as shown in Fig. 4) and the stator was manufactured with two separate copper wire coils having 1250 turns. The diameter of the stator and rotor plates is 76.2 mm. The wind flow can rotate the rotor plate, which induces electrical voltage in copper wires. The maximum harvested electrical power in this study at the highest wind speed (8.94 m/s) is 651 μW.

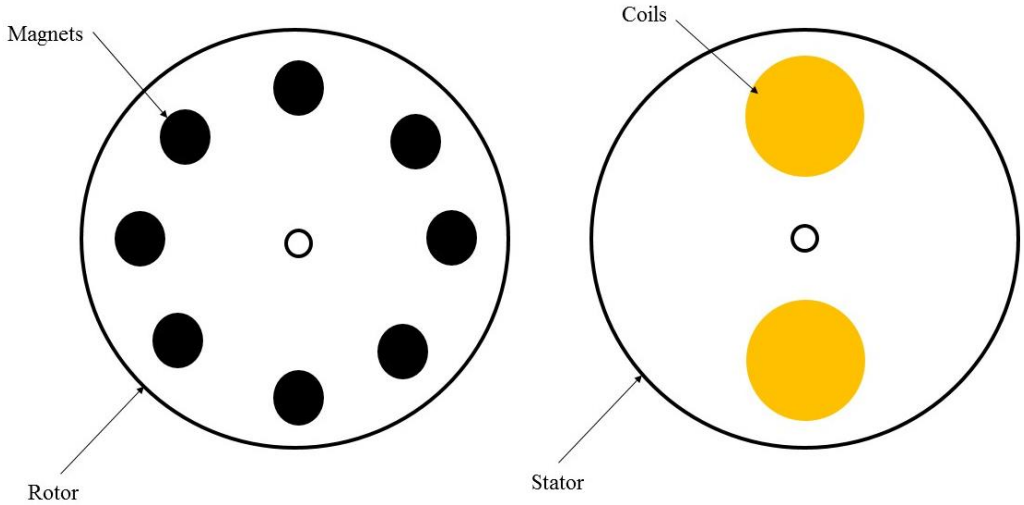

Fig. 4. Rotor and stator for the axial-flux alternator.

A Helmholtz-resonator-based electromagnetic energy scavenger was introduced by Kim *et al*. [58]. The simplified schematic of the proposed Helmholtz resonator-based energy harvesting is depicted in Fig. 5. This Helmholtz resonator has a chamber, which is simply filled with gas (air), with an open neck in the middle. The air inside the chamber has spring behavior and the air inside the neck acts as mass. Thus, this system can be modeled by a second-order differential equation. To increase the efficiency, a diaphragm (membrane) is attached to the bottom wall of the resonator with a magnet fixed on this diaphragm. While fluidic oscillation happens for the diaphragm due to mechanical energy of wind flow, the magnet attached to the diaphragm vertically vibrates inside the coil. This devised energy harvester includes two parts, a cylindrical chamber with 19 mm diameter and 5 mm height, and a neck on top of the chamber with 3 mm diameter and 5 mm height. It could produce peak to peak voltage output of 4 mV at 5 m/s wind velocity. However, the power conversion efficiency of the proposed wind energy harvester was quite low even at high wind speed. Thus, it may not function very well for practical applications.

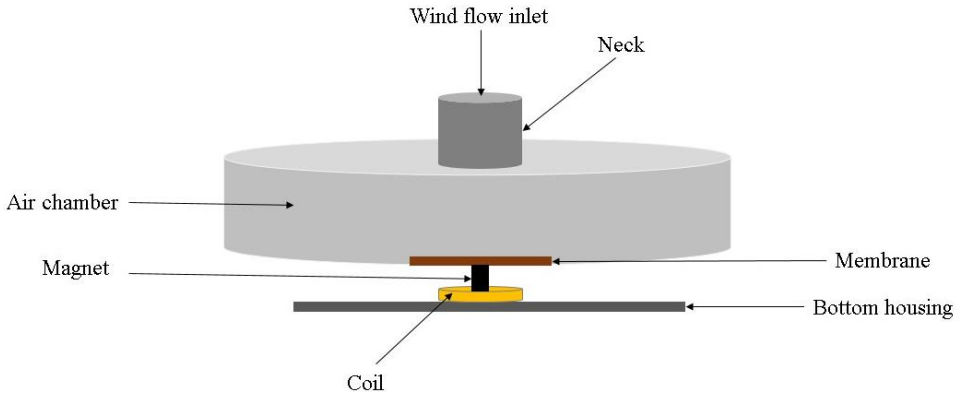

Fig. 5. Schematic diagram of the Helmholtz resonator-based energy scavenger.

Another configuration that can function well is to use coils as moveable component and consider magnets as the fixed part of electromagnetic generators. Feasibility of an energy harvesting system based on wind-induced vibration of bridge cables was investigated by Jung *at*

al. [59]. In this study, an electromagnetic-based generator was introduced to harvest wind-induced vibration energy due to interaction between wind flow and cables. The proposed device, as depicted in Fig. 6, includes a big circular magnet with an opening in the center. The proposed energy harvester has a suspended coil, which is connected to a spring. The ambient vibrations cause oscillation to the coil, which can induce the relative motion inside the magnet. In comparison with the other research work, the proposed device in this study can provide greater magnetic flux due to use of a big magnet compound (enclosing the fixed magnet and moving coil). With 80 mm diameter and 10 mm thickness, the utilized circular magnet could generate magnetic flux density of 0.5 Tesla. The experimental results showed that this device could generate 27.14 mW RMS power at 5.4 m/s wind speed.

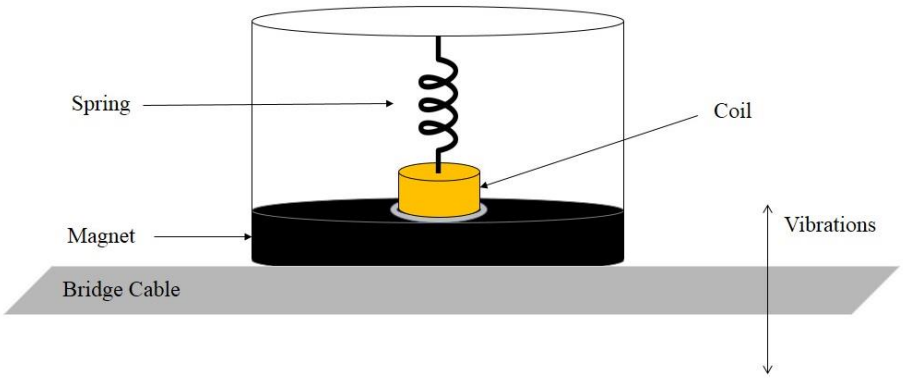

Fig. 6. Schematic diagram of the wind-induced energy harvesting system.

By comparing the existent piezoelectric and electromagnetic techniques above, we can see the presented equivalent circuits for both approaches are almost the same. As illustrated in Fig. 2 and Fig. 3, the output impedance is capacitive for the piezoelectric generators and resistive for the electromagnetic generators. For adapting load impedance, the electromagnetic-based generators need a load impedance of some kilo ohm, whereas the piezoelectric-based generators require a load impedance in mega ohm range. Furthermore, the damping factor for the piezoelectric

generators is constant because the used piezoelectric material has unchangeable surroundings. However, the electromagnetic-based generators have varied damping factor, which may change along with electromagnetic or resistive load variation. Furthermore, a minimum deformation in the electromagnetic-based generators has to be required, which means the wind flow should be strong enough to provide such a minimum deflection.

2.1.3. Electrostatic-Based Generators

Another technique for electrical power generation from ambient environment is electrostatic method, whose operation is based on a capacitive structure created by two standalone electrodes. The gap between both electrodes can be filled with air, vacuum, or any dielectric materials [60]. The variation of capacitance, which takes place by moving one of the electrodes, is able to convert mechanical vibration to electricity by charge-discharge cycles or electret. This type of generators can be categorized into two groups [61]: (1) Electret-free electrostatic generators, whose functionality is dependent on external bias voltage [25]; (2) Electret-based electrostatic generators, which are able to directly turn ambient vibration to electricity thanks to electret utilization on the surface of one or both electrodes. Electrets are the dielectric material with a capability of keeping electric field and surface potential inside the structure for years just like the magnets in the electromagnetic-based generators [62]. Figure 7 illustrates the electret-based generator and its equivalent circuit, where Q_e is the electret charge, Q is the sum charge between counter (movable) electrode and fixed electrode, R is the load resistance, $C(t)$ is the capacitance of the electrostatic energy harvester, and U_e is the surface voltage on electret [63]. The relative motion of the counter electrode leads to variable capacitance, which induces electrical current through load.

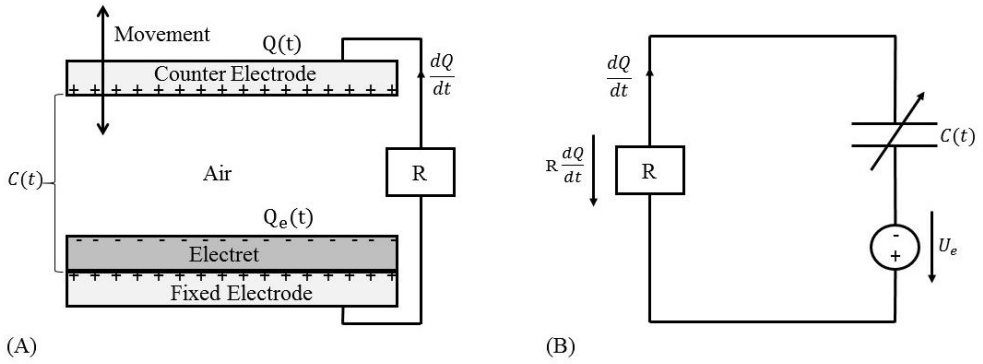

Fig. 7. (A) Schematic view of the electret-based electrostatic energy harvesters and (B) equivalent circuit.

If the prerequisite initial electrical charge for capacitor polarization is realized by the electret materials, promising harvesting performance may be offered by the electret-based electrostatic energy harvesters. Recently Perez *et al.* [63] introduced a wind energy harvester by deploying the electret-based electrostatic technique. The proposed device in this study includes two parallel copper plates with the size of 50 mm and 200 μm in length and thickness, respectively. Both copper films are covered with a 25 μm Teflon PTFE layer, which was fabricated by corona discharge. Furthermore, a membrane with 25 μm thickness of PVDF, whose two sides were deposited with 10 nm gold layer, is attached to a bluff body. The schematic diagram of this wind energy harvester is illustrated in Fig. 8. The proposed system has two capacitors between the membrane and upper electrode (C_{upper}) as well as lower electrode (C_{lower}). When wind flow blows the membrane to move upwards and downwards, capacitance of the energy harvester would be changed continuously. When wind flow velocity reaches 10 m/s, the membrane can oscillate. The average output power during period time T is proportional to the capacitance variation between C_{max} and C_{min}, which can be determined by:

$$P_{elec} = \frac{1}{T}\int_0^T R\left(\frac{dQ}{dt}\right)^2 dt \propto (C_{max} - C_{min})U_{elec}^2 f, \qquad (11)$$

where U_{elec} is the surface electret voltage, f is the oscillation frequency, C_{max} and C_{min} are maximum and minimum possible capacitances, respectively.

The experimental data in this study show the proposed wind energy harvester was able to produce 2.1 mW power and 200 V output voltage, when the electret voltage is -650 V with 30 m/s wind speed. Even though this wind energy harvester has a simple structure, the required high wind speed (10 m/s) for fluttering the membrane makes it somehow impractical for the regular windy conditions. In addition, a special power management system has to be considered due to the generated high output voltage and low current.

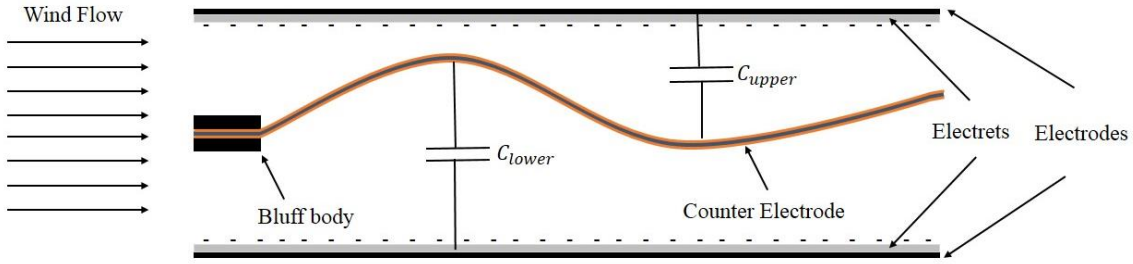

Fig. 8. Schematic representation of the proposed wind energy harvester in [63].

2.2. Mechanical Mechanisms for Portable Vibration Energy Harvesting

The energy harvesting devices need to function as a mechanical resonator for converting wind flow to vibrations. The direct reaction between wind flow and moveable part of energy harvesters is oscillation. This periodic oscillation can affect the active part of the energy harvesters. All the portable wind energy harvesters in the literature follow two distinct mechanical mechanisms for

trapping wind flow vibrations. In this regard, we can classify the wind energy harvesters into two groups: rotational and aeroelastic harvesters. Below each group is discussed in more detail.

2.2.1. Rotational Harvesters

Figure 9 shows the mechanical structure of rotational wind energy harvesters. The rotational movement is a circular motion of an object with reference to its center. This type of motion has been widely used in the traditional large-scale windmills [64]. Due to high reliability and accumulated mature design knowledge, this mechanism has been widely used for small-scale wind energy harvesting devices [34]. Normally, the rotational-mechanism-based devices, such as the one in [65], may include a fan with multiple blades and a jamb, which is fixed in the centre of the fan. The energy of wind flow can rotate the fan around the fixture. The intensity of rotation is related to wind flow speed. In other words, wind blowing in higher speed can induce circular motion with higher frequency of rotation for the moveable part of the harvesters.

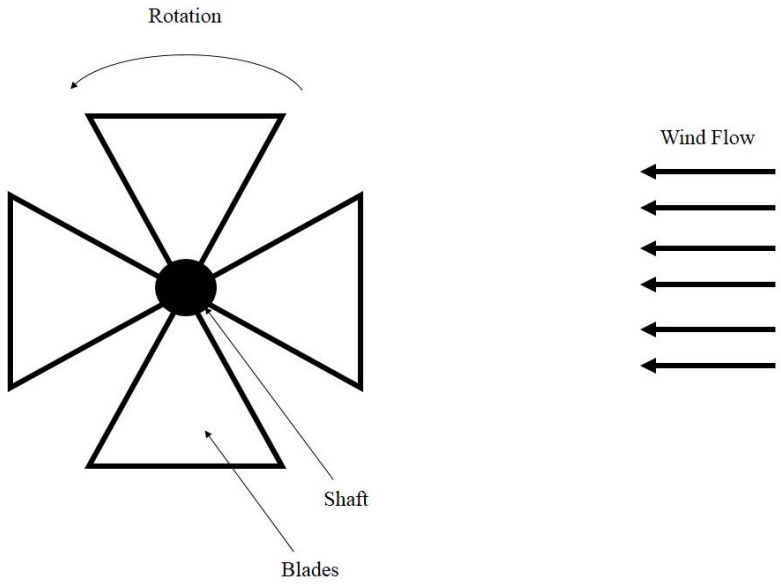

Fig. 9. Diagram of portable wind energy harvesting devices based on rotational mechanism.

The rotational mechanism has been used for piezoelectric-, electromagnetic- and electrostatic-based wind energy harvesters. In the piezoelectric-based harvesters, one side of the piezoelectric cantilever is clamped by the fan and the other side is free. Then the induced rotation in the fan can move the piezoelectric cantilever. The interaction between the shaft, which is a fixed point in the centre of the fan, and the moveable side of the piezoelectric cantilever applies relative stress to the piezoelectric material. Priya *et al.* [66] introduced a small-scale wind energy harvester based on piezoelectric direct effect, which was combined with the traditional windmill features and piezoelectric properties. The proposed device included 12 bimorph piezo-cantilevers, which were attached to a quite small fan. The schematic of such a piezoelectric windmill with 12 cantilevers is illustrated in Fig. 10. Wind flow could apply oscillatory stress on the cantilevers since the fan could be easily rotated at the normal wind flow conditions. The dimension of each individual bimorph was 60 × 20 × 0.6 mm^3. This energy harvesting device was able to generate power of 10.2 mW at the frequency of 6 Hz.

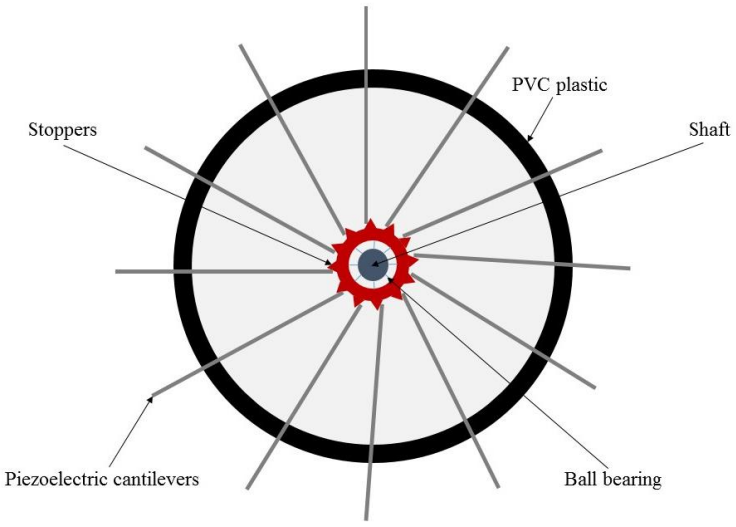

Fig. 10. Schematic diagram of the piezoelectric windmill consisting of 12 piezoelectric cantilevers.

Another rotational piezoelectric wind energy harvester, which was introduced by Yang *et al.* [67], consisted of 12 micro-cantilevers with $47 \times 20 \times 0.5$ mm^3 dimension behind the fan. One or multiple shafts were located at the centre of the fan. Wind flow could rotate the fan, while the interaction between shafts would apply relative stress to piezoelectric cantilevers. The prototyped device in this research could generate 613 μW rectified power. In comparison with the conventional energy harvesters such as wind turbines, the size of the developed devices in these studies was significantly reduced. In spite of the size reduction, how to prevent reducing the harvested power is a challenging question to be addressed.

The frequency of the applied stress is proportional to the rotational frequency of the fan. The advantage of the piezoelectric-based harvesters is the huge stress applied to the cantilevers at the centre of the fan due to high torque at that location, which can be computed by $\tau=Fd$, where F is the excitation force (wind flow) and d is the distance between the force and the free end of the cantilever. Consequently, the maximum torque may appear around the center of the rotational structure, where shaft is located. Furthermore, increasing the number of the piezoelectric cantilevers may increase the number of stoppers, which are actually the confluence nodes between cantilevers and shaft. As a result, the rotational frequency would be dropped. Therefore, higher wind flow speed is required for the proper function of these harvesters.

On the other side, for the electromagnetic-based harvesters, the required movement for the rotor can be achieved by the mechanical rotational mechanism, which is able to provide a relative motion between the rotor and stator in the harvesters [57]. The rotational structure normally encloses a big plane, which can provide sufficient space for locating magnets or accessing coils on the top. This available space can also allow the designers to enlarge the generated power by adding more magnets. But it should be noted that, by applying more magnets for enhancing magnetic field,

the mechanical rotational structure may gain a lot of weight, which in turn requires stronger wind flow to make rotation feasible. Similarly, the rotational mechanism is able to be used by the wind energy harvesters based on electrostatic generators. In a recent study conducted by Perez *et al.* [26], a small wind turbine with 4 blades within 4 cm rotor diameter to extract power from wind flow was devised. The proposed device could generate 1.8 mW output power at 10 m/s wind speed. The main advantage of this energy harvester is its capability of generating 95 μW power at wind speed as low as 1.5 m/s.

The main advantage of the rotational mechanism is to provide an alternative and strong spin with sufficient space for patterning the active part of an energy harvester. But this mechanism needs relatively larger space for making rotation viable. Therefore, the portability associated with this mechanism is not high. For this reason, no MEMS wind energy harvester entirely based on rotational mechanism has been developed thus far.

2.2.2. Aeroelastic Harvesters

When a mechanical resonator is immersed in a fluid flow, aerodynamic phenomena (such as vortex shedding, fluttering, and galloping) may appear around or on the structure. As a result, vibration can be observed as shown in Fig. 11, which presents the most common aerodynamic mechanisms, (A) vortex shedding with a bluff body, (B) flutter with attachment of an airfoil, (C) galloping with attachment of a prismatic object, and (D) flapping leaf [68][69].

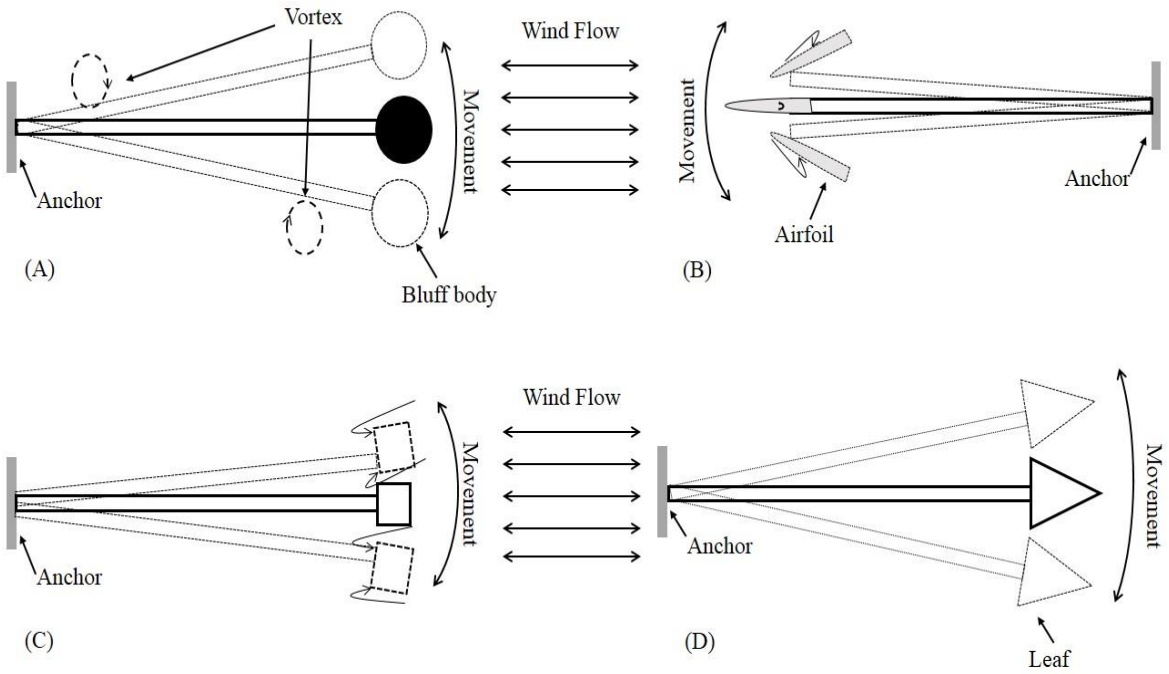

Fig. 11. Common aeroelastic mechanisms for wind energy harvesting: (A) vortex shedding, (B) flutter, (C) galloping and (D) flapping leaf.

The existing aeroelastic mechanisms in the literature for wind energy harvesting can be categorized into two groups: (1) vortex induced vibrations (VIV) and (2) movement induced vibrations [34][70]. Normally in VIV, a cylindrical bluff body is located at the end of cantilever in a wind energy harvester. When wind passes the bluff body, the resulting flow would form discrete vortices due to gradient pressure. The pattern of the vortices shedding alternately from one side of the body and then the other side is called Karman vortex street. In the situations where vortex shedding behaviour is periodic, the frequency can be determined by [34]:

$$f = \frac{S\,V}{D}, \qquad (12)$$

where V is the wind flow speed, D is the characteristic dimension (e.g., the diameter if a circular cylinder is used as a bluff body or the channel diameter if a fluid channel is used), and S is the

Strouhal number that is a dimensionless number for describing oscillating flow mechanism. The Strouhal number depends on both the body shape and the Reynolds number, which can be calculated with (13),

$$\mathrm{Re} = \frac{\mathrm{D\,V}\,\rho}{\mu}, \tag{13}$$

where ρ is the flow density and μ is the flow viscosity. When the vortex shedding frequency is close to one of the harmonic natural frequencies of the aeroelastic harvester, lock-in or synchronization takes place so that the energy harvesting maximum power is feasible under this condition [71].

Zhu *et al.* [72] presented an electromagnetic wind energy harvester based on VIV. The proposed device includes a 50 mm × 18 mm × 0.2 mm cantilever made of Beryllium Copper (BeCu). As shown in Fig. 12, a cylindrical magnet, which is made of NdFeB-38H with 15 mm diameter and 10 mm height, is fixed at the end of the cantilever with certain distance (15 mm) from an 80 mm × 25 mm × 6 mm rectangular aerofoil, which is located at the other side of the cantilever. The overall size of the device is 12 cm × 8 cm × 6.5 cm. According to reported experimental data, the proposed electromagnetic generator could operate with harvested electrical output power of 470 μW at the wind speed as low as 2.5 m/s. When the wind speed reached 5 m/s, the amount of output power was 1.6 mW. Although the harvested electrical power by the proposed device in this study is enough for most of low power electronic devices, using bluff body may somehow reduce level of portability. In addition, high cut-in wind speed (2.5 m/s) is another drawback of the proposed energy harvester.

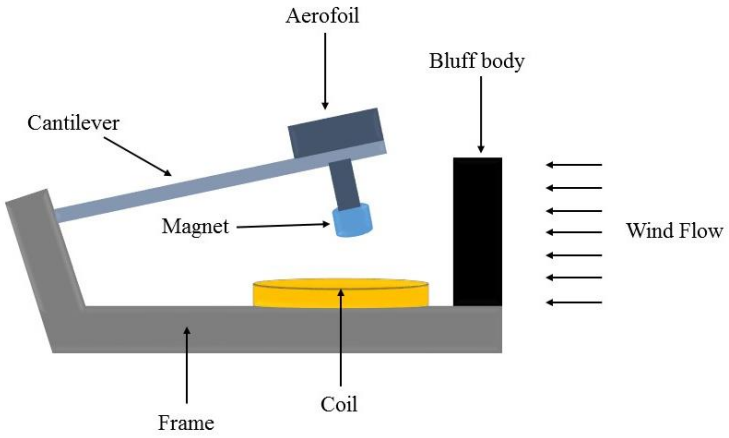

Fig. 12. Schematic diagram of the electromagnetic wind energy harvester based on VIV mechanism.

The VIV mechanism is also capable of being utilized in the energy harvesters based on piezoelectric generation technique [73]. Piezoelectric material is deposited in an area close to the root of the cantilever. A lumped-parameter model for describing the coupling behaviour of the piezoelectric VIV-based wind energy harvesters can be written as [74]:

$$\mathrm{M_{eff}}\ddot{\mathrm{w}} + \mathrm{C}\dot{\mathrm{w}} + \mathrm{Kw} + \Theta\mathrm{U} = \mathrm{F_L}, \tag{14}$$

$$\mathrm{C_{pz}}\dot{\mathrm{U}} + \frac{\mathrm{U}}{\mathrm{R}} - \Theta\dot{\mathrm{w}} = 0, \tag{15}$$

where w is the displacement of the cantilever tip, M_{eff} is the effective mass, C and K are the damping coefficient and stiffness respectively, Θ is the electromechanical coupling coefficient, U is the generated voltage, C_{pz} is the piezoelectric material capacitance, R is the load resistance, and F_L is the vortex induced force.

As the second group of aeroelastic mechanism for wind flow trapping, movement-induced-vibration has a wider scope than the first VIV group, including (i) flutter-based, (ii) galloping-based, and (iii) flapping-leaf-based harvesters, as detailed below. This type of aeroelastic

mechanisms is affected directly by wind flow force. As a result, movement appears right on the fluttering structure.

(i) Flutter-based mechanism: In the aeroelastic flutter-based wind energy harvesters, an airfoil is generally attached to the free end of the beam as shown in Fig. 11B. When wind flow velocity reaches a sufficient level known as the critical flutter speed, negative damping occurs and results in divergence of flutter deformation [70]. The relationship between critical flutter speed and flutter frequency for two degrees of freedom is approximately expressed by [75]:

$$V_c \sim \left(\frac{Y\,T^3}{\rho\,L^3}\right)^{\frac{1}{2}}, \tag{16}$$

$$\omega \sim \left(\frac{\rho\,V^2}{\rho_b\,T\,L}\right)^{\frac{1}{2}}, \tag{17}$$

where V_c is the critical flutter speed, ω is the flutter frequency, ρ and ρ_b are the fluid and beam densities respectively, V is the wind speed, T is the beam thickness, L is the beam length and Y denotes Young's modulus of the beam. Bibo *et al.* [76] presented a piezoelectric wind energy harvester integrated with an airfoil, the equations governing the motion of this lumped-parameter system can be written as:

$$m_T\ddot{h} + m_w X_G \ddot{\alpha} + C_h \dot{h} + K_h h - \theta U = L, \tag{18}$$

$$I_\alpha \ddot{\alpha} + m_w X_G \ddot{h} + C_\alpha \dot{\alpha} + K_\alpha \alpha = M, \tag{19}$$

$$C_{pz}\dot{U} + \frac{U}{R} + \theta \dot{h} = 0, \tag{20}$$

where m_T is the total mass of the airfoil plus the supporting structure, m_w is the airfoil mass alone, X_G is the dimensionless distance between the elastic axis and the center of mass, C_h and C_α are the plunge and pitch structural damping coefficients respectively, and I_α is the mass moment of inertia. The linear structural stiffness factors for the plunge and pitch are K_h and K_α respectively. The electromechanical coupling factor is denoted by θ, while *U* is the generated voltage and *R* is the load resistance. The nonlinear load can be presented by aerodynamic lift *L* and moment *M*, which are equal to [77]:

$$\mathrm{L} = \rho\,\mathrm{V}^2\mathrm{bSC_L}\left(\alpha_{\mathrm{eff}} - \mathrm{c_3}\alpha_{\mathrm{eff}}^3\right), \qquad \mathrm{M} = \left(\frac{\mathrm{b}}{2} + \mathrm{a}\right)\mathrm{L}, \qquad (21)$$

where *V* is the wind flow velocity, *b* is the half chord length, *S* is the airfoil span, C_L is the aerodynamic lift coefficient, and c_3 is a nonlinear parameter derived from wind tunnel tests, α_{eff} is the effective angel of attack and *a* is the elastic axis distance from the mid-chord.

(ii) Galloping-based mechanism: as shown in Fig. 11C, when a prismatic object (such as square, D-section, triangle, etc.) is attached to the free end of a flutter, the oscillation proportional to the incoming wind flow can be formed in a plane [78]. The required condition for the galloping oscillations is the derivative of the steady state aerodynamic lift coefficient is negative. Its main difference from the flutter-based mechanism is that it is a one degree-of-freedom system whereas a flutter-based harvester may be a two- or three-degrees-of-freedom system. Sirohi *et al.* [79] developed a wind energy harvester with galloping piezoelectric beam. The proposed device in that study includes an aluminum beam with 90 mm long, 38 mm width and 0.635 mm thickness. Moreover, two piezoelectric sheets with 72.4 mm, 36.2 mm and 0.267 mm in length, width and thickness respectively are bonded to the top and bottom surface of the aluminum beam. Eventually, a rigid wooden bar with 235 mm long and D-shaped cross section with 30 mm diameter is attached

to the free end of the beam. This energy harvester was able to generate 1.14 mW power at 4.69 m/s wind speed.

(iii) Flapping-leaf-based mechanism: For this mechanism, a flexible leaf or flag is attached to the free end of the beam as shown in Fig. 11D. When wind flow is blowing, the leaf can be moved upwards and downwards to produce vibration. Li *et al.* [80][81] proposed a flapping-leaf-based wind energy harvesting device that has the potential to extract energy from low wind velocity and irregular flow. This study deployed a piezoelectric stalk (made of polyvinylidene fluoride (PVDF)) as an active part of the wind energy harvester. To increase vibration amplitude, a flexible leaf with 8*8 cm^2 was attached to the end of this stalk. With a dimension of 72 × 16 × 0.41 mm^3, the proposed device could generate peak power of approximately 615 μW at 8 m/s wind speed. The required big leaf at the end of the cantilever (stalk) and the generated power amount show that power density of the proposed wind energy harvester is not that high. Moreover, the required large area for flapping operation is one of its major drawbacks.

Numerous methods for predicting and modeling the effect of VIV on the structure are available in the literature. Among them, the phenomenological models based on wake oscillators have high accuracy for representations due to the considered nonlinear factors (e.g., softening and hardening) [82]. Most recently, Dai *et al.* studied more accurate modeling for the fluctuation lift force and investigated the passive suppression mechanism of the cylinder VIV by means of a nonlinear energy sink [83]. To model the galloping-based harvesters, the quasi-steady approximation method may be used [84]. To improve the applicability of this method, further advancement is still required by devising unsteady representations to specify the galloping force. Thus, the effects of the unsteady wake can be taken into account. Moreover, this study on modeling method should be validated and supported by sufficient experimental measurements.

In the literature, almost all the presented mathematical models for aeroelastic flutter-based wind energy harvesters are based on lumped models, where the flutter is considered as a mass-spring-damper system. The main advantage of this modeling is simplicity for extraction of motion equations, which can be utilized for harvesting performance estimation and structural parameter optimization. However, this model is limited due to lack of parameters to consider piezoelectric characteristics and substrate layers. In addition, the lumped-models cannot present the status of dynamic mode shapes and strain distribution. Therefore, there is still a lot of room for improving such models in the future research to account for nonlinear effects of the piezoelectric materials as well as beam's inertia and geometric nonlinearities.

Compared with the rotational mechanism, the aeroelastic mechanism is able to build up very small wind energy harvesting devices. Since it just needs a narrow ribbon for flapping in proportion with air flow power, the required space for this strip is small. Furthermore, the fabrication of this mechanical mechanism is less complex than the rotational one. However, the major drawback of the aeroelastic mechanism is that its efficient operation only occurs in just one direction although wind flow may have arbitrary directions. Zhao *et al.* [85] proposed a portable wind energy harvester by using aeroelastic mechanism, which had an arc shape fabricated by a copper plate. The schematic diagram of the proposed energy harvester is illustrated in Fig. 13. This study clearly showed that a maximum power could be harvested while wind flow incident was perpendicular to the resonator. To overcome this problem, some techniques such as using funnels have been suggested.

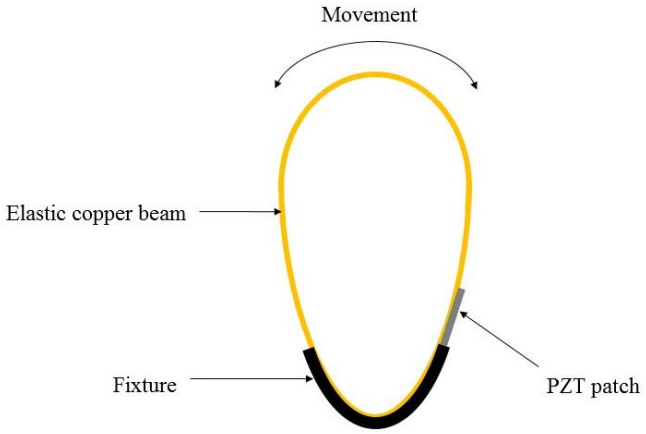

Fig. 13. Schematic diagram of the arc shape wind energy harvester.

Park *et al.* [86] proposed a portable wind energy electromagnetic harvester using the aeroelastic mechanism, which consisted of a T-shape cantilever and a magnet attached at the end of the cantilever. As illustrated in Fig. 14, two coils were fixed at a location very close to the end of the cantilever. Both the cantilever and coils were located inside a funnel, which had two openings as inlet and outlet for wind flow. The inlet of 4×4 inch^2 and outlet of 2×2 inch^2 with 8 inch distance from each other were patterned. The reported experimental results showed that the funnel could magnify wind speed by approximately 20% while the incident angle was at least 30 degrees. However, utilizing funnel may make the device size larger, which in turn reduces the portability.

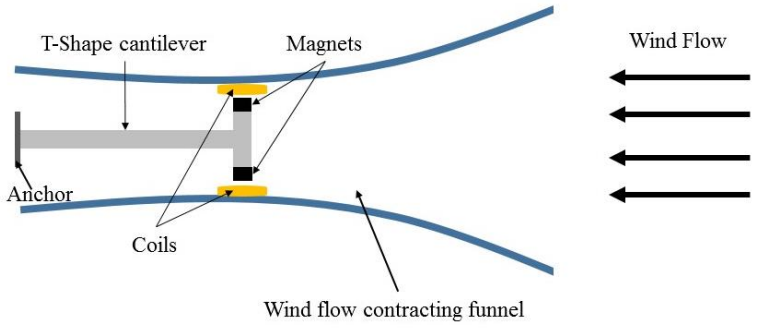

Fig. 14. The electromagnetic wind energy harvester with wind flow contracting funnel.

2.3. Dimension of Portable Vibration Energy Harvesters

The portable wind energy harvesters may have varied sizes from several micrometers to many centimeters. The reported harvesters from the literature can be classified into two major groups, macro and micro sizes, in terms of physical dimensions. In this chapter, we are using the following definition for us to differentiate macro- and micro-scale wind energy harvesters. We consider those devices with any aspect (e.g., length or diameter) greater than 75 mm as the macro-scale wind energy harvesters, while the other ones are categorized as the micro-scale harvesters. In the following sub-sections, we will present each group with a focus on their properties. Moreover, the fabrication methods for the macro- and micro-scale wind energy harvesters will be briefly discussed as well.

2.3.1. Macro-Scale Harvesters

Industry and academia have introduced macro-scale wind energy harvesting devices with dimensions greater than several centimeters. The mechanical aeroelastic mechanism can be

fabricated in macro-scale size for portable energy harvesters. Fei *et al.* proposed a wind-flutter harvester for powering wireless sensors, which encloses a one-meter belt to gain 7 mW electrical energy from 3 m/s wind speed [87]. Matova *et al.* presented a wind energy harvester by using micromachining piezoelectric on diaphragm of Helmholtz resonator [88]. The proposed device has a neck with length of 2 cm and diameter of 2 cm along with a cavity with length of 17 cm and diameter of 8 cm. The resonator worked in an airflow region from 10 to 15 m/s wind speed. The obtained power was 2 μW at 13m/s. After Helmholtz structural optimization, the harvested energy was improved to 42.2 μW at 20 m/s. This device may be considered as a portable wind energy harvester, but its level of portability is fairly low. Moreover, its amount of the generated power is also quite small.

Compared to the micro-scale devices, the macro-scale wind energy harvesters have simpler structures. As shown in (2), there is a strong direct relation between the generated power amount and size of wind energy harvesting devices. Therefore, the macro-scale wind energy harvesters can normally offer much larger output power. The rotational mechanism for both piezoelectric- and electromagnetic-based harvesters can be implemented with a small fan. These rotational harvesters [57] normally fall into the macro-scale category due to the large size of their used fans. The rotation of the fans can directly present motion to the rotor part of the electromagnetic-based harvesters [65], while piezoelectric materials can be located on the fans in the piezoelectric-based harvesters so that rotational movement can stress the piezoelectric materials to produce output electrical power [66].

The mechanical aeroelastic mechanism can be also fabricated in the macro scale domain for portable wind energy harvesters. The electromagnetic-based harvesters by using cantilever can provide relative motion between active part and stator, where coils or permanent magnets are

attached to the end of the free end of the cantilevers for maximum deflection amplitude [89]. In contrast, the piezoelectric technique can also offer an integrated macro-scale wind energy harvester by bonding a ceramic piezoelectric material and a metal ribbon serving as the cantilever. Sirohi *et al.* [90] proposed an energy harvester with two identical aluminum cantilevers with a dimension of 161 mm × 38 mm × 0.635 mm. The piezoelectric films can be bonded near the root of the cantilevers by using epoxy, hot air plastic welding, or pressure.

Table 3 summarizes the previously published macro-scale portable wind energy harvesters by listing their geometry sizes, harvested electrical voltages, harvested electrical powers, normalized power densities, power coefficients, wind speeds, utilized power generation techniques, and deployed mechanical mechanisms for wind flow trapping. By default the harvester geometry size is given in the form of *length* × *width* × *height*, or diameter (φ) and thickness (t) if specified. The normalized power density (with unit of μW*s/(mm^3*m)), which is shown in the 5th column, is defined as (3), while the power coefficient, C_p defined as (4), is listed in the 6th column of Table 3.

From Table 3, one can observe that the largest harvested voltage can reach up to 30 V, while most of the macro-scale harvesters can only output several volts with the minimum output voltage of 80 mV. The largest output harvested power can reach 171 mW, while the minimum one is only 2 μW. The maximum normalized power density is 5.1 μW*s/(mm^3*m) for one electromagnetic generator based on aeroelastic mechanism [91] and the maximum power coefficient is 8.13% for a rotational electromagnetic-based generator [92]. Among these macro-scale wind energy harvesters, the rotational mechanism tends to be less popular in comparison with the aeroelastic mechanism for trapping wind flow. Both electromagnetic and piezoelectric power generation

techniques are popular for this group of portable wind energy harvesters. Moreover, a majority of the macro-scale harvesters can provide several milliwatts of output electrical power.

Table 3. Macro-scale portable wind energy harvesters (EM stands for electromagnetic and PZ means piezoelectric).

Ref	Size [mm]	Voltage	Peak Power	Normalized Power Density [μW *s/(mm^3*m)]	Power Coef. C_P [%]	Wind Speed [m/s]	Gen. Tech.	Mech. Mechanism
[57]	φ = 76.2	0.15 V	651 μW	-	-	17.5	EM	Rotational
[92]	φ = 76	-	6 mW	-	8.13	3	EM	Rotational
[93]	76.7 × 12.7 × 2.2	8.8 V	155 μW	0.01	0.09	6.7	PZ	Aeroelastic
[59]	φ = 80, t = 10	1.60 V	27.14 mW	0.1	5.7	5.4	EM	Aeroelastic
[88]	φ = 80, t = 170	80 mV	2 μW	1.7E-7	2.4E-5	14	PZ	Aeroelastic
[74]	90 × 10 × 0.6	12 V	145 μW	0.08	0.63	3.5	PZ	Aeroelastic
[49]	100 × 60 × 30	-	4 mW	0.006	1.73	4	PZ	Aeroelastic
[89]	141 × 100 × 55	3.8 V	573 μW	1.8E-4	0.11	4	EM	Aeroelastic
[94]	150 × 30 × 0.6	-	8.4 mW	0.4	0.61	8	PZ	Aeroelastic
[95]	150 × 30 × 1.1	-	6 mW	0.15	0.43	8	PZ	Aeroelastic
[96]	152.4 × 18 × 0.305	-	9.5 μW	0.007	0.12	1.69	PZ	Aeroelastic
[90]	161 ×250 × 0.635	30 V	53 mW	0.4	1.6	5.18	PZ	Aeroelastic
[20]	200 × 15 × 0.8	-	4.5 mW	0.191	0.26	9.8	PZ	Aeroelastic
[86]	203.2 × 50.8 × 50.8	2.1 V	-	-	-	7	EM	Aeroelastic
[97]	209 × 24 × 1	32 V	4 mW	0.073	0.1	11	PZ	Aeroelastic
[98]	254 × 254 × 0.381	-	2.2 mW	0.011	0.011	7.9	PZ	Aeroelastic
[99]	325 × 36.2 × 0.267	30 V	1.14 mW	0.077	0.15	4.69	PZ	Aeroelastic
[91]	490 × 20 ×0.2	6 V	70 mW	5.1	3.46	7	EM	Aeroelastic
[100]	620 ×290 × 750	6 V	171 mW	6.3E-5	0.02	20	EM	Aeroelastic
[87]	1000 × 25 × 0.2	3.3 V	7 mW	0.47	1.72	3	EM	Aeroelastic

2.3.2. Micro-Scale Harvesters

Micromachining technology is the key of manufacturing a device in tiny dimension. The cooperation between micro-mechanical parts, which are fabricated by micromachining techniques, and micro-electrical parts offer MEMS devices. Inertial sensors, which can be used for navigation

purpose, have always seen their successful MEMS applications for consumer electronics [101]. Wind energy harvesting in micro-scale dimension can be also offered by using this technology.

Micromachining technology is able to produce micro wires with multiple turns as coils in the electromagnetic-based energy harvesters. Micro-scale electromagnetic energy harvesting based on the aeroelastic mechanism from low-frequency ambient vibration was introduced by Sari *et al.* [102], who proposed a wideband electromagnetic micro-power harvester by using several cantilevers with varied lengths. The micro wiring was located around the surface of the cantilevers. The fabrication process of the proposed energy harvester required 5 masks for patterning. It had a square shape with one opening in the centre for locating the magnet. Although the limit of cantilever length may shrink the amount of the generated power, this effect can be alleviated by increasing the number of cantilevers. Park *et al.* [103] proposed a micro-electromagnetic harvester for collecting energy from low-frequency ambient vibration. In this study, spiral spring was patterned on silicon wafer by using the bulk micromachining technology. Multi-turned copper micro-coil was manually added and NdFeB magnet as inertial mass was fixed on the spring. As a result of ambient vibration, the spring moved and the magnet would move accordingly. Thus, electrical power could be induced in the copper coil. The total size of the fabricated micro-power harvester was 10×10×6 mm^3, which could generate 115.1 μW power and 68.2 mV load voltage when variation was 0.57 g (g=9.8 m/s^2) at 54 Hz.

Table 4 summarizes the previously published micro-scale portable wind energy harvesters by listing their geometry sizes, harvested electrical voltages, harvested electrical powers, normalized power densities, power coefficients, wind speeds, power generation techniques, and mechanical mechanisms for wind flow trapping. By default the harvester geometry size is given in the form of *length* × *width* × *height*, or diameter (φ) and thickness (t) if specified. Compared to the macro-

scale harvesters, one can read that the micro-scale portable wind energy harvesters normally output less harvested voltage and power. The maximum harvested power is 130 mW and the maximum power coefficient is 9.4% for an electromagnetic wind energy harvester based on the rotational mechanism, which was however measured at high wind speed (11.83 m/s) [104]. The maximum normalized power density is 3.1 μW*s/(mm3*m) for an electrostatic wind energy harvester based on the aeroelastic mechanism. This somehow helps exhibit that the electrostatic power generation technique based on the aeroelastic mechanism is advantageous for the micro-scale wind energy harvesters. Furthermore, the piezoelectric-based power generation technique working with the aeroelastic mechanism for wind flow trapping, such as [105], can be considered as another promising option for the micro-scale wind energy harvesters. Generally the electromagnetic-based wind energy harvesters along with the mechanical rotational mechanism have higher power coefficients than the others. Moreover, both electromagnetic- and piezoelectric-based techniques are popular in the designs of micro-scale wind energy harvesters.

Table 4. Micro-scale wind energy harvesters (EM stands for electromagnetic, PZ means piezoelectric, and ES represents electrostatic).

Ref.	Size [mm]	Voltage	Peak Power	Normalized Power Density [μW*s/(mm^3*m)]	Power Coef. C_P [%]	Wind Speed [m/s]	Gen. Tech.	Mech. Mechanism
[29]	2 × 1.65 × 0.005	24 mV	34 nW	0.39	0.012	5.2	PZ	Aeroelastic
[106]	3 × 0.3 × 0.008	18.1 mV	3.3 nW	0.03	1.6E-4	15.6	PZ	Aeroelastic
[107]	3 × 8 × 0.035	965 mV	2.27 μW	0.17	0.004	16.3	PZ	Aeroelastic
[58]	12 × 12 × 6	81 mV	-	-	-	-	EM	Aeroelastic
[58]	φ = 19, t = 5	4 mV	-	-	-	5	EM	Aeroelastic
[108]	φ = 20	-	4.3 mW	-	2.3	10	EM	Rotational
[109]	23 × 4 × 0.130	1.6 V	0.64 μW	0.004	3.4E-4	15	PZ	Aeroelastic
[65]	φ = 32	-	2.5 mW	-	1.51	7	EM	Rotational
[26]	φ = 40, t = 10	-	1.8 mW	0.01	0.24	10	ES	Rotational
[110]	φ = 40	0.6 V	16 mW	-	2.11	9	EM	Rotational
[104]	φ = 42	-	130 mW	-	9.4	11.83	EM	Rotational
[67]	47 × 20 × 0.5	13 V	613 μW	-	-	200 r/min	PZ	Rotational
[111]	75 × 60 × 30	5.2 V	60 mW	0.02	0.39	18	EM	Rotational
[63]	50 × 15 ×0.030	200 V	2.1 mW	3.1	0.29	30	ES	Aeroelastic
[112]	58 × 10 × 0.202	4.3 V	30 μW	0.05	0.06	5	PZ	Aeroelastic
[113]	φ = 53	5 V	7.5 mW	-	6.32	4.47	PZ	Rotational
[85]	60 × 40 × 0.06	34 V	1.73 mW	0.71	0.03	17	PZ	Aeroelastic
[114]	φ = 63, t=41	4.68 V	10 mW	0.02	5.2	4.67	EM	Rotational
[115]	φ = 68, t = 30	70.90 V	9.30 mW	-	-	-	PZ	Aeroelastic
[105]	69 × 37 × 0.24	3.3 V	1 mW	0.81	8.1	2	PZ	Aeroelastic
[80]	72 × 16 × 0.41	3.7 V	615 μW	0.2	0.2	7	PZ	Aeroelastic
[116]	75 × 20 × 0.004	1.2 V	0.98 μW	0.041	0.002	3.9	PZ	Aeroelastic

It tends to be true that the mechanical rotational mechanism for portable wind energy harvesters cannot be achieved by the micromachining technology due to the required fans or blades in the integrated rotation-based wind energy harvesters. Although some parts of the rotational structure, e.g., piezoelectric cantilevers or micro-scale coils, are possible to be fabricated by the micromachining technology, the manufacturing of the whole devices seems impractical at the moment. Nevertheless, the advantage of the rotational mechanism in terms of the beneficial power conversion efficiency is definitely obvious compared to the aeroelastic mechanism. On the other

hand, a micro-scale wind energy harvesting device may be offered by using piezoelectric generators based on the aeroelastic mechanism thanks to the perfect co-existence capability between piezoelectric materials and micromachining technology. Zhao *et al.* [117] proposed a micro vibration energy harvester, which was fabricated by using multiple piezoelectric cantilevers with AlN as the piezoelectric material. The film layers were deposited on a silicon wafer by using the magnetron sputtering technique. Eventually the proof mass on each cantilever and other suspending patterns were released by utilizing deep-reactive ion etching. Five piezoelectric cantilevers were used as an array to generate electrical power of 3.315 μW. The schematic of this energy harvester is depicted in Fig. 15. Furthermore, some other micro energy harvesters by using micromachining process based on the aeroelastic mechanism have been reported in [54] and [29].

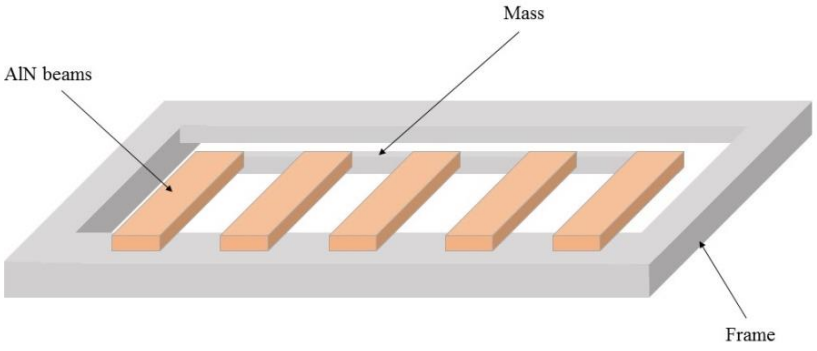

Fig. 15. Schematic diagram of 5 AlN cantilevers as an array for energy harvesting.

Figure 16 illustrates various features among the portable wind energy harvesters that are reviewed in this chapter. It helps exhibit the common features of the energy harvesters along the historical timeline. In this figure, the horizontal axis represents the timeline in years 2004-2016 and the vertical axis covers the information of electrical power generation techniques and device physical dimensions. For each electrical power generation technique, increasing Y amount stands for the increment of the normalized power density. According to Fig. 16, the portable wind energy

harvesting research and development started with the rotational mechanism, and afterwards the wind energy harvesting based on the aeroelastic mechanism was developed. Since 2013, the piezoelectric technique for the portable wind energy harvesting has become popular. The piezoelectric technique has been widely used in not only macro-scale, but also micro-scale wind energy harvesters. Most recently, the electrostatic technique shows some capability in either aeroelastic or rotational mechanism for wind energy harvesting. Furthermore, by considering the used mechanisms for wind flow trapping in the prior studies, one may observe that the rotational mechanism is less popular than the aeroelastic mechanism, although the former can more effectively extract power from wind flow. Moreover, one can also find that the micro-scale wind energy harvesters have been increasingly developed in the most recent years. In the near future, we may expect that this trend would be continuing to fit for ultra-low-power electronic applications until some commercial micro-scale wind energy harvesting products get available in the market.

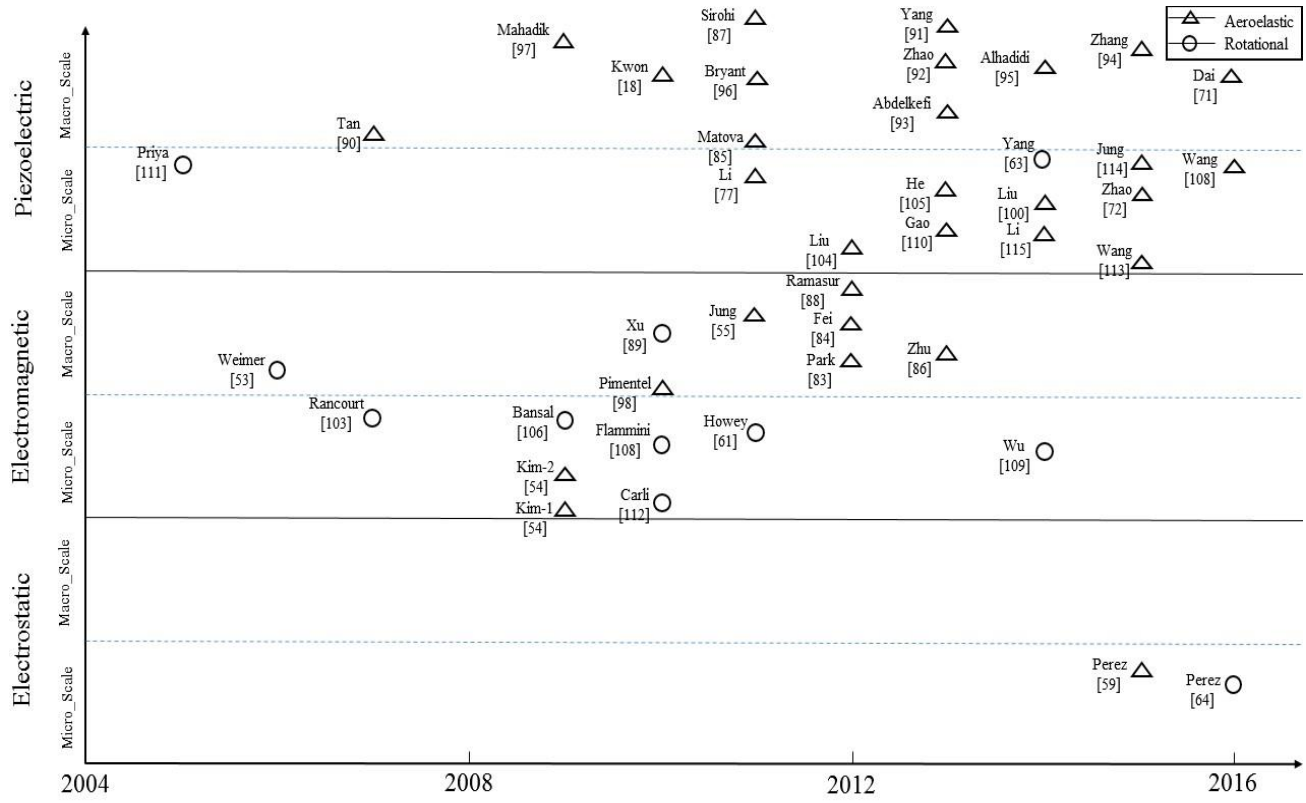

Fig. 16. An overview of the surveyed portable wind energy harvesters.

2.4. Power Management Systems

Due to small dimension of the portable energy harvesters, the generated electrical power normally has extremely low magnitude, which most of the time is not suitable for practical electronic applications. Therefore, modifying the magnitude is a vital step. Moreover, a direct use of the harvested electrical power is typically impossible due to its AC nature, which needs to be converted to a DC power supply. Therefore, power management systems (PMS) play an important role in conditioning the output voltage or current magnitude and meanwhile providing the DC signals.

The purpose of PMS can be satisfied by a charge pump circuit, also known as a voltage multiplier (VM), whose major configuration is Villard [118]. This voltage multiplier operates with at least two capacitors where one capacitor is charged and the other one is discharged in the first half cycle of the AC input signal and vice versa during the second half cycle. The number of circuit stages specifies the multiplication level of the original signal. Similar to a rectifier circuit, the voltage multiplier outputs a DC voltage, whose power can be simply stored within a super-capacitor. Eventually, any electronic application devices (such as microcontrollers) can draw the required power from the super-capacitor, which can be recharged continuously [119].

The simplest scheme to convert the generated AC signals to DC ones is to use the standard AC-DC circuitry as depicted in Fig. 17, which includes a full wave bridge rectifier and a filter capacitor. Four diodes are connected in the bridge configuration to provide unidirectional voltage output. In each cycle only two diodes are forward biased, while the other two diodes are reverse biased. Thus, during each input signal cycle, electrical current is only through one pair of diodes as well as load resistor *R*. In addition, to reduce the ripple on the output voltage, a filter capacitor *C* is used. The experimental validation conducted by Zargarani and Mahmoodi for wind energy harvesting using a piezoelectric flag [120] shows the output power would be reduced as a result of voltage drop across the non-ideal diodes in their forward-biased mode. Since 1N4001 diodes were used with 1V forward bias, a total of 2V voltage drop across the forward-biased diodes existed in the circuit before reaching the output due to the connection of two series diodes.

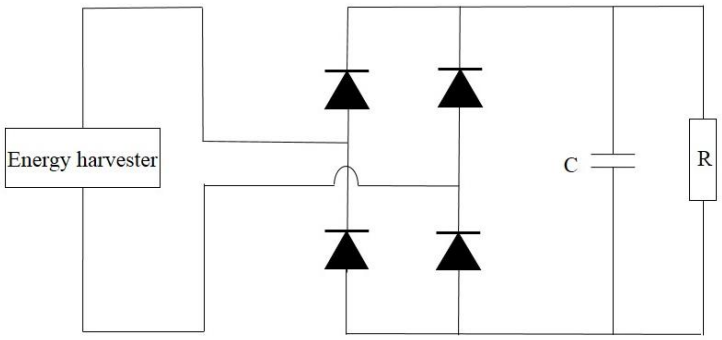

Fig. 17. The standard AC-DC circuitry.

Tan *et al.* [121] optimized a power management system for their wind energy harvesting devices. An active rectifier, as shown in Fig. 18, with MOSFET transistors instead of the standard diode bridge was developed. The rectifier bridge was composed of a pair of P-type MOSFETs and a pair of N-type MOSFETs. The ON-state voltage drop across each pair of transistors was quite low so that the efficiency could be improved from 40% to 70%. Then a DC-DC boost converter with resistor emulation algorithm took over to perform maximum power point tracking (MPPT) to extract maximum power from wind energy harvesters. As the last stage of the proposed power management system, a super-capacitor was utilized as a power storage unit. The experimental data in this study shows that over the range of wind speed from 2.3 to 8.5 m/s, the efficiency of the MOSFET-based active rectifier is on average 15%–25% higher than the diode-based passive rectifiers.

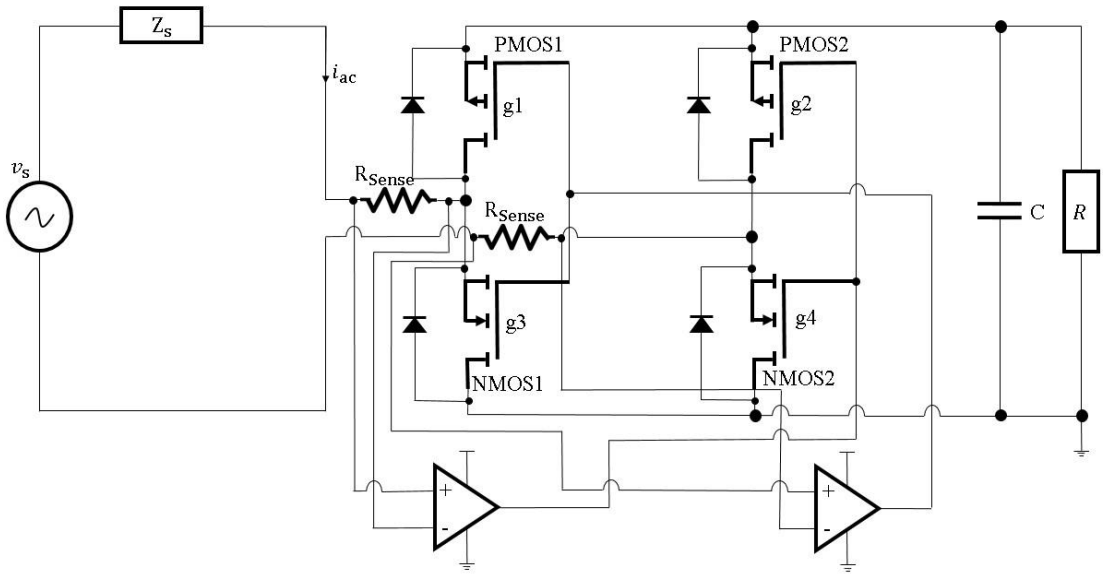

Fig. 18. Schematic diagram of the active rectifier bridge.

Another configuration for AC-DC converter that has been used for piezoelectric-based energy harvester is synchronous charge extraction (SCE) interface circuitry. As illustrated in Fig. 19, the accumulated electrical charge is periodically removed from the energy harvester (C_{pz}) and transferred to the load. The energy harvesting with this method consists of two features: firstly extraction phases are synchronized with stimulation forces, secondly the energy harvester itself is considered as an open circuit configuration [122]. An SCE circuit, which has an inductive path in comparison with the standard AC-DC circuit, is composed of a switching component *S*, an inductor *L*, and a diode *D*. When the harvester vibration displacement reaches the extreme position under the stimulation force, C_{pz}'s voltage climbs to its peak value. Then switch *S* is turned on so that the energy accumulated in capacitor C_{pz} is extracted to inductor *L* through *LC* oscillation (composed of *L* and C_{pz}). After passing a certain time (i.e., a quarter of *LC* oscillation cycle), capacitor voltage

V drops to 0 and inductor *L*'s current reaches its maximum value. Then, switch *S* is turned off, and inductor *L* freewheels through diode *D* and capacitor *C*.

Shi *et al.* studied an efficient self-powered SCE interface circuit for piezoelectric-based energy harvesters [123]. Their work confirms that the stimulation force frequency should be less than *LC* oscillation frequency in order for a SCE circuit to function well. In [124], Zhao and Yang investigated analytical solutions for galloping-based piezoelectric energy harvesters with various interfacing circuits. Their analytical and experimental results show that the power, voltage and vibration displacement are independent of load resistance, which is known as a feature of SCE interface circuits. Moreover, the comparison between standard AC-DC and SCE circuits indicates that the SCE circuit has higher output power than the standard AC-DC one under small electromechanical coupling factor condition of piezoelectric materials.

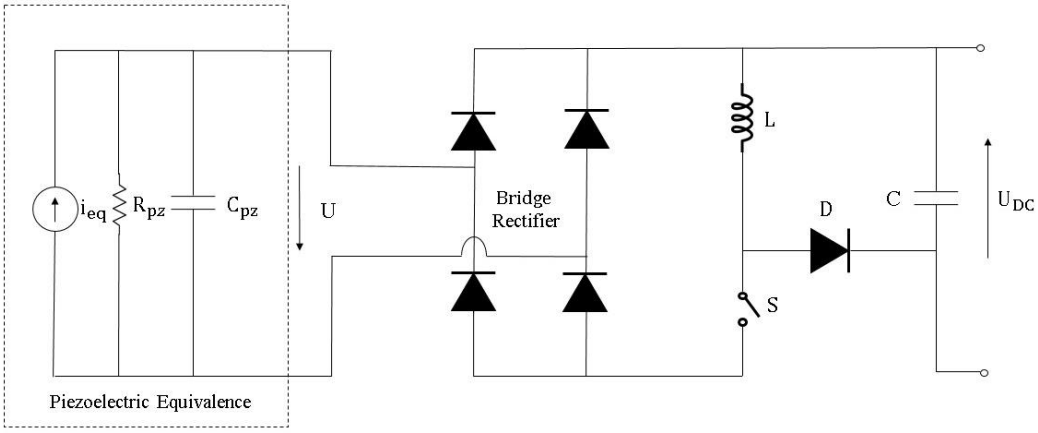

Fig. 19. Synchronous charge extraction (SCE) circuitry.

Wei *et al.* developed a power management circuit with a simple structure for electrostatic energy harvesters [125]. The proposed circuit, as shown in Fig. 20, is only composed of diodes and capacitors. This interfacing circuit includes a source capacitor C_{var}, which represents electrostatic generators, a biasing capacitor C_{bias}, a storage capacitor C_{store}, a pair of rectifier

diode D1 and D2, and a voltage multiplier with cells 1, 2 up to *n*. The operation of this circuit consists of two phases. In the first phase, C_{var} decreases due to the discharge through the path of C_{var}, C_{bias}, D1 and C_{store}. In the second phase, C_{var} increases due to the charge with the path of D2, C_{bias} and C_{var}. Therefore, the maximum voltage of C_{var} is equal to (*n*+1) times of V_{Cstore} when C_{var} reaches its minimum value, whereas the minimum voltage of C_{var} is equal to *n* times of V_{Cstore} when C_{var} has its maximum value. The experimental results of this study showed that the efficiencies of over 75% were measured for the harvested power ranging from 13 nW to 75 nW.

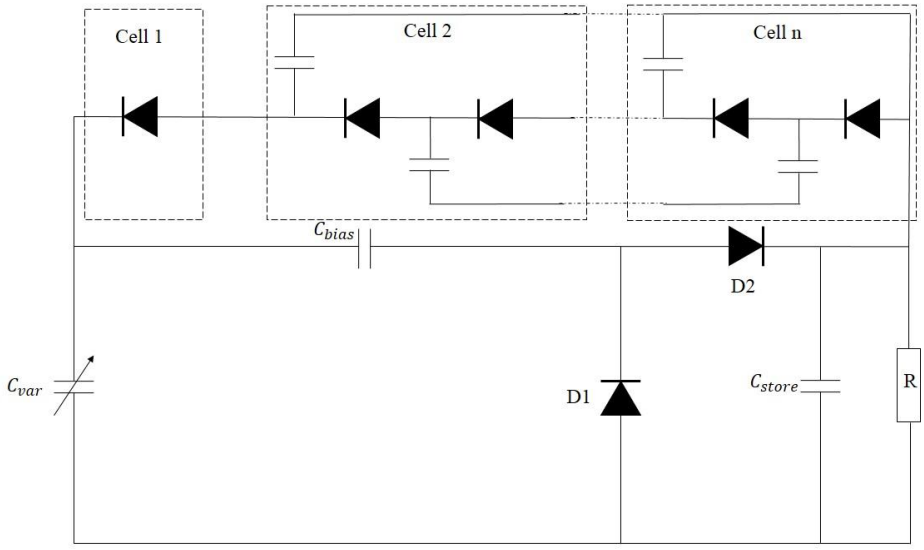

Fig. 20. Interface circuit for electrostatic-based energy harvesters.

Currently some companies, such as Linear Technology [126] and Infinite Power Solution[127], offer integrated kits for converting AC to DC voltage and storing the rectified voltage in super-capacitors. For instance, the low-loss bridge rectifier from Linear Technology has a total voltage drop of about 400 mV under typical piezo-generated currents (~10μA) and high rectifying conversion efficiency up to 90%. Moreover, typical charge loss of Infinite Power

Solution products (e.g. MEC125, MEC120, and MEC) is 2% per year. The stored electrical energy in super-capacitors can be delivered upon the request of power-consuming devices. Thus, the super-capacitors can be repeatedly charged until the electrical power reaches a certain level for practical power supply.

2.5. Summary

In this chapter a comprehensive survey on recent portable vibration energy harvesting devices has been conducted. Vibration energy harvesters can be categorized into the following three groups in terms of the used power generation techniques: piezoelectric-based harvesters by utilizing the direct effect of piezoelectric materials, electromagnetic-based harvesters by leveraging magnetic flux density changes, and electrostatic-based harvesters by utilizing capacitance variation. In addition, the vibration from wind flow can be collected with the following two mechanical approaches: rotational and aeroelastic mechanisms. The aeroelastic mechanism consists of two groups, vortex-induced vibrations and movement-induced vibrations. Furthermore, considering their physical dimensions, the portable wind energy harvesters are also classified into macro-scale and micro-scale ones. As the generated power amount is strongly dependent on the device size, the macro-scale energy harvesters can typically produce more power than the micro-scale ones.

The current status of research and development exhibits that the aeroelastic mechanism is promising for portable wind/vibration energy harvesting mainly thanks to simple structure and ease of fabrication, while the rotational mechanism is quite effective for extracting power from wind flow. The aeroelastic mechanism, which can only operate with good power conversion efficiency when wind flow direction is perpendicular to the structures, should be improved for omnidirectional function by deploying some new symmetric structures. The combination between

piezoelectric power generation technique and micromachining fabrication technology can offer a wide range of wind/vibration energy harvesters with high portability and reasonable output power. Thus, we expect to see numerous studies in this direction related to piezoelectric materials in the near future.

Chapter 3 Design and Optimization of Piezoelectric MEMS Vibration Energy Harvesters Based on Genetic Algorithm

3.1. Introduction

In the recent decade, several approaches to improve energy conversion efficiency for the MEMS piezoelectric energy harvesters have been presented. Gao *et al.* [112] proposed a new piezoelectric energy harvester that is attached with an external cylindrical object made of photo paper to adjust the resonant frequency and magnitude of the output voltage. This study clearly demonstrates that different sizes of extension objects (e.g., a cylindrical one) can impact on the characteristics of harvester output. Another technique to improve efficiency of the MEMS piezoelectric energy harvester, which was presented by Jung *et al.* [105], is to modify the location of piezoelectric film along the beam surface by selecting an area closer to the anchor side. In addition, Jia and Seshia [128] proposed to enhance the efficiency of the MEMS piezoelectric harvesters by tuning proof mass size as a practical approach. It was found that an end mass occupying about 60%–70% of the total cantilever length is optimal for linear response. Furthermore, Ibrahim *et al.* [129] proposed a new structure with a magnetic oscillator around the piezoelectric cantilever tip in order to enhance the harvested voltage magnitude. The comparison between the proposed device and the conventional piezoelectric energy harvesters shows that the harvested voltage was enlarged by a factor of 2.8 at the magnetic oscillator speed of 2 m/s (i.e., meters/second).

However, all the techniques above are solely based on the designers' experience and skills in making a wise decision, which means they have to spend a considerable amount of time to gain optimum design. To address this difficulty, Sunithamani *et al.* [130] proposed an optimization method by using variant-mesh analysis, which aims to run numerous simulations to investigate the effect of harvester geometry changes on its performance. Furthermore, in a recent study [131], analyzing geometric parameters by incrementing the harvester aspects to produce a correlation matrix was presented as a solution to MEMS piezoelectric harvester optimization. However, requiring a large amount of time to complete finite element method (FEM) simulations as well as acute human observation makes these methods less efficient for optimizing a number of physical parameters of MEMS piezoelectric energy harvesters. Thus, a proper design automation technique is essential for the MEMS piezoelectric harvester designers to be liberated from the conventional laborious trial-and-error effort. Therefore, in this chapter we are motivated to utilize some design automation techniques to address this pressing challenge during the design process of the MEMS piezoelectric energy harvesters.

In the literature various approaches for optimization of MEMS structures have been presented [101]. Tabatabaei *et al.* [132] proposed an Artificial Immune System (AIS) method for piezoelectric energy harvester shape optimization. However, this method offers an energy harvester with unusual shape that cannot be readily fabricated with regular MEMS fabrication technologies. Moreover, the proposed AIS optimization approach is less efficient in comparison with the other optimization methods [133]. Kim *et al.* [134] presented a Computational Experiments (CE) method for design automation, by which a prototyped device was first tested and then the FEM simulation parameters were corrected upon the obtained experimental results. After performing this calibration, the objective function for maximizing the harvested voltage at

low frequency was utilized in the process of tuning the piezoelectric cantilever dimensions. Since this proposed method needs prototyping-based calibration, fabricating energy harvesters two times make it somehow impractical. On the other side, Genetic Algorithm (GA), an evolutionary optimization approach, was used to enhance the magnitude of the voltage harvested from traffic roads [135]. However, the proposed objective function in this study is dependent on natural properties of the piezoelectric materials (e.g., piezoelectric coefficient, internal capacitance of piezoelectric, etc.), which designers cannot modify during fabrication process. Thus, considering a fitness function with optimizable variables but without a need of prototyping-calibration is highly demanded.

To overcome these aforementioned challenges, we propose a new design automation method based on GA in this chapter. The contributions of this chapter include the following:

- We validate the accuracy of the analytic model for MEMS-based unimorph piezoelectric energy harvesters with FEM simulation and prototype measurement;
- We propose a GA-based automated design optimization methodology with minimum human efforts for MEMS-based unimorph piezoelectric energy harvester design;
- We also investigate and analyze various effects of physical parameter changes on the mechanical and electrical properties of the MEMS energy harvesters.

The major work in this chapter has been formally documented in multiple journal and conference papers (as listed in the Appendix [Journal-2][Conference-1]).

3.2. Analytic Modeling of Unimorph Piezoelectric Energy Harvesters

The piezoelectric materials, which are used to fabricate sensors and actuators [136], have crystal structure. By applying mechanical force on the surface, the structure changes to generate electrical voltage. This unique property makes them useful for converting mechanical vibration to electrical power, and vice versa for mechanical deformation if an external electrical power is applied. Since kinetic energy of vibration provides periodic deformation on the piezoelectric structure, an AC electrical voltage can be collected from its surface. In order to collect electrical voltage from the piezoelectric film, two different configurations for electrode deposition (i.e., capacitor-style and interdigitated-style) can be utilized [137]. In this study, due to our manufacturing restriction, we can only deposit capacitor–style electrodes in our MEMS unimorph piezoelectric energy harvesters. Thus, according to the IEEE standard on piezoelectricity with the special consideration of our electrode deposition, the generated voltage by piezoelectric materials is proportional to the observed stress on their structure with the following conversion relationship (22) [138]:

$$\mathrm{V} = \mathrm{g}_{31}\mathrm{t}_{\mathrm{p}}\sigma_{\mathrm{p}}, \tag{22}$$

where V is the generated voltage, g_{31} is the piezoelectric coefficient with an assumption of dominant stress in the in-plane direction and zero stress in the out-of-plane direction, t_p is the piezoelectric film thickness, and σ_p is the applied stress on the piezoelectric material. Since stress can lead to strain inside the material, their general conversion can be expressed by the following when the object is restricted to move only in one direction (i.e., the in-plane direction):

$$\varepsilon_p = \frac{\sigma_p}{Y_p}, \tag{23}$$

where ε_p is the observed strain inside the piezoelectric material, and Y_p denotes the Young's modulus of the piezoelectric material. Since the prevalent rectangular-shaped piezoelectric energy harvesters are compatible with the regular MEMS fabrication process, this chapter is focused on such harvesters. Typically the piezoelectric vibration energy harvesters can be offered in two different configurations: bimorph and unimorph. In the bimorph configuration, piezoelectric material is deposited on two sides of the beam (or called cantilever, both of which terms are exchangeable throughout this chapter) by bonding approaches (e.g., gluing or hot air pressure) for centimeter-scale piezoelectric energy harvesters [18]. Due to the limitation of regular MEMS fabrication process in deposition of piezoelectric material on two sides, the unimorph piezoelectric energy harvesters, which includes the piezoelectric film only on one side, features sound advantages for producing energy harvesters in the micrometer scale [139]. Therefore, this chapter is aimed at exhibiting the design automation benefits for the unimorph piezoelectric energy harvesters. The structural diagram of the unimorph piezoelectric energy harvester is displayed in Fig. 21.

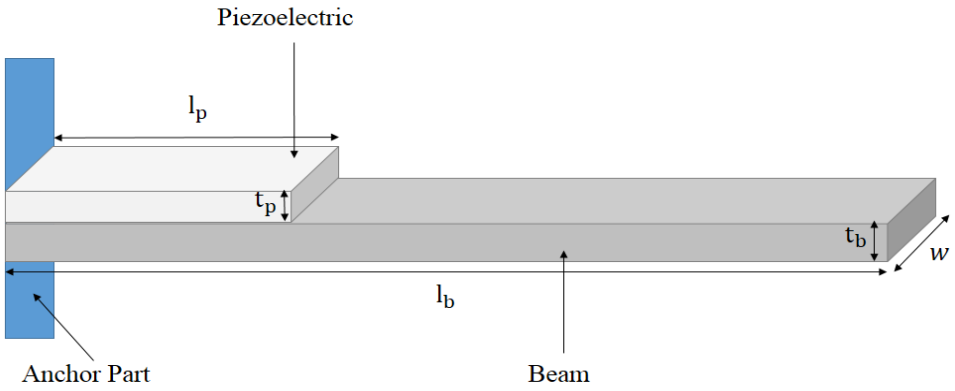

Fig. 21. Structural diagram of the unimorph MEMS piezoelectric energy harvester with deposition of piezoelectric film on the beam surface close to the anchor side.

In the literature, the analytic models, which can estimate the harvested voltage from the piezoelectric energy harvesters, can be categorized into the following three: pin-force model, enhanced-pin-force model, and Euler-Bernoulli model. The pin-force model assumes the piezoelectric film is attached to the beam as a pin connection. The strain on the beam, which linearly increases through the beam thickness, is computed by the Euler-Bernoulli beam theory, whereas the strain on the entire piezoelectric film is considered to be constant. Obviously this model does not consider the bending stiffness of the piezoelectric material. The enhanced-pin-force model actually improves the pin-force model by taking into account the bending stiffness of the piezoelectric material. In this regard, the strain on the piezoelectric material, which is not constant any longer but linearly increases, is determined by the beam deformation. In comparison with the two models above, the Euler-Bernoulli model features the highest modeling accuracy. Since this model assumes the beam and piezoelectric film are perfectly bonded together, their deformation should be represented with reference to the new common neutral axis [140][141][142]. Thanks to this advantage, in this chapter we utilize the Euler-Bernoulli model for the design optimization purpose.

The Euler-Bernoulli model schematic is depicted in Fig. 22. In this model, the bonding adhesive material has no impact on the beam stiffness or mass. Moreover, it is assumed that the piezoelectric film is homogenous, transverse isotropic, elastic, and thin compared to the beam.

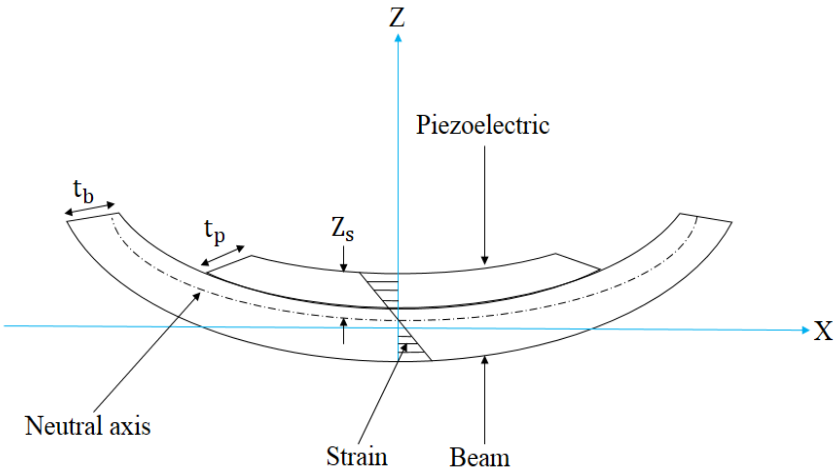

Fig. 22. Schematic of the Euler-Bernoulli model with an assumption of perfect bonding between beam and piezoelectric film.

By using the method of transformed section [143], we can transfer the two-layer piezoelectric energy harvester into one unified structure (i.e., beam). The common neutral axis of the newly formed structure with the reference of the piezoelectric surface on the top can be computed by (24):

$$Z_s = \frac{\sum_{i=1}^{n} Z_i f_i A_i}{\sum_{i=1}^{n} f_i A_i} = \frac{\frac{t_p}{2} t_p \frac{Y_p}{Y_b} + [t_p + \frac{t_b}{2}] t_b}{t_p \frac{Y_p}{Y_b} + t_b}, \qquad (24)$$

where Z_s is the new common neutral axis, Z_i is the original neutral axis for the i^{th} material, f_i is the dimensionless transformation factor based on the ratio of piezoelectric film and beam Young's moduli, and A_i is the area of the i^{th} material. Constant n is the number of the composite materials, which is equal to 2 in this modeling application. And t_b is the beam thickness and Y_b is the Young's modulus of the beam.

Consequently, the strain on this transformed structure can be expressed by (25):

$$\varepsilon_p = -\frac{M}{\left(Y_p\, I_p + \, Y_b\, I_b\right)}\,(z_s - \frac{t_p}{2}), \qquad (25)$$

where *M* is the actuating momentum and the term of $(z_s - \frac{t_p}{2})$ indicates the distance between the neutral axis and the center of the piezoelectric film. The origin of this coordinate system in our analysis is assumed to be the neutral axis. I_p and I_b are the moments of inertia for the piezoelectric film and beam within the coordinate system in Fig. 22. They can be calculated by (26):

$$\begin{aligned} I_p &= \int_{Z_s - t_p}^{Z_s} w z^2\, dz = \frac{1}{3} w \left[Z_s^3 - \left(Z_s - t_p\right)^3\right], \\ I_b &= \int_{Z_s - t_b - t_p}^{Z_s - t_p} w z^2\, dz \qquad (26) \\ &= \frac{1}{3} w \left[\left(t_p + t_b - Z_s\right)^3 + \left(Z_s - t_p\right)^3\right], \end{aligned}$$

where *w* denotes the width of the beam or piezoelectric film. By substituting (24) and (26) into (25), we can derive the average strain on piezoelectric film as (27):

$$\varepsilon_p = -\frac{6\ Y_b\, t_b\left(t_b + t_p\right)}{w\left[Y_p^2\, t_p^4 + Y_b^2\, t_b^4 + 2 Y_p\, t_p\, Y_b\, t_b\left(2t_p^2 + 3t_p t_b + 2t_b^2\right)\right]} \times M. \qquad (27)$$

Eventually by using (23), we can also compute the average stress on the piezoelectric material. Then by applying it into (22), the harvested voltage from the unimorph piezoelectric harvester is equal to (28):

$$V = -\frac{6\, g_{31}\, t_p Y_p\ \ Y_b\, t_b\left(t_b + t_p\right)}{w\left[Y_p^2\, t_p^4 + Y_b^2\, t_b^4 + 2 Y_p\, t_p\, Y_b\, t_b\left(2t_p^2 + 3t_p t_b + 2t_b^2\right)\right]} \times M. \qquad (28)$$

In order to use (28) for estimating the harvested voltage, the actuating momentum, which is equal to (29), has to be computed,

$$M = (I_b Y_b)\hat{k}, \tag{29}$$

where $\hat{k}$ is the average of radius curvature. Based on the Euler-Bernoulli beam theory, the governing equation of the beam can be expressed by (30):

$$Y_b I_b \frac{\partial^4 d(x,t)}{\partial x^4} + \rho A \frac{\partial^2 d(x,t)}{\partial t^2} = F(t), \tag{30}$$

where ρ is the beam density, *A* is the cross-sectional area of the beam, *d(x,t)* is the deflection along the Z-axis as shown in Fig. 22, and *F(t)* represents the external excitation force on the beam, whose oscillation frequency is identical to the resonant frequency of the beam. Moreover, the radius curvature in terms of time *t* is equal to (31):

$$k(x,t) = \frac{\partial^2 d(x,t)}{\partial x^2}. \tag{31}$$

Eventually, the required average of radius curvature for momentum calculation in (29) can be calculated in (32),

$$\hat{k} = \frac{1}{l_p}\int_0^{l_p} k(x,t)\, dx\,, \tag{32}$$

where l_p denotes the length of the piezoelectric film.

Since the Euler-Bernoulli beam theory is used in the derivation above, the following prerequisites should be observed in order to ensure the highest accuracy of the final analytic modeling: (1) the ratio between the beam length and its thickness is greater than 10 [144]; (2) the ratio between the beam length and its width is greater than 2 [145]; (3) the piezoelectric film length is much greater than its thickness [146].

3.3. Single-Optimization-Based Genetic Algorithm

The Genetic Algorithm (GA) is an evolutionary computing method for searching and optimizing complex problems by mimicking biological evolution [147]. The GA starts its operation by generating some random numbers for a group of variables to maximize or minimize certain defined fitness function(s). The GA solutions are normally coded in binary string structure. During the computation, three different operators can be typically applied to the set of solutions to provide new evolutionary population. The flowchart of the GA mechanism is illustrated in Fig. 23 [148].

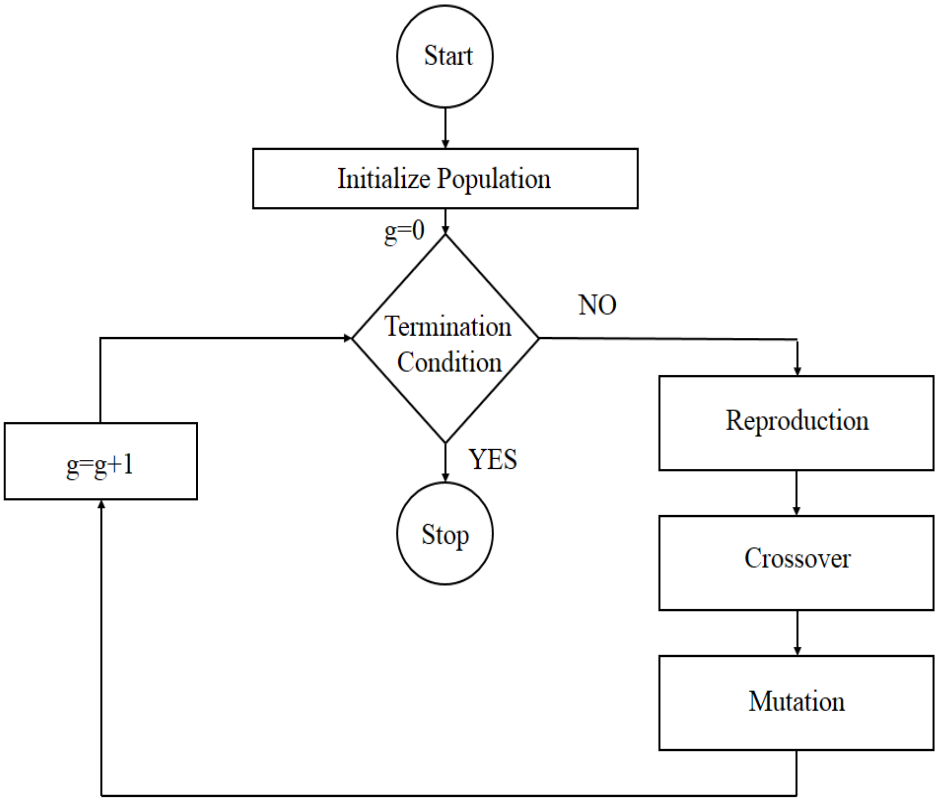

Fig. 23. The working mechanism flowchart of the single GA optimization method.

As shown in Fig. 23, GA starts with initialization, where the variables are coded in the form of fixed-length binary string. Each variable can be randomly selected with equal probability. Usually the first operator that performs on a population is reproduction, which strives to find appropriate strings in a population and interpolate them into a mating pool. A number of methods for string selection have been proposed in the literature, although the main idea is that certain preferable strings from the current population should be chosen, duplicated and inserted into the pool. The next operator within GA is crossover, where typically two strings are selected from the mating pool and a certain quota of these strings are exchanged in between. In other words, the recombination between string pairs produces new strings, called *offspring*. Finally, mutation operator is performed to change one bit from 1 to 0 or vice versa. This process is also random with a very low probability (called *mutation rate*) on the entire population. All the three operators are performed on the entire population in one GA generation, which is counted by *g* in Fig. 23. Thus, the search and optimization aspect of GA is mainly provided by the crossover and mutation operators. The multi-dimensional search capability offered by GA can effectively prevent it from being trapped by local optima [149]. Therefore, a significant feature of GA in comparison with the conventional optimization approaches is its advantageous access to the global optimum.

In this chapter, our proposed GA-based optimization method is performed to identify optimum physical aspects of the beam and piezoelectric film in the MEMS piezoelectric harvesters for the efficiency enhancement of energy harvesting. The coverage of the electrodes is defined to be identical to the size of the piezoelectric film. In the following section, the capability of the GA-based optimization methodology in efficiency improvement and its applicability to the micro-fabrication process will be discussed and demonstrated.

3.4. Experimental Results and Discussion

In order to evaluate accuracy of the presented analytic equations in Section 3.2 for harvested voltage of the unimorph piezoelectric energy harvesters, one piezoelectric energy harvester with the listed parameters in Table 5 was implemented in MATLAB (Version 2014) for analytic computation, while the other one with the same properties was simulated with COMSOL Multiphysics (Version 5.2) for finite element method (FEM). The comparison between the harvested voltages by using the analytic computation technique and the FEM simulation is shown in Fig. 24. One can observe that the proposed analytic computation after reaching the steady state (around 1.3ms) has high accuracy and reliability. Thus, we can ensure that such an analytic model has solid potential for being utilized in the magnitude estimation of harvested voltage from the unimorph piezoelectric energy harvesters. It should be noted that such high accuracy between analytic computation and FEM simulation can be attributed to the relatively simple structure of the unimorph piezoelectric energy harvesters and the applied Euler-Bernoulli beam theory. Moreover, our sufficient satisfaction of the accuracy-related prerequisites as listed in Section 3.2 is highly essential.

Table 5. The utilized parameters in the analytic computation and FEM simulations for a unimorph piezoelectric energy harvester.

Parameters	**Description**	**Value**
l_b	Beam length	3 mm
t_b	Beam thickness	200 um
Y_b	Young's modulus of beam	70 Gpa
ρ_b	Beam density	2700 Kg/m^3
l_p	Length of piezoelectric film	3 mm
t_p	Thickness of piezoelectric film	50 um

Y_p	Young's modulus of piezoelectric material	50 Gpa
ρ_p	Piezoelectric material density	7600 Kg/m^3
g_{31}	Piezoelectric material coefficient	-9.5e-3 V*m/N
W	Beam and piezoelectric film width	1 mm

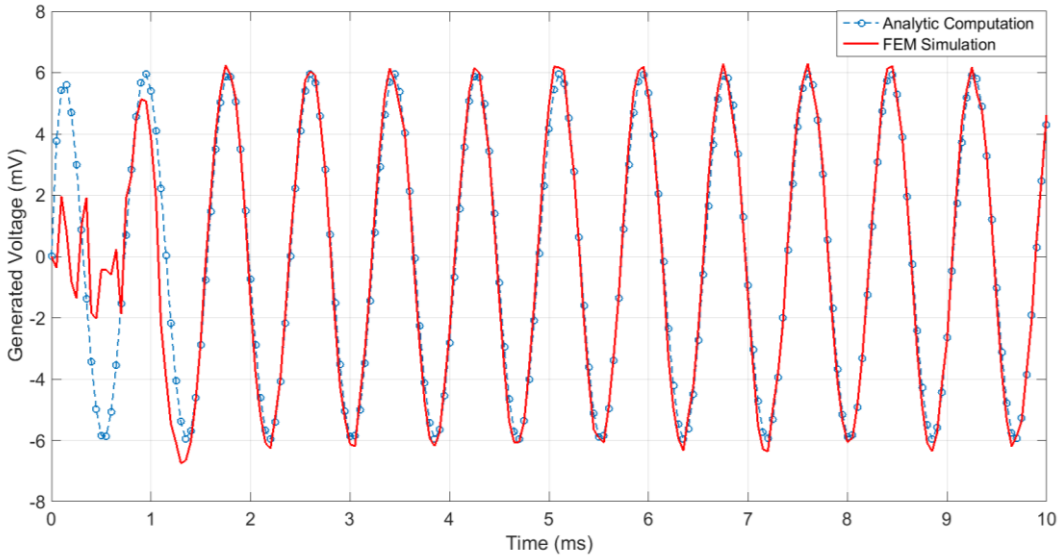

Fig. 24. Estimation of the harvested voltages from the unimorph MEMS piezoelectric energy harvester by using analytic computation and FEM simulation.

Since the analytic equations presented in Section 3.2 are able to accurately estimate the harvested voltage for the given harvester dimensions, we opt to utilize them in a fitness function of our GA optimization, which includes five physical variables defined as *optimizable parameters*, i.e., beam length (l_b), beam thickness (t_b), piezoelectric-film length (l_p), piezoelectric-film thickness (t_p), and beam or piezoelectric width (w). Note that we define the harvested voltage instead of the harvested power as our fitness function of GA. In this way, we can only focus on the physical geometry optimization of the harvesters, rather than having to consider any external

parameters (e.g., load impedance) additionally.

The proposed optimization method was implemented in MATLAB genetic algorithm toolbox to enhance the magnitude of harvested voltage besides device size reduction. The piezoelectric energy harvesters were excited with a sinusoidal vibration, whose amplitude of acceleration is 0.5g (1g=9.8 m/s^2) with a frequency identical to the resonant frequency specification of the corresponding energy harvester.

The applied fitness function and constraints of our GA optimization are defined by (33):

$$\begin{aligned} &\textit{Maximize}: \{\mathrm{V}\}\mathrm{Maximize}:\{\mathrm{V}\} \\ &\textit{Subject to}: \text{ design rules of the optimizable parameters} \end{aligned} \tag{33}$$

For all the five physical optimizable parameters (i.e., l_b, t_b, l_p, t_p, and w), upper and lower bounds are defined as per the design rule constraints as listed in the second row of Table 6. Moreover, the observed results by using a commercial product (i.e., COMSOL optimization module) for MEMS structural optimization are listed in the fourth row of this table (named as *Com-OPT*). To run the COMSOL optimization module, the geometry of any piezoelectric energy harvester in 3D space was first defined, and isotropic materials for both beam and piezoelectric film were considered. We selected the *Time Dependent Study* to measure the harvested voltage for 50ms with a time interval of 5ms. The optimization module is configured as follows: *Monte Carlo* as the optimization method, 600 as the maximum number of objective evaluations, and *objective maximization* as the optimization type. Further information regarding the COMSOL optimization module can be found in [150]. To demonstrate and compare the GA capability, GA was executed 4 times with the same generation size of 20 but with different population sizes ranging from 5 to 45, as shown in the rows of *OPT1-OPT4*. To make a comprehensive comparison, we also list the resonant frequency, generated peak voltage (V_{peak}) at a specific frequency, and runtime in Table 6.

Table 6. Un-Optimized and Optimized five physical aspects of the MEMS piezoelectric vibration energy harvesters by COMSOL optimization module and GA with different population sizes.

Parameter	**Beam Length l_b [μm]**	**Beam Thickness t_b [μm]**	**Piezoelectric Length l_p [μm]**	**Piezoelectric Thickness t_p [μm]**	**Beam Width w [μm]**	**V_{Peak} [mV] (Analytic)**	**V_{Peak} [mV] (FEM)**	**Resonant Frequency [KHz]**	**Population Size**	**Runtime [min]**
Range	[1000,5000]	[100,200]	[500,5000]	[10,50]	[500,2500]	-	-	-	-	-
Un-OPT	5000	200	5000	10	2300	7.6	6.5	7.08	-	-
Com-OPT	4998	196	4995	14	504	9.13	8.25	7.85	-	338
OPT1	2265	167	2237	18	905	2.9	2.1	29.03	5	10
OPT2	4029	114	500	49	970	18.6	17	7.29	15	65
OPT3	4923	111	636	50	864	27.14	25.8	4.58	30	180
OPT4	4891	115	500	50	1531	27.81	26.1	4.98	45	720

According to the listed data in Table 6, the un-optimized case, as named *Un-OPT*, had a large occupied area with extremely small V_{peak}. The optimized unimorph energy harvester by COMSOL optimization module, labeled as *Com-OPT*, could enlarge harvested V_{peak} by a factor of 27% in comparison with the un-optimized case, while it took 338 minutes in the computation. After the first GA optimization run (labeled as *OPT1*) with a small population size of 5, the generated V_{peak} was highly reduced in comparison with *Un-OPT* although the GA optimization process was done very quickly. By increasing the population size to 15, the required runtime was increased along with the energy harvesting efficiency. *OPT3* with a sufficiently large population size of 30 demonstrates that increasing the population size can help improve the magnitude performance of

the piezoelectric energy harvesters by a factor of 3.96 although more runtime is expected. It is worth noting that selecting a proper population size is highly critical for the GA optimization. As the data of *OPT4* shows, although an even larger population size is utilized, the runtime is significantly increased but the performance improvement in terms of V_{peak} is very little compared to *OPT3*.

On the other hand, the obtained results for *OPT3* show that the magnitude performance improvement was actually emerging on top of dimension reduction in several aspects, such as piezoelectric film length, beam thickness, and beam width. This is indeed highly desirable for MEMS piezoelectric design optimization. In addition, the comparison between the obtained data by using GA and COMSOL optimization module clearly demonstrates that GA has gained less runtime but with higher capability in energy harvesting efficiency improvement. Besides the computation results from the analytic equations, the eighth column in Table 6 also provides the FEM numerical simulation results for the harvested voltage magnitude by using COMSOL *Time Dependent Study*. It is found that both results above are in line with each other very well. In general, from Table 6 one can observe that a slim beam (i.e., larger length, smaller width, and thinner layer) may lead to larger magnitude of the harvested voltage. Moreover, a shorter and thicker piezoelectric film tends to contribute considerable improvement to the energy conversion for the MEMS unimorph piezoelectric energy harvesters.

As reflected from Table 6, the GA-based optimization method can successfully optimize a large number of free variables (i.e., five physical parameters) that the designers can select during the design process. However, for the most of the commercially accessible fabrication processes, the thickness of the layers (e.g., beam layer and piezoelectric layer) is normally fixed. In other words, the designers have no control on the thickness amount during the fabrication process. Thus,

to consider such manufacturing limitation, in this chapter we also performed the GA optimization and associated comparison on three harvester physical aspects (i.e., beam length l_b, piezoelectric film length l_p, beam and piezoelectric width w) as reported in Table 7. Moreover, several harvesters with the distinct physical aspects were fabricated by a micro-fabrication process and then verified by our experimental measurement.

3.4.1. Micro-Fabrication Process

The simplified fabrication process flow, which was utilized to fabricate our harvester prototypes, is sketched in Fig. 25. This process starts with 150 mm n-type double side polished Silicon-on-Insulator (SOI) wafers. The top surface of the silicon layer is doped by depositing a phosphosilicate glass (PSG) layer and being annealed at 1050°C for one hour in argon (as depicted in Fig. 25 Step-1). Thereafter, the PSG layer is removed via wet chemical etching. Then the piezoelectric film, 0.5 μm aluminum nitride (AlN), is deposited over the wafer by reactive sputtering technique (as depicted in Fig. 25 Step-2). Subsequently, the wafer is coated with photoresist and the piezoelectric film is lithographically patterned. After completion of this step, the top electrode, which includes 20 nm chrome and 1 μm aluminum, is deposited and patterned through a liftoff process. In the next step, the silicon layer is lithographically patterned, and Deep Reactive Ion Etch (DRIE) is performed to etch the silicon layer down to the oxide layer (as depicted in Fig. 25 Step-3). Then on the front side of the wafer, protection material is deposited (as shown in Fig. 25 Step-4). After the wafer is reversed, the substrate is lithographically patterned and etched by using RIE and DRIE methods. Eventually the deposited protection material on the front side is stripped by using a dry etch process. As shown in Fig. 25 Step-5, this MEMS process can release our clamped unimorph piezoelectric harvester prototypes.

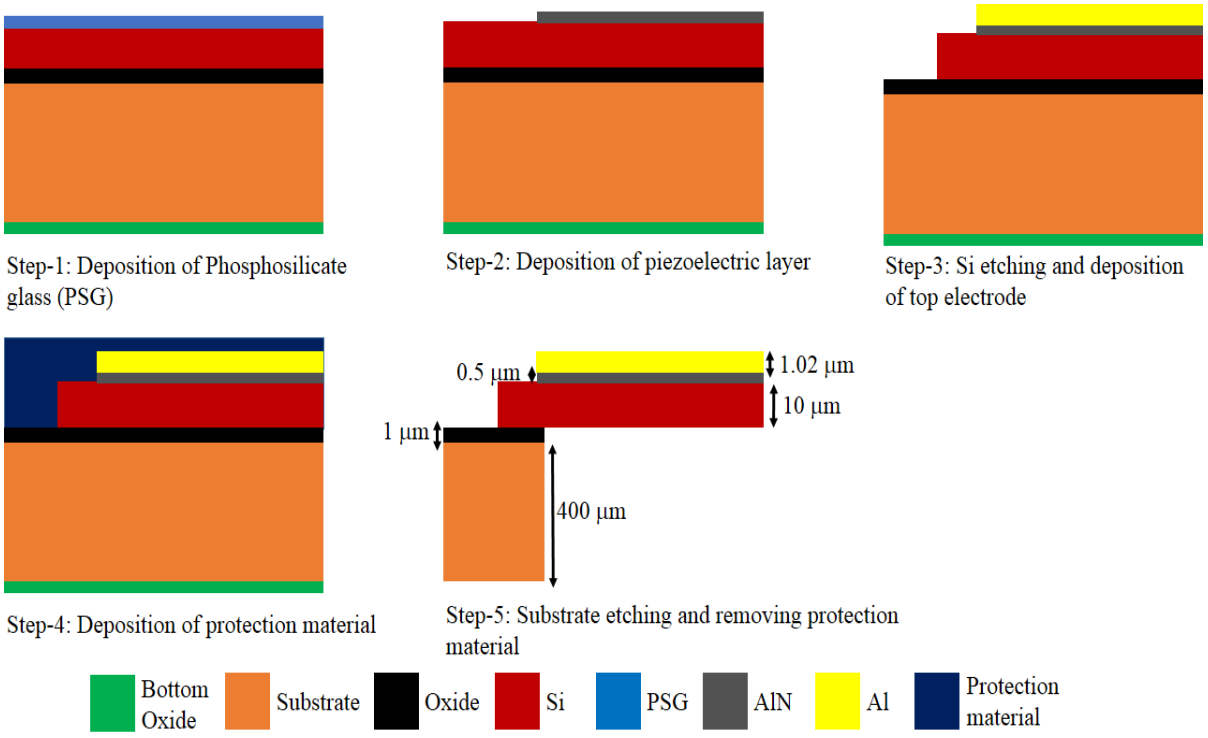

Fig. 25. Fabrication process flow for manufacturing our MEMS unimorph piezoelectric energy harvesters.

3.4.2. Experimental Results

In Table 7, the coverage ranges for the three optimizable parameters based on the design rule constraints and our budgetary chip plan are listed. It is worth mentioning that the size of an un-optimized harvester, labeled as *Un_OPTF*, is selected with the maximum allowable sizes in all the dimensions. The COMSOL optimization module result, labeled as *Com_OPTF*, is listed in the fourth row of Table 7. On top of the GA optimization study from Table 6, two promising evolutionary population sizes of 15 and 30 were selected to perform GA-based optimizations in the new scenario here as listed by *OPTF1* and *OPTF2*, respectively. Table 7 includes the peak harvested voltage magnitude from the analytic computation in Column 5 by using our presented analytic equations and the FEM simulation in Column 6 by using the COMSOL *Time Dependent*

Study at the harvester resonant frequencies. Moreover, *Un-OPTF*, *OPTF1*, and *OPTF2* were fabricated by using the micro-fabrication process above. *Com_OPTF* was not selected into our silicon-area-constrained chip fabrication due to its comparable V_{peak} performance but significantly inferior runtime efficiency with reference to *OPTF1*. The measurement results are also included in Table 7 (Column 7). The SEM images of the prototyped devices are illustrated in Fig. 26.

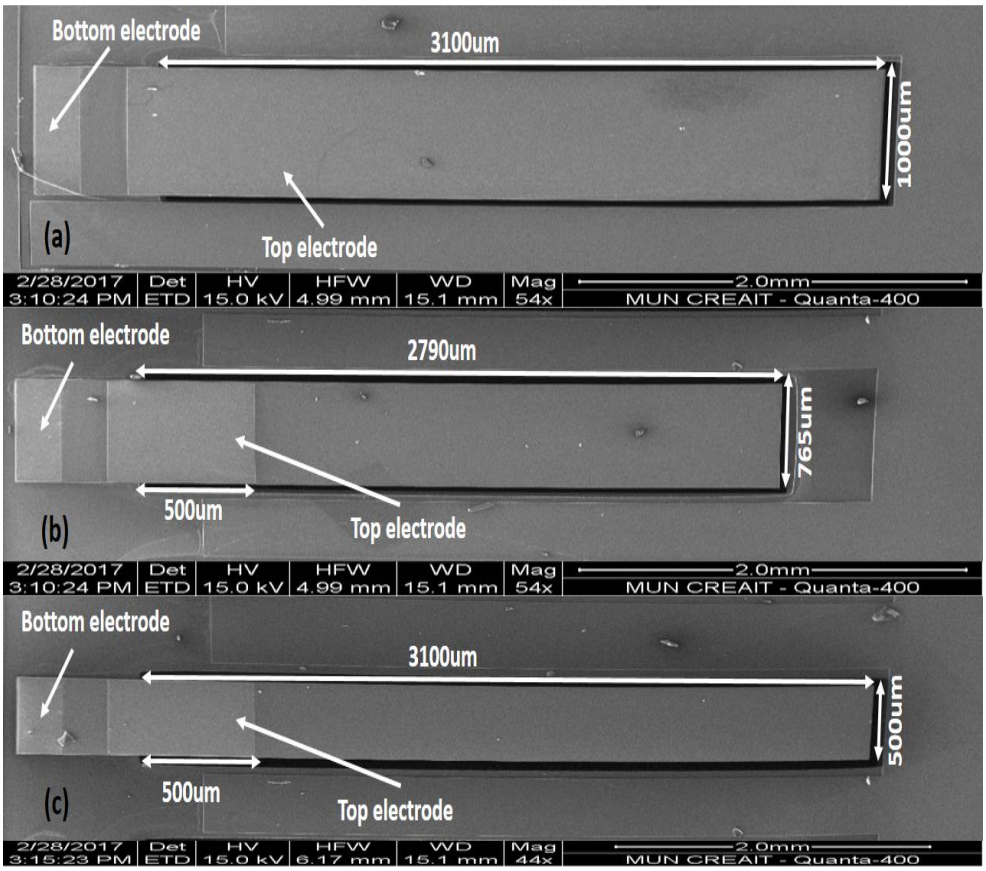

Fig. 26. SEM images of the fabricated micro-harvesters (a) un-optimized (*Un-OPTF*), (b) optimized with population size of 15 (*OPTF1*) and (c) optimized with population size of 30 (*OPTF2*).

Table 7. Un-Optimized and Optimized three physical aspects of the MEMS piezoelectric vibration energy harvesters by COMSOL optimization module and GA with different population sizes.

Parameter	**Beam Length l_b [μm]**	**Piezoelectric Length l_p [μm]**	**Beam Width w [μm]**	**V_{Peak} (Analytic) [mV]**	**V_{Peak} (FEM) [mV]**	**V_{Peak} (Measurement) [mV]**	**Resonant Frequency [Hz]**	**Population Size**	**Runtime [min]**
Range	[1000,3100]	[400,3100]	[400,1000]	-	-	-	-	-	-
Un-OPTF	3100	3100	1000	50	47	36	1595	-	-
Com-OPTF	2993	2507	650	54	50	-	1791	-	315
OPTF1	2790	500	765	52	49	41	1972	15	16.1
OPTF2	3100	500	500	72	67	50	1576	30	130

From the summarized data in Table 7, one can observe that number reduction of the optimizable parameters from 5 to 3 can considerably reduce the GA runtime. However, the efficiency improvement of the COMSOL optimization module is not significant. Although *Un_OPTF* was selected to use the maximum available physical dimensions, its performance on the harvested voltage magnitude is not necessarily superior. Moreover, in comparison with *Com_OPTF*, *OPTF1* can achieve equivalent harvested voltage magnitude but with much less runtime. Among all the candidates, *OPTF2* can achieve the largest harvested voltage magnitude with reasonable runtime.

In addition, compared to the measured output voltage, we can see that the analytic model presented in Section 3.2 is capable of estimating the harvested voltage magnitude with accuracy of around 80%. Our analyses show that such a difference between the analytic estimation and experimental measurement is mainly due to neglect of air damping ratio (normally 0.01 - 0.05 [140]) and absence of electrode thickness during the analytic computation. On the one side, if we consider an air damping ratio of 0.015 in the FEM simulation, the simulation results would be very

close to the measurement results. On the other side, the electrode thickness may take up to 10% of the beam thickness. Furthermore, it can be seen that our proposed GA optimization methodology with proper size of population is able to enhance the harvested voltage by a factor of 31% while reducing the harvester physical size by 50%. In contrast, the efficiency of the optimized harvester with COMSOL optimization module (i.e. *Com_OPTF*) is improved only by 6.4% while it needs a lot more time for completion of the optimization. Therefore, we conclude that our presented analytic model is very helpful for estimating harvested voltage of the MEMS unimorph piezoelectric energy harvesters and our proposed GA-based optimization methodology can facilitate the MEMS design both effectively and efficiently.

One may observe that the reported peak harvested voltage magnitudes for the studied harvesters in Table 6 are generally less than those listed in Table 7. This is all due to the differences of two applied technologies and excitation inputs. In Table 6 the beam and piezoelectric film use aluminum and PZT respectively, while in Table 7 the two materials are silicon and AIN. Moreover, we used 0.5g acceleration as the excitation input for the computation/simulation in Table 6, and 2g acceleration in the experiment of Table 7 for easier measurement data reading. Therefore, one can conclude that the performance of our proposed GA-based optimization methodology is independent of technology material properties and external excitation inputs.

As reflected in Table 7, geometry modification of energy harvesters may change the amount of the resonant frequency. In theory the resonant frequency of a mechanical resonator can be computed by (34):

$$\mathrm{f} = \frac{1}{2\pi}\sqrt{\frac{k}{m}} \quad , \tag{34}$$

where k is the stiffness and m is the mass of the harvester. That is to say, the resonant frequency is

largely dependent on the physical aspects of the harvester. Table 8 lists the computed mass for the presented energy harvesters (i.e., the un-optimized and optimized ones) in Table 7. There is certain mass change that can be observed from the various harvesters above. Among them, *Un_OPTF* is the heaviest while *OPTF2* is the lightest.

Table 8. Computed masses of the un-optimized and optimized piezoelectric energy harvesters.

Device Name	**Mass [ngr]**
Un_OPTF	85.84
Com_OPTF	52.47
OPTF1	51.38
OPTF2	37.2

In order to compute the required stiffness for resonant frequency calculation by using (34), Fig. 27 exhibits the tip displacement versus excitation force for the four presented harvesters from Table 8. To measure the tip displacement, we used COMSOL Multiphysics to model the harvesters in 3D space and applied variable forces by *edge load* at tip location in *Stationary Study* with *Parametric Sweep* function. The slope of each curve can clearly represent the stiffness of the corresponding energy harvester. One can observe that *Un_OPTF* has the maximum stiffness and *OPTF2* is the minimum one. Furthermore, even though the *Com_OPTF* and *OPTF1* devices have almost identical masses, the resonant frequency of *OPTF1* is 9.2% greater than that of *Com_OPTF* due to their clear difference in stiffness. Therefore, it can be concluded that the geometry optimization is of high significance for the unimorph piezoelectric energy harvesters due to the sensitivity of stiffness besides device mass.

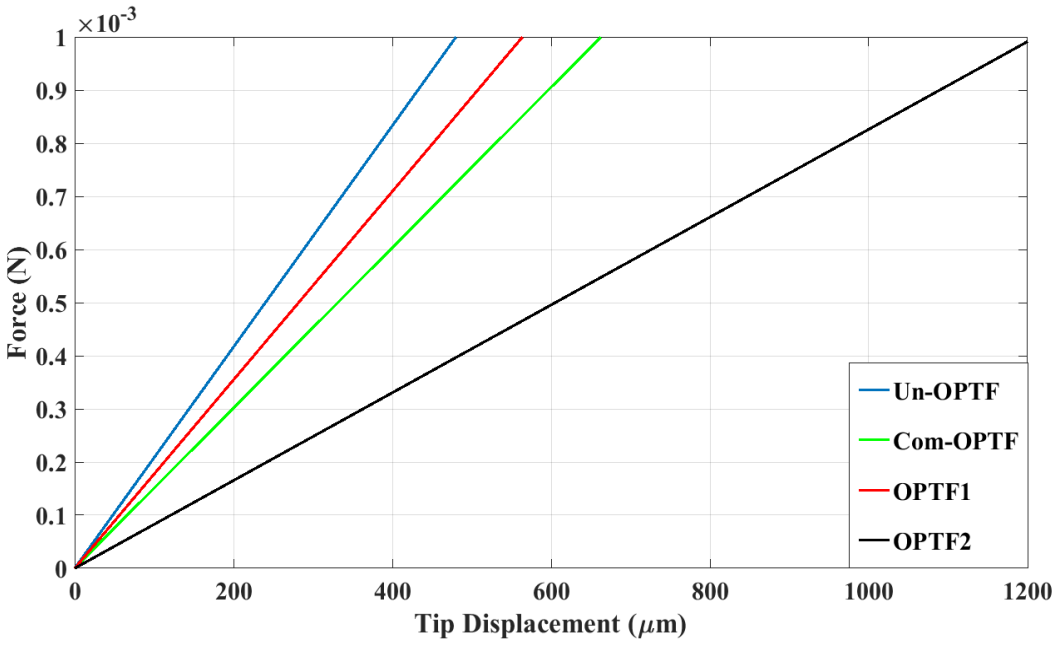

Fig. 27. Tip displacement versus excitation force for the un-optimized and optimized harvesters with consideration of three optimizable parameters.

Another vital parameter to be investigated for the performance of one piezoelectric energy harvester is its impedance. The internal piezoelectric impedance, which is known as a source impedance, can be modeled by VanDyke equivalent circuit [151]. According to this model, the internal piezoelectric generator impedance is dependent on several physical properties of the resonator, such as stiffness, mass, mechanical damping, and piezoelectric capacitance. Consequently the geometry optimization proposed in this chapter can be used to change the internal impedance of the piezoelectric harvesters. Fig. 28 illustrates the simulated internal impedance for the four energy harvesters as listed in Table 7, including the resistance curves (with the maximum amount at the resonant frequency) and the reactance curves (with zero magnitude at the resonant frequency). In this regard, 3D geometry of these devices was modeled by COMSOL Multiphysics and 0.01 was considered as a damping ratio around the device resonant frequency. Then 0.01 volt was applied on the top side of the piezoelectric film as a test voltage to measure the

impedance in *Frequency Domain Study*. Among the measured impedances, it is observed that the maximum impedance belongs to the energy harvester with the minimum resonant frequency and the minimum piezoelectric film area, which is *OPTF2*. In contrast, *Com_OPTF*, which has higher resonant frequency than *Un_OPTF*, features the minimum internal impedance.

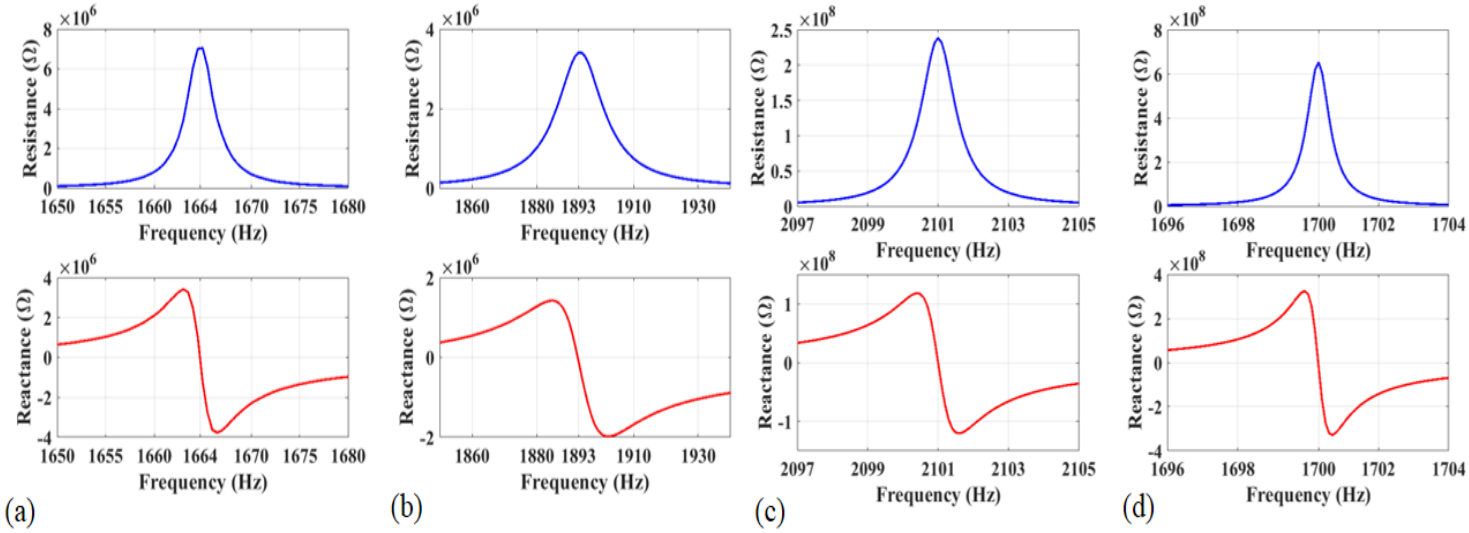

Fig. 28. Internal impedance of (a) *Un_OPTF*, (b) *Com_OPTF*, (c) *OPTF1* and (d) *OPTF2* piezoelectric MEMS harvesters.

Such intricacies can be understood by the following reasoning. Since any piezoelectric generator has an internal impedance, whose amount is a function of device resonant frequency and piezoelectric film area, the piezoelectric energy harvester with higher resonant frequency and larger piezoelectric film area would offer lower internal impedance. By providing an optimum impedance load corresponding to the piezoelectric internal impedance, a perfect impedance matching network would be offered so that the maximum harvested power can be extracted from the energy harvesters.

The von-Mises stress distributions for the four unimorph piezoelectric energy harvesters from Table 7 by applying a 0.01 N constant force at their tip edge under the *Load Edge* feature in

Stationary Study of COMSOL Multiphysics are shown in Fig. 29. According to this figure, the minimum observed actuation stress belongs to *Un_OPTF* with magnitude of $2.9*10^9$ N/m^2 (Fig. 29(a)), while the maximum one happens to *OPTF2* with magnitude of $6.9*10^9$ N/m^2 (Fig. 29(d)). That is to say, *Un_OPTF* and *OPTF2* gain the lowest and highest energy conversion efficiency in terms of the harvested voltage, respectively. Fig. 29(b) and (c) demonstrate that *Com_OPTF* and *OPTF1* have almost similar peak von-Mises stress with magnitude of $4.5*10^9$ N/m^2 and $4.43*10^{9,}$ N/m^2, respectively. As a result, it can be concluded that *OPTF2* has the best performance in terms of both actuating stress and occupied area in comparison with the other un-optimized and optimized MEMS piezoelectric harvesters.

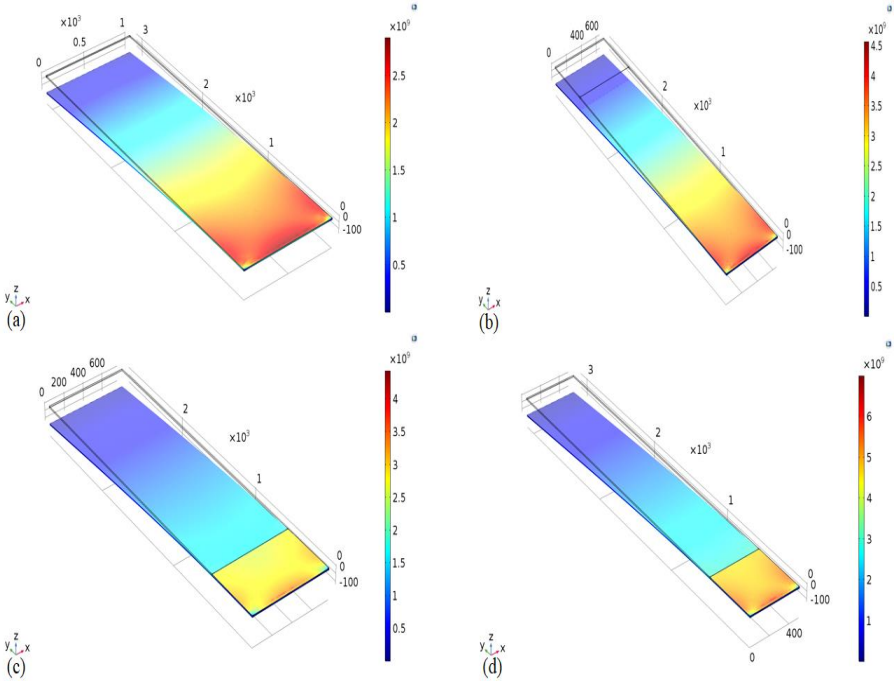

Fig. 29. 3-D views and von-Mises stress distributions of un-optimized and optimized piezoelectric MEMS harvesters: (a) *Un_OPTF*, (b) *Com_OPTF*, (c) *OPTF1* and (d) *OPTF2*.

To illustrate the direct effect of our proposed design automation methodology on performance enhancement, the induced charge density by the piezoelectric effect was computed and exhibited

in Fig. 30. By using COMSOL MEMS module, the induced charge density was measured by applying a 0.01 N force at the tip edge of each harvester. Figure 30 clearly demonstrates that the highest charge density with magnitude of 0.025 C/m^2 belongs to the GA-optimized harvester with sufficient population size (i.e., *OPTF2*). In contrast, the minimum charge density of 0.011 C/m^2 was observed for the un-optimized harvester, *Un-OPTF*. Moreover, the comparison of the induced charge density between the optimized harvester with COMSOL optimization module (i.e., *Com_OPTF*) and our GA-optimized harvester with population size of 15 (i.e., *OPTF1*) shows that they have very similar capability in producing charge with magnitude of 0.019 C/m^2 and 0.015 C/m^2, respectively. On the other side, one should not ignore the fact that *OPTF1* can run 19.7 times faster than *Com_OPTF*.

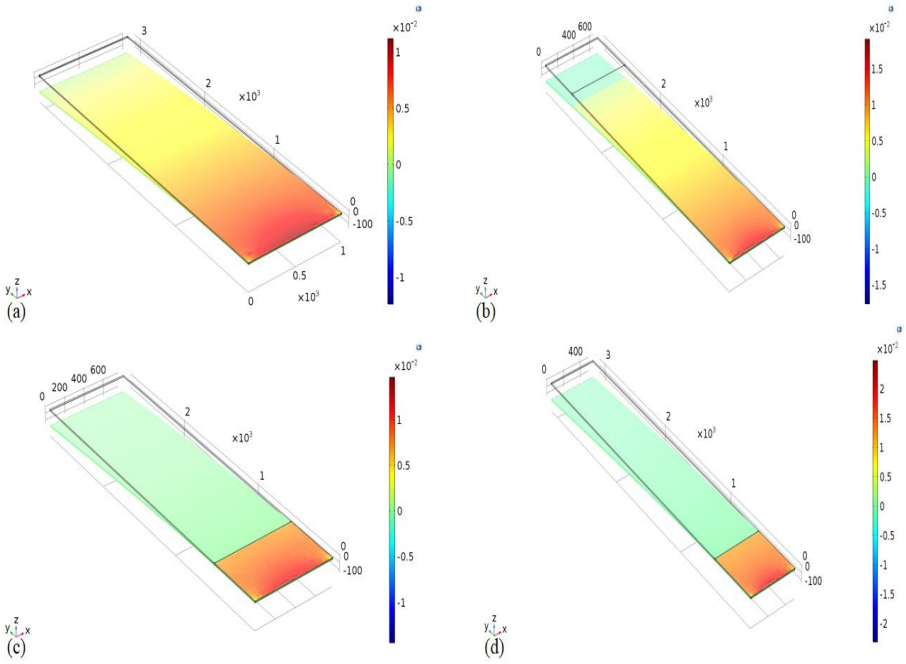

Fig. 30. 3-D views and induced charge densities of un-optimized and optimized piezoelectric MEMS harvesters: (a) *Un_OPTF*, (b) *Com_OPTF*, (c) *OPTF1* and (d) *OPTF2*.

A comprehensive comparison among the von-Mises stress, induced charge density, and measured peak harvested voltage shows that there is a direct relationship between actuating stress,

induced charge, and harvested voltage amount. This is also theoretically reflected from our presented equation set in Section 3.2. Thus, a unimorph piezoelectric energy harvesting device with the capability of forming higher stress would be able to generate larger harvested voltage. Our proposed GA-based optimization methodology can optimize the physical geometry of the unimorph piezoelectric energy harvesters in order to form higher stress and in turn generate higher output voltage.

3.5. Summary

In this chapter we proposed a GA-based design and optimization method for MEMS unimorph piezoelectric energy harvesters. The analytic equations for estimating the generated voltage from the MEMS unimorph piezoelectric harvesters were first presented and then validated by using COMSOL Multiphysics, a commercial FEM tool, as well as experimental measurement of our prototype devices. The proposed GA-based optimization methodology in this study demonstrated an enhancement of energy harvesting efficiency by 31% in comparison with un-optimized harvesters. This improvement was gained along with physical size reduction in several aspects such as beam width and piezoelectric film length. In addition, the comparison between the proposed optimization method in this chapter and available commercial product (e.g., COMSOL optimization module) shows that our GA-based optimizer has higher optimization efficiency in enlarging the harvested voltage magnitude and reducing the computation time. Moreover, some effects of the geometry optimization on harvester properties (such as resonant frequency, mass, stiffness, and internal impedance) were studied. The developed design and design automation techniques would be essential for the MEMS unimorph piezoelectric energy harvester designers to be liberated from the conventional laborious trial-and-error effort.

Chapter 4 Frequency Tuning and Efficiency Improvement of Piezoelectric MEMS Vibration Energy Harvesters

4.1. Introduction

During the past decade, several approaches to improve energy conversion efficiency of the piezoelectric energy harvesters have been presented. As a matter of fact, all these proposed methods to enhance energy conversion efficiency of the piezoelectric MEMS energy harvesters have been performed without considering operational resonant frequencies of the harvesters. For instance, although the proposed method in [128] enlarged the device efficiency, the harvester resonant frequency is also increased. However, this is actually undesirable for vibration energy harvesters due to the low frequency nature of the ambient vibration sources [152][153] and the narrow operational bandwidth of the energy harvesters [154]. One of the popular topological design methods for the MEMS-based piezoelectric harvesters is to locate a proof mass at the beam tip [155] because of its compatibility with the regular micro-fabrication processes. Although the resonant frequency tuning for this type of MEMS piezoelectric energy harvesters has been studied in the literature, how to simultaneously optimize both resonant frequency and harvested voltage amplitude is still unknown thus far.

Moreover, since the previously developed techniques for resonant frequency tuning and energy conversion efficiency improvement of the MEMS piezoelectric energy harvesters are heavily dependent on the designers' intellectual decision, sufficient design experience and considerable trial time are indispensable for the designers to gain optimal device structure. To

facilitate this design process, a number of optimization techniques, such as the variant-mesh analysis based on finite element method (FEM) [130], the correlation matrix with aid of FEM results by incrementing the harvester geometry aspects [131], etc., have been proposed. However, requiring a large amount of FEM simulation time and only considering one objective in the optimization make these methods less effective for real devices in the practical applications. In a recent study [156], Siramdas and Pratap demonstrated that the harvested power by the unimorph piezoelectric MEMS energy harvesters can be enlarged by optimizing four parameters, namely, excitation force, equivalent mass, harvester's natural frequency, and power factor, where the power factor itself is a function of coupling factor, frequency ratio, normalized load resistance, and damping ratio.

From this study, one can imply that the operational resonant frequency should be considered in the optimization for the energy conversion efficiency improvement of the piezoelectric MEMS energy harvesters due to its impact on the amount of the harvested voltage. However, nonlinearity and intricacy among the harvester physical dimension aspects, resonant frequency, and energy conversion efficiency make the conventional design methods less effective and efficient if solely relying on human observation in the optimization loop. In order to tackle this issue, we are motivated to develop an automated design and optimization technique based on Genetic Algorithm (GA), which is an evolutionary computation method for optimizing complex problems. Our proposed optimization methodology in this chapter can optimize physical aspects of the MEMS piezoelectric vibration energy harvesters with the minimum designers' efforts to achieve high energy conversion efficiency and low operational resonant frequencies, besides their geometric size reduction. The major work in this chapter has been formally documented in one journal paper (as listed in the Appendix [Journal-3]).

4.2. Analytic Modeling of Resonant Frequency of Piezoelectric MEMS Energy Harvesters

As shown in Fig. 31, the unimorph piezoelectric harvesters can be manufactured without or with a proof mass at the beam tip. The resonant frequency (or natural frequency) of a micro cantilever with clamped-free boundary conditions with no proof mass can be estimated by the bending modulus [157] or flexural rigidity [158]. In the flexural rigidity, the resonant frequency of both micro and macro cantilevers (or beams, both of which are exchangeable throughout this chapter) can be expressed by (35):

$$\mathrm{f_n} = \frac{1}{2\pi}\sqrt{\frac{\mathrm{k}}{\mathrm{m}}} \quad , \tag{35}$$

where *k* is the beam stiffness and *m* represents the effective mass of the beam. The stiffness of the rectangular objects can be simply calculated by (36):

$$\mathrm{k} = \frac{3\,\mathrm{Y_b I_b}}{l_\mathrm{b}^3} \quad , \tag{36}$$

where Y_b is the Young's modulus of the beam, I_b is the area moment of inertial, and l_b is the beam length. Since the highest quality factor of the clamped-free beams is obtainable at their first-mode resonant frequency, we can compute the first-mode resonant frequency of the harvesters by using (37) [159]:

$$\mathrm{f_1} = \frac{3.52}{2\pi}\sqrt{\frac{\mathrm{Y_b I_b}}{\mathrm{m_b} l_\mathrm{b}^3}} \quad , \tag{37}$$

where m_b is the beam mass. By equating (37) and (35), we can derive the equivalent mass, which considers both the beam mass m_b and the proof mass m_{tip} at the beam tip. Thus, (35) can be rewritten as:

$$f_1 = \frac{1}{2\pi}\sqrt{\frac{3Y_b I_b}{(0.2427m_b + m_{tip})l_b^3}}; \qquad (38)$$

where m_{tip} denotes the proof mass at the end of the beam (if existing). In such a presented analytic model for estimating the resonant frequency of the unimorph MEMS piezoelectric harvesters, it is assumed that the effect of the piezoelectric film and electrode layers on the resonant frequency is insignificant. Therefore, only the attributes of the beam and proof mass are taken into account in the computation below due to their remarkable sizes in comparison with the other components.

On the other side, the harvested voltage by the piezoelectric materials is proportional to the actuating stress on their surface. Thus, according to the IEEE standard on piezoelectricity, the conversion relationship between the generated voltage and stress can be expressed by the presented analytic equation (28) for the unimorph piezoelectric harvesters in Chapter 3.

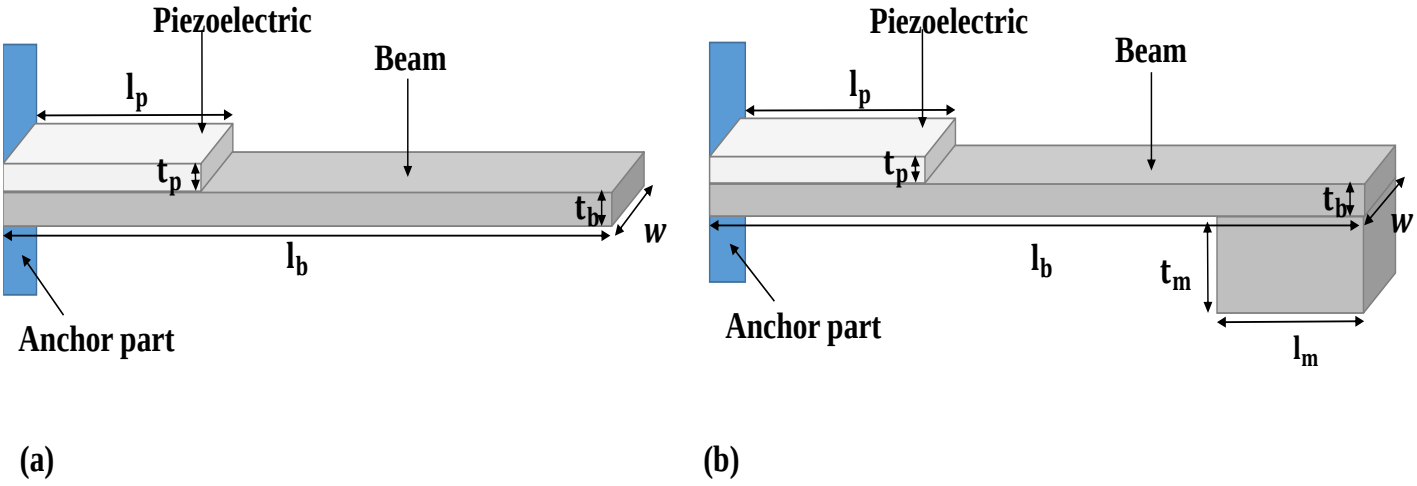

Fig. 31. Structural diagram of the unimorph MEMS piezoelectric energy harvesters (a) without and (b) with a proof mass.

4.3. Multi-Objective Optimization Based on Genetic Algorithm

Genetic algorithm (GA) is an evolutionary and heuristic computing method that is used for searching in a large solution space to optimize complex problems by mimicking biological evaluation. In the GA optimization method, a solution is represented as a chromosome within a population. The entire population, which is comprised of a large number of chromosomes, can be generated by distinct methods, such as random generation, greedy heuristic, etc. The GA scalability and performance are dependent on the population size, which is normally a user-defined parameter. The GA multi-objective working flowchart is depicted in Fig. 32 [147][148].

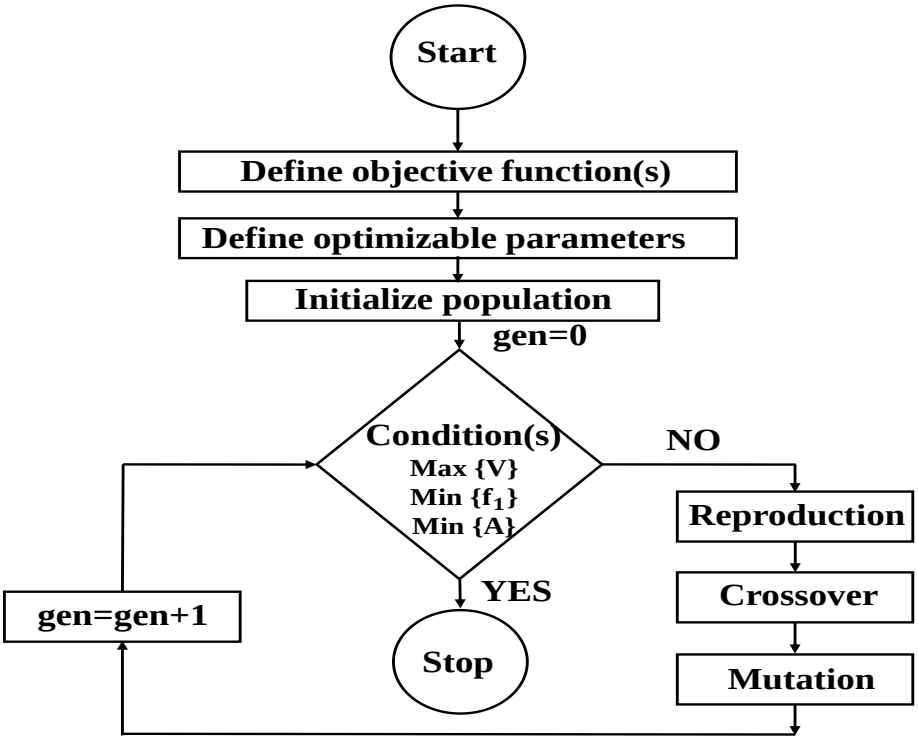

Fig. 32. Flowchart of the multi-objective GA working principle.

In this chapter, the GA methodology is utilized for both single-objective and multi-objective optimization. Therefore, as shown in Fig. 32, first of all the users need to define the objective function(s) and optimizable parameters. In this way, the presented equations (28) and (38) are deployed as the objective functions, while the physical aspects of the harvesters, i.e., beam length (l_b), piezoelectric-film length (l_p), proof mass length (l_m) (if existing), and beam or piezoelectric-film width (w) are considered as optimizable parameters.

After providing these information by the users, GA commences with initialization, where the variables (i.e., optimizable parameters) are coded in the form of fixed-length binary string. In this stage, the variables are selected randomly within the allowed ranges, while the selection probabilities are considered to be equal for all the qualified values. During the GA-based optimization, usually three genetic operators are performed on the entire population, where the repetition is controlled by the number of generation. The first genetic operator, which is called *reproduction*, is to strive to find appropriate strings in a population and interpolate them into a mating pool. In the literature, a number of methods for appropriate string selection have been proposed, although the basic ideas are similar. From the population, the strings with certain preferable features have to be selected. Afterwards, the selected individuals are reproduced and inserted into the mating pool.

The second genetic operator within GA is called *crossover*. This operator chooses two strings from the mating pool, whose particular portions are swapped. Consequently, such a recombination operation between the string pairs creates some new strings, which are called *offspring*. Eventually, the last genetic operator, which is called *mutation*, is performed to change only one bit from 1 to 0 or vice versa. This mutation operation, similar to the other two operators, is performed randomly with a very low probability, whose value is normally recognized as mutation rate. Once these three

operations are sequentially performed on all the population members, one GA generation, which is indicated by *gen* in Fig. 32, will be counted. Finally, if the specified conditions (i.e., sufficiently superior harvested voltage *V*, resonant frequency f_1, and occupied silicon area *A*) are satisfied, the algorithm will be stopped and the optimum values of the optimizable parameters will be reported.

It is worth mentioning that the MEMS-based energy harvesters might be optimized by using other mathematical optimization techniques, such as nonlinear programing, geometric programing, etc. However, these techniques may impose special requirements (e.g., continuity or convexity) on the problems themselves. Moreover, they tend to be highly dependent on the selection of a proper starting point in the optimization process. Therefore, in this study we opt for the GA in the multi-dimensional search, which is capable of statistically approaching the global optimum solutions by skipping local optima. Furthermore, the GA is able to tackle multi-objective optimization challenges by offering Pareto solutions for designers' synergistic trade-off decisions. It should be noted that each optimization technique has its own advantages as well as drawbacks. Although featuring the listed advantages above, the GA-based optimization is normally a time-consuming evolutionary process. And its algorithmic factors need to be well tuned in the implementation.

4.4. Experimental Results and Discussion

By integrating the presented analytic equations in Sections 3.2 and 4.2, it is feasible for the designers to estimate both the magnitude of the harvested voltage and the operational resonant frequency of the MEMS unimorph piezoelectric harvesters. Thus, as discussed in Section 4.3, the required objective fitness functions for the GA optimization methodology can be provided by using these analytic equations. It is obvious that the presented analytic equations are dependent on the

harvester's dimensions (e.g., width, length, thickness, etc.) and utilized material properties, such as Young's modulus. During the design process, the designers normally have good control on physical dimensions of the devices, whereas the thicknesses of various layers are constantly fixed in most of the commercially accessible MEMS fabrication technologies. In this regard, we have defined four physical variables as optimizable parameters, i.e., l_b, l_p, l_m, and w. Thus, the proposed optimization method by specifying the following objective fitness functions, was implemented in MATLAB genetic algorithm toolbox (Version 2014) in order to maximize the harvested voltage and minimize the resonant frequency of the MEMS piezoelectric harvesters besides their geometric size reduction.

$$\begin{aligned} &\text{Maximize: } \{V\} \\ &\text{Minimize: } \{f_1\} \\ &\text{Minimize: } \{A\} \\ &\text{Subject to: design rules of the optimizable parameters} \end{aligned} \tag{39}$$

where V represents the harvested voltage, f_1 denotes the first-mode resonant frequency, and A is the structural area of the harvester. For all the optimizable parameters (i.e., l_b, l_p, l_m, and w), the upper and lower bounds, as listed in the second row of Table 9, are defined by considering the following three factors: (1) design rule constraints (which are demanded by the foundry), (2) available silicon area, and (3) rational aspects for ease of measurement.

In order to study the accuracy of the proposed analytic modeling discussed in the previous section, and demonstrate the performance of the proposed optimization methodology in both voltage enhancement and resonant frequency reduction, four piezoelectric harvesters with and without integration of proof mass were prototyped by using the micro-fabrication process detailed in Section 3.4.1 of Chapter 3. Among these prototyped piezoelectric energy harvesters, two of

them, which are listed as *Un-OPT* and *Un-OPTM* in Table 9, were fabricated with no special considerations. Thus, they can be identified as the un-optimized cases for the piezoelectric MEMS harvesters without and with proof mass, respectively. In the first step, the GA was executed as a single-objective optimization of the voltage magnitude by setting the population size to 30 and the generation number to 20, which means its aim was to only enhance the energy conversion irrespective of the resonant frequency and required silicon area. Consequently, the piezoelectric MEMS structure in absence of the proof mass was optimized and its geometrical properties are summarized in Table 9 under the name of *OPT*. Furthermore, another GA run was performed as a multi-objective optimization with its population size of 50 and generation number of 20. Therefore, the physical aspects of the piezoelectric MEMS harvester with the integration of the proof mass was optimized by considering the enhancement of the energy conversion efficiency and the reduction of the resonant frequency, besides its geometric size reduction. This optimized harvester is identified as *OPTM* in Table 9.

Table 9. The physical dimensions of the un-optimized and optimized MEMS piezoelectric energy harvesters.

Item	**Beam Length (l_b) [μm]**	**Piezo. Length (l_p) [μm]**	**Width (w) [um]**	**Mass Length (l_m) [μm]**
Range	(500,3200)	(500,3200)	(200,1000)	(100,1000)
Un-OPT	3150	3153	989	-
Un-OPTM	3010	3010	989	200
OPT	3154	500	500	-
OPTM	2997	1997	1000	1000

From the summarized data in Table 9, it can be seen that increasing size of the proof mass or beam dimension is a solution to reducing the resonant frequency and increasing the harvested voltage amplitude. However, in the absence of the proof mass, as described by the analytic models in Section 3.2, the width of the beam has almost no contribution to the resonant frequency and harvested voltage. Thus, in the case of single-objective *OPT*, which was optimized to only enhance its harvested voltage, any value (e.g., 500 μm) between the upper and lower bounds might be selected as the final beam width. However, if any other objectives are simultaneously considered in the scenario of multi-objective optimization, a clearer mutual relationship would properly guide the optimizable parameters to converge to their optimum solutions. That helps partially demonstrate that the single-objective optimization is generally less superior than the multi-objective optimization.

It can be also seen that our GA-based optimization finally identified shorter piezoelectric film lengths in order to provide larger harvested voltage. This decision is actually in line with a most recent study about the impact of the piezoelectric/electrode length on the harvested voltage/power [160]. The rationale behind the increase of the harvested voltage is due to the relatively moderate diminution in the total generated electrical charge and the significant reduction in the piezoelectric film capacitance (i.e., $V=Q/C_p$). In addition, it should be noted that the performance of the optimized harvesters derived in Table 9 might have further increased, if different parameter upper and lower bounds were selected. For instance, *OPTM* would offer even larger harvested voltage as discussed in [128] if the upper bound of the proof mass length is chosen to be larger than 1000μm as defined in Table 9 of this study.

To investigate the accuracy and effectiveness of our proposed analytic models and GA-based optimization methodology, by using the micro-fabrication process as described in Section 3.4.1 of

Chapter 3, the un-optimized and optimized piezoelectric MEMS harvesters, according to their indicated geometric dimensions in Table 9, were fabricated for prototype measurements. The top and bottom view SEM images of the prototyped harvesters are depicted in Figs. 33 and 34, respectively.

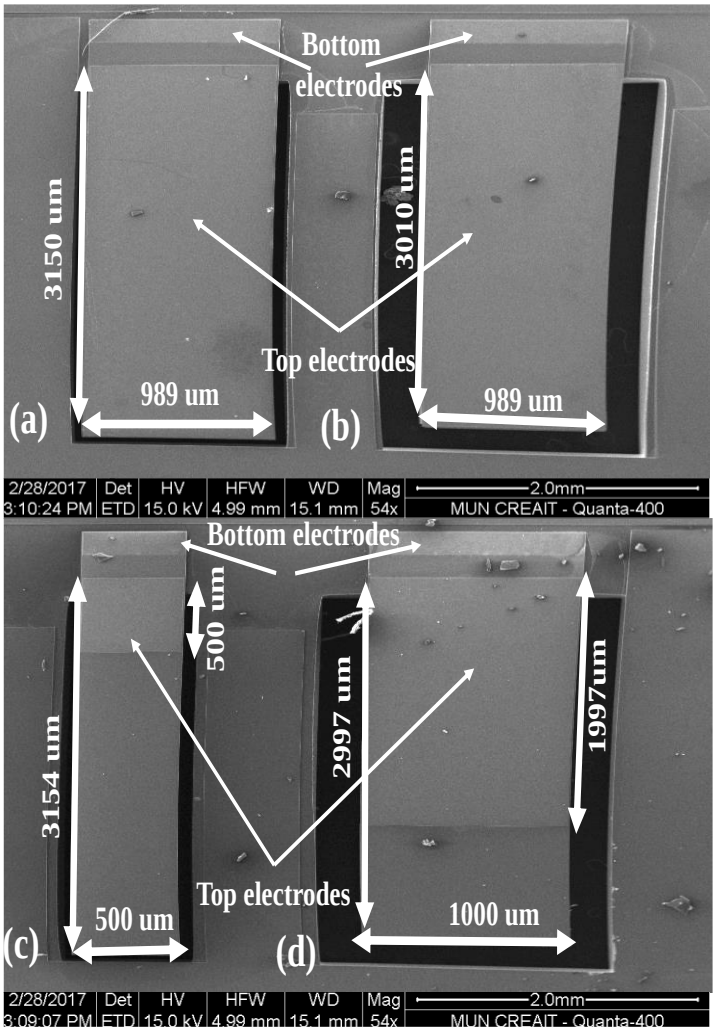

Fig. 33. Top view SEM images of the fabricated micro-harvesters (a) *Un-OPT*, (b) *Un-OPTM*, (c) *OPT*, and (d) *OPTM*.

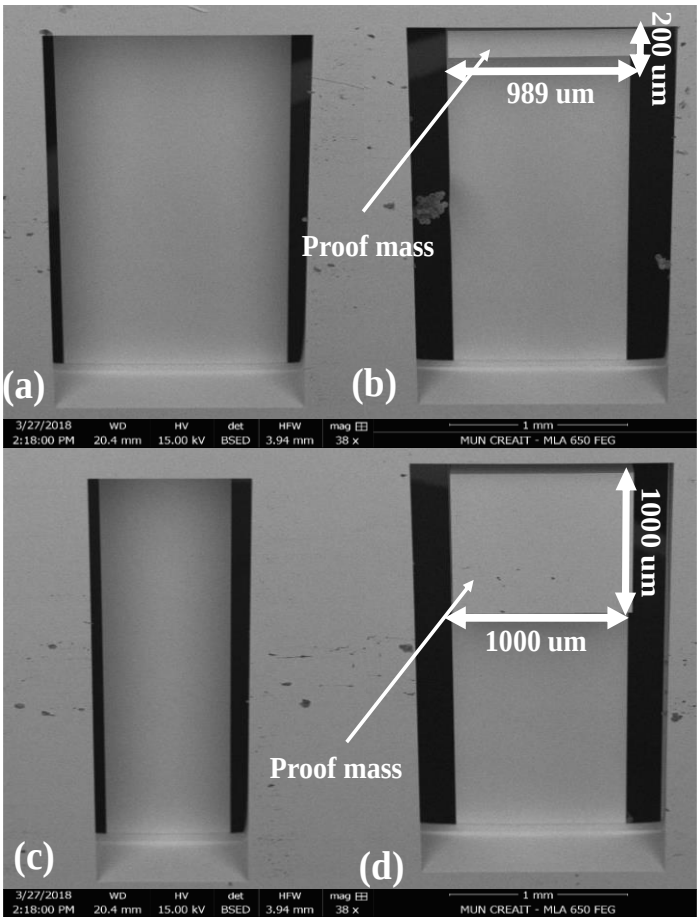

Fig. 34. Bottom view SEM images of the fabricated micro-harvesters (a) *Un-OPT*, (b) *Un-OPTM*, (c) *OPT*, and (d) *OPTM*.

To measure the harvested voltages and their resonant frequencies of the prototyped MEMS harvesters, the experimental setup as illustrated in Fig. 35 has been used. As shown in this figure, the prototyped harvesters can be excited by using a mechanical shaker (4809 manufactured by Brüel & Kjær), whose vibration frequency and magnitude are controlled by a function generator (3250 manufactured by Agilent) and a high power amplifier (manufactured by Brüel & Kjær). The shaker acceleration amplitude is monitored by an accelerometer (ADXL 335 manufactured by Analog Devices), which is attached to the shaker. The generated voltage by the piezoelectric MEMS harvesters is measured by a high performance oscilloscope (DSA 7040 manufactured by

Tektronix) through a high impedance probe. In order to measure the tip displacement for deriving the resonant frequency, we have used a laser displacement sensor (LK-H022 manufactured by Keyence), which is mounted on top of the prototyped harvesters.

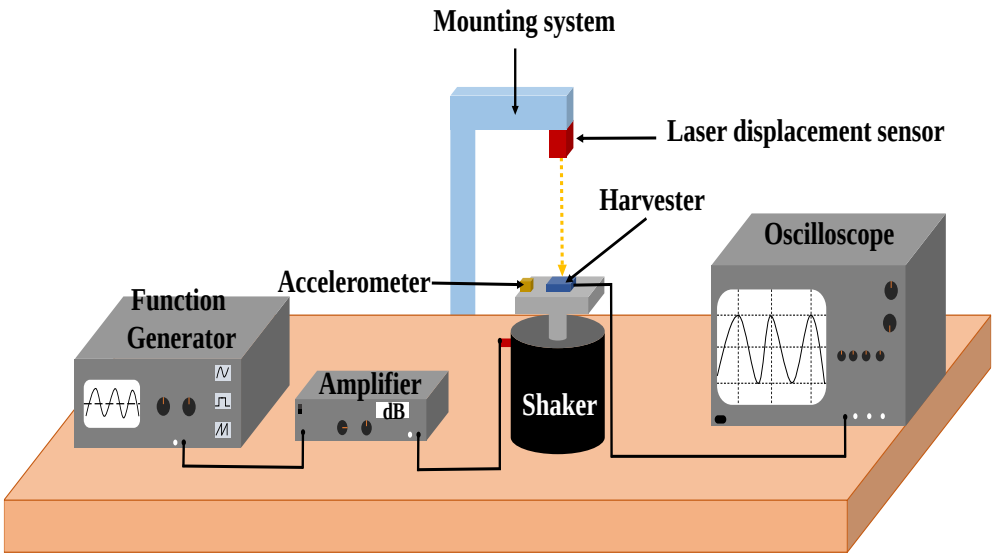

Fig. 35. Schematic of the utilized experimental setup for measurement of the harvested voltages and operational resonant frequencies.

To comprehensively evaluate the capability of the proposed optimization methodology, the numerical technique carried out by the available commercial FEM simulator (i.e., COMSOL Multiphysics (version 5.2a)) and the analytic technique by utilizing the presented analytic models in Sections 3.2 and 4.2, besides the experimental measurement, have been deployed to estimate the harvested voltage and resonant frequency for the given aspects of the MEMS harvesters. The observed results for all the prototyped harvesters based on three methods (i.e., analytic, numerical and experimental) for both resonant frequency and harvested peak voltage are listed in Table 10.

According to Table 10, one can observe that the utilized analytic equation for estimation of the resonant frequency is able to perform with less than 15% error in reference to the FEM

simulation results. The discrepancy was mainly caused by the neglect of two thin layers in the structure of the harvesters (i.e., piezoelectric material and electrode) in the analytic computation. It is obvious that taking into consideration these two layers, which have been modeled in the FEM method, can significantly increase the stiffness of the mechanical resonators, and in turn the resonant frequencies as reported by the FEM simulations.

Table 10. The physical dimensions of the un-optimized and optimized MEMS piezoelectric energy harvesters.

	Resonant Frequency [Hz]				**Harvested Peak Voltage [mV]**		
Parameters / Device	**Analytic**	**FEM**	**Experimental (with electrical connections)**	**Experimental (without electrical connections)**	**Analytic**	**FEM**	**Experimental**
Un_OPT	1341.5	1560	1770	1682	51	47	36
Un_OPTM	515.78	554.69	886	525	439	385	310
OPT	1306	1524	1704	1589	75	68	52
OPTM	269.83	320.1	425	298	2208	2050	1900

In order to provide electrical connections to the prototyped harvesters, in our experiments we manually connected wires to the top and bottom electrodes by utilizing conductive epoxy. Since this handling is not precise, it is highly possible that the active beam length was diminished to a certain extent. As a result, the measured resonant frequencies of the prototyped harvesters, where the electrical wires were connected to the electrodes, are normally higher than the FEM results by a factor of ~1.4.

Consequently, to investigate the impact of the electrical connections on the resonant frequency, the connected electrical wires on the surface of the top electrodes in different locations close to the

anchor side have been modeled in COMSOL Multiphysics. In this regard, an additional layer with the width of 400 μm and the uniform thickness of 200 μm, whose density is assumed to be uniform, was attached to the top electrode. In Fig. 36, it is demonstrated that for all the four prototyped energy harvesters, the amount of the resonant frequency is actually increased when the occupied area of the beam by the electrical wire is incremented. Moreover, it can be further observed that there is a good agreement between the FEM and experimental results when the occupied beam length by the electrical wire is within the range of 15% - 20% of the entire beam length.

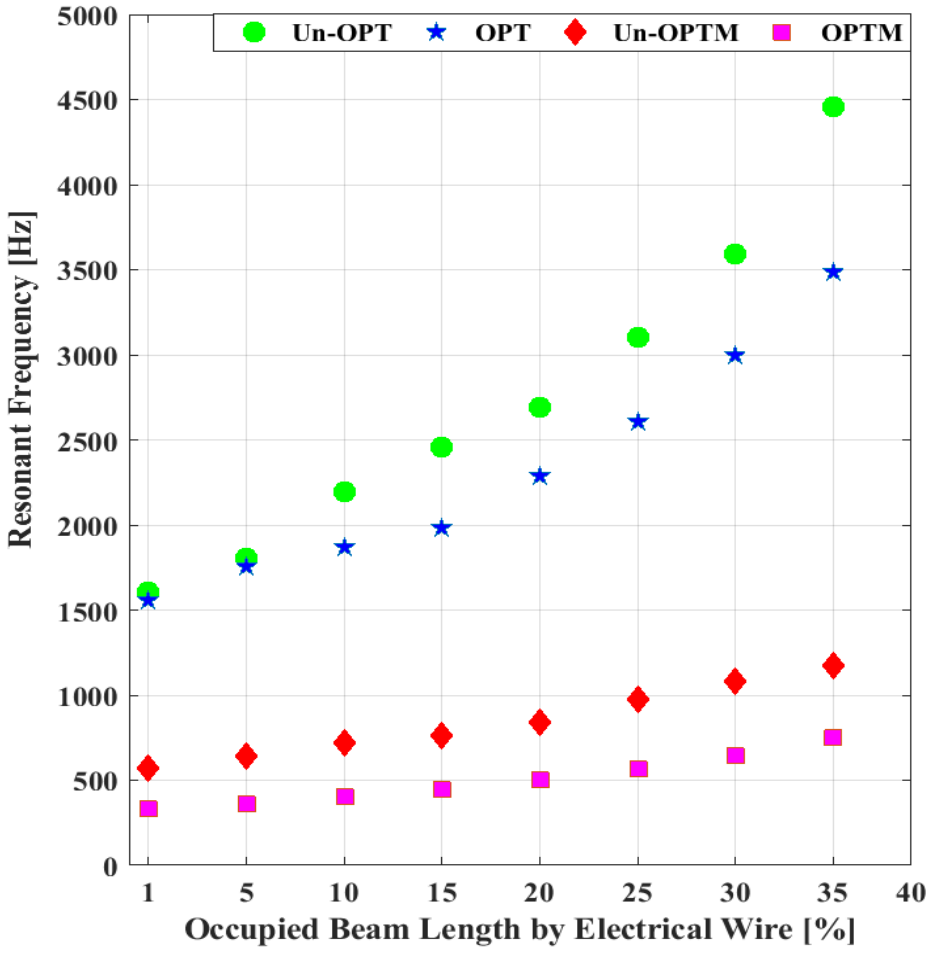

Fig. 36. Impact of the electrical wire size on the resonant frequency of the MEMS piezoelectric harvesters.

Furthermore, to experimentally investigate the effect of the electrical wires on the operational resonant frequency of the harvesters, the resonant frequency was also measured without electrical connections by using the displacement sensor. In this regard, the operational shaker frequency was swept and the tip displacement of the prototyped harvesters was measured. The maximum displacement, which was observed at the harvester resonant frequency, could represent the device resonant frequency. As per Table 10 and Fig. 36, it is obvious that the measured resonant frequency without electrical connections is in a good agreement with the FEM simulations. Thus, we can conclude that it is the imperfection of the electrical wire connection that reduces the effective length of the beam, which then increases the resonant frequency of each prototyped harvester. Moreover, it should be noted that this observed impact of the electrical connection on the resonant frequency of the MEMS harvesters can be readily eliminated by considering a contact pad on the silicon substrate and expanding the top electrode of the piezoelectric cantilever to that pad when designing the layout.

In Table 10, the comparison among the harvested peak voltage by using the presented analytic model, FEM simulations, and experimental measurement demonstrates that these obtained results are quite close to one another. Our analysis shows that around 20% difference between the analytic model and the measured peak voltage is due to the absence of the electrode layer in the analytic computation and the applied rough number for the air damping ratio, which is normally in the range of 0.01 - 0.05 [140]. Thus, we can confidently conclude that the presented analytic equations for estimation of resonant frequency and harvested voltage can be used as the objective fitness functions for the GA-based optimization methodology, which is supposed to indicate the optimization trend rather than providing exact values.

According to the experimental measurement of the resonant frequencies and harvested peak voltages for *Un_OPT* and *OPT* energy harvesters, it is clear that the proposed GA-based optimization as a single-objective optimization could reduce the resonant frequency from 1682 Hz to 1589 Hz and enhance the harvested voltage from 36 mV to 52 mV, which means this resonant frequency reduction just happened naturally under no algorithmic control. To enhance the functionality of the proposed optimization methodology, we need to execute a multi-objective optimization for the unimorph piezoelectric harvesters with an integration of proof mass. In this regard, the comparison of the measured resonant frequency and harvested peak voltage between *Un_OPTM* and *OPTM* harvesters shows that the GA was able to reduce the resonant frequency from 886 Hz to 425 Hz and enhance the harvested voltage from 310 mV to 1900 mV, respectively. Thus, it can be highlighted that the performance of the optimized harvesters is much better than that of the un-optimized ones. Moreover, within the optimized ones, the harvester with the integration of proof mass (i.e., *OPTM*) from the multi-objective optimization can offer a more efficient energy harvester with the capability of operation at lower resonant frequency.

To explore the effects of the proposed GA-based optimization on the improvement of the mechanical properties for the piezoelectric MEMS energy harvesters, all the prototyped harvesters were modeled in COMSOL Multiphysics and their deflection under uniform acceleration of 1g was measured. The mode shapes of the prototyped harvesters during their operation in the first mode are illustrated in Fig. 37. Since the prototyped harvesters are clamped-free based, the maximum deflection can be only observed at their tips, while in these harvesters the maximum actuating stress is obtained in the vicinity of the anchors. Furthermore, the effects of the tip deflection on the amount of the harvested voltage will be analyzed in more detail below.

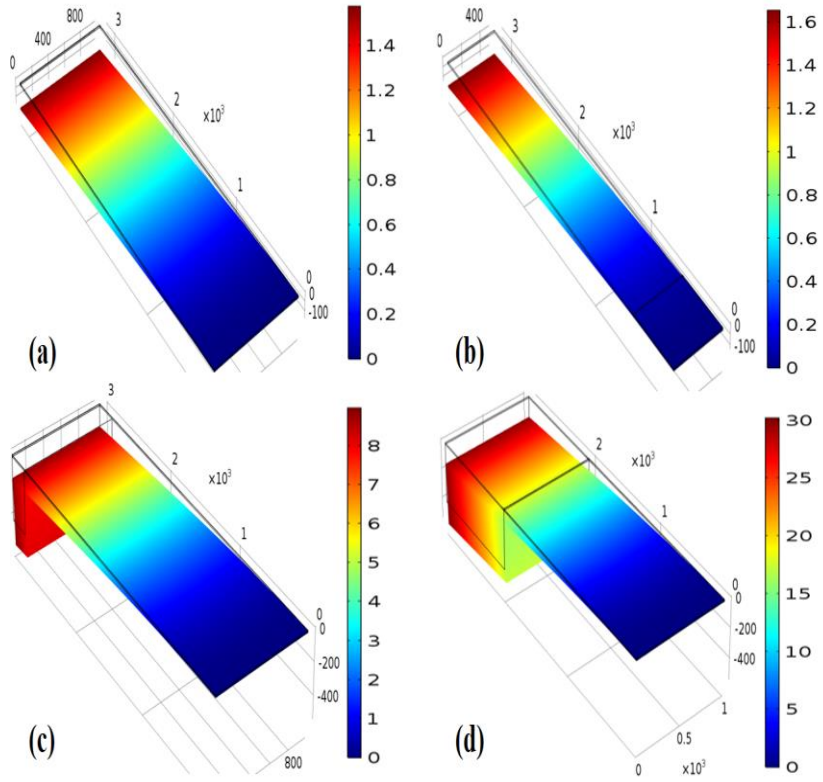

Fig. 37. Simulated 3-D beam deflections of (a) *Un_OPT*, (b) *OPT*, (c) *Un_OPTM* and (d) *OPTM* harvesters under uniform 1 g acceleration.

From the literature, we know that the harvested voltage by a piezoelectric energy harvester with clamped-free end boundary is proportional to their tip displacement as expressed below [113]:

$$V = \frac{3}{8}\left(\frac{t}{L}\right) h_{31}\delta_z \ , \qquad (40)$$

where t is the beam thickness, L is the beam length, h_{31} is the piezoelectric constant, and δ_z denotes the tip displacement along the Z-axis. The beam deflections along the Z-axis for all the prototyped harvesters, which were measured as per the FEM simulations, are illustrated in Fig. 38. One can observe that the proposed optimization methodology in this study is able to successfully enlarge the tip displacement especially in the scenario of proof-mass integration. Consequently, in the single-objective optimization (i.e., *OPT*) the tip displacement is clearly enhanced, although the

improvement of the harvested energy conversion is not that considerable. In contrast, with the aid of the multi-objective optimization (i.e., *OPTM*), the tip displacement is significantly enhanced and in turn the harvested voltage amplitude is extremely higher than the others. Thus, we can conclude that a bigger tip displacement is able to provide a larger amplitude of the harvested voltage, which can be actually achieved by our proposed GA-based optimization methodology.

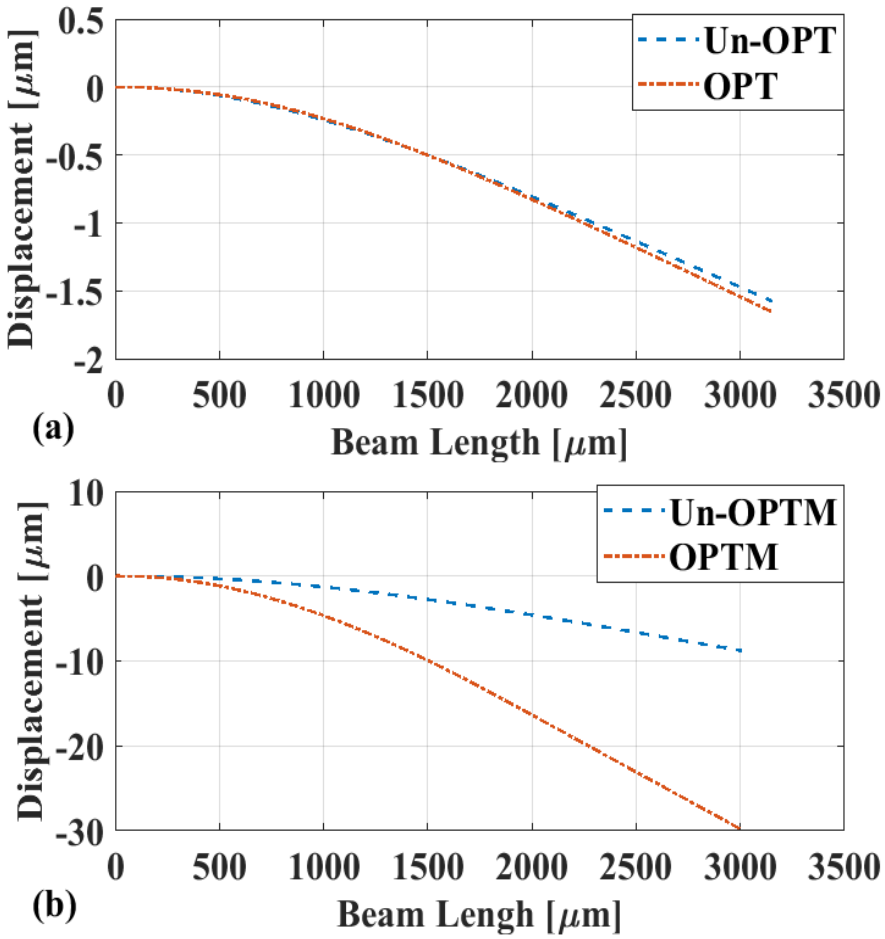

Fig. 38. Computed beam deflections by the FEM simulations along the Z-axis for the unimorph piezoelectric harvesters: (a) without and (b) with integration of the proof mass.

Finally, the results of our two optimized MEMS unimorph piezoelectric energy harvesters (i.e., *OPT* and *OPTM*) are compared with the other reported micro-piezoelectric harvesters in the

literature. A metric, which is widely used for harvester performance comparison, is called normalized power density (NPD). However, this metric is highly dependent on the load resistance and harvester volume. To eliminate such dependence on external components (e.g., load resistance) and minimize the effect on the material thickness, which is a constant value most of the time [161], we have proposed another metric called *Normalized Voltage Density* (NVD), which can be determined by the harvested voltage over the device occupied area times square of the acceleration amplitude. According to the listed data in Table 11, one can observe that the existence of proof mass provides higher NVD, and its optimum size plays an important role in offering higher energy conversion at a desirable (e.g., lower) resonant frequency. It is worth mentioning that the highest NVD belongs to the optimized harvesters by our proposed optimization methodology. Therefore, it is concluded that our proposed GA-based optimization methodology is able to explore the harvesters with higher NVD for both configurations of the unimorph MEMS piezoelectric harvesters (i.e., without and with proof mass), mechanical resonators, and in turn the resonant frequencies as reported by the FEM simulations.

Table 11. Comprehensive performance comparison among the reported harvesters from the literature and the proposed ones in this study.

Ref.	**Material**	**Length×Width (mm)**	**Proof mass Length (mm)**	**Acceleration (g)**	**Resonant Frequency (Hz)**	**Peak Voltage (mV)**	**NVD** $(\frac{\mathbf{mV}}{\mathbf{mm^2 g^2}})$
Jia (2016) [162]	AlN	2 × 0.5	No proof mass	2	3688	13.94	3.45
OPT	**AlN**	**3.154 × 0.5**	**No proof mass**	**2**	**1589**	**52***	**8.24**
Wen (2015) [54]	PZT	11 × 12.3	8	1	210	3500	25.86
Shen (2008) [155]	PZT	4.56 × 0.4	1.36	2	461.15	225	30.84
Andosca (2012) [163]	AlN	6 × 7.8	Not stated	1	57	2310	49.36
Janphuang (2014) [139]	PZT	11.5 × 10.8	5.75	1	96	6364*	51.23
OPTM	**AlN**	**2.9 × 1**	**1**	**2**	**425**	**1900***	**163.8**

*Open circuit voltage

4.5. Summary

In this chapter we proposed a design automation method for reducing resonant frequency and enhancing energy conversion of the piezoelectric MEMS energy harvesters. In this regard, the analytic model to estimate the resonant frequency and harvested voltage for the unimorph MEMS piezoelectric harvesters with and without integration of proof mass was presented. Its accuracy with reference to the FEM simulations and the experimental measurement from the prototyped harvesters was validated. Thanks to the high accuracy observed, they were utilized as the required objective fitness functions of our proposed GA-based optimization. The GA, which is an evolutionary computation method, was implemented to optimize the physical aspects of the harvester, such as beam length, beam/piezoelectric width, piezoelectric length, and proof mass length (if existing). By using a micro-fabrication process, two un-optimized harvesters without special considerations and two optimized ones based on the proposed optimization methodology were fabricated with their performance measured. It is demonstrated that the optimized harvester geometry by GA can generate the peak voltage of 1900 mV at the reduced resonant frequency of 425 Hz with the highest NVP of 163.8 among the alternatives, which is highly desirable for the MEMS devices.

Chapter 5 T-Shaped Piezoelectric Structure for High-Performance MEMS Vibration Energy Harvesting

5.1. Introduction

The most commonly used structure for piezoelectric MEMS vibration energy harvesters is the cantilever-based one, where the piezoelectric material is deposited on the unimorph or bimorph piezoelectric harvesters, respectively [164][165]. To effectively meet the power requirement of low-power consumer electronic applications such as wireless sensor nodes, wearable and implementable devices, various approaches for enhancing energy conversion efficiency have been proposed. For instance, Shen *et al.* [155] presented a clamped-free micro piezoelectric cantilever with an integrated silicon proof mass at the tip of the cantilever for reducing resonant frequency and enhancing power density. Later on, Jia and Seshia [128] observed that by increasing the size of proof mass the harvested power can be significantly enlarged. Instead of utilizing a rectangular or square shaped proof mass, Li *et al.* [166] proposed a curved L-shaped proof mass. Since this form of proof mass does not reduce the effective length of the piezoelectric cantilever, the prototype measurement in that study demonstrated its superiority over the conventional ones. Although the curved L-shaped proof mass may be considered as a new enhancement method for energy conversion efficiency, it cannot be readily applied to the MEMS-scale harvesters due to the manufacturing limitation of the micromachining process.

Another practical method to increase efficiency of the piezoelectric harvesters, which was presented by Gu [167], is to limit the cantilever up-and-down oscillations by using a pair of stoppers. The reported experimental results in this study clearly demonstrated that utilizing the stoppers can increase the output power by 5.3 times in comparison with the conventional

piezoelectric harvesters. Nevertheless, although the proposed device can be implemented by the regular MEMS technology, it is obvious that such an arrangement makes the fabrication process more complex and expensive.

Another appropriate configuration for piezoelectric MEMS vibration harvesters is to utilize a piezoelectric beam with clamped-clamped boundary conditions (i.e., both ends anchored). Thus, stress can be obtained from two distinct anchored areas. However, since this configuration would increase operational frequency, it is essential to utilize a significantly weighty proof mass in order to achieve an efficient energy harvester for being used in the real environment [168]. In turn, using a big proof mass would reduce the active area of the cantilever [169], which means the efficiency of this configuration is not considerably high at low resonant frequency. On the other hand, a lot of research efforts in the literature have been focused on packaging design to enhance the energy conversion efficiency for the piezoelectric MEMS harvesters, which themselves often just use the conventional straight clamped-free cantilever with integration of proof mass [170].

In this chapter, we are motivated to develop a new structure to enhance performance of the piezoelectric MEMS vibration harvesters in terms of both energy conversion efficiency and operational frequency. In this regard, with an intention of promoting uniform stress distribution along the piezoelectric cantilever and providing larger area for placing proof masses, a T-shaped cantilever structure with two degrees-of-freedom (DOF) is proposed. The tip part of the cantilever is comprised of a “T” segment, which is associated with two symmetric proof masses. Thanks to this special configuration, a considerable amount of stress/strain can be obtained from the tip part of the structure during the vibration, in addition to the anchor region. An analytic model for computing the frequency response of the proposed structure is derived, and the harvester performance is studied analytically, numerically and experimentally. By measuring the proposed

T-shaped piezoelectric MEMS harvester along with the conventional straight cantilever harvester, we have demonstrated that the normalized power density of the T-shaped harvester is about 4.8 times higher than that of the conventional one.

It cannot be ignored that the generated voltage by the piezoelectric MEMS harvesters is actually an AC signal, whose amplitude may be as low as several hundred millivolts due to the physical aspects of the MEMS harvesters. Therefore, AC to DC converters are deemed as an indispensable part of the MEMS energy harvesters. The typical diodes (e.g., silicon, Schottky and germanium) have voltage drops between 0.2 to 0.7 volts. Therefore, using this type of passive components in the conventional bridge rectifier would lead to extremely low-efficient converters, and consequently a considerable amount of the harvested voltage would be wasted.

In the literature, several approaches for rectification of small AC signals have been proposed. For instance, Tan *et al.* [121] proposed an active rectifier, which could rectify low input voltage (V_{in}=1.2V) with 70% efficiency. However, the proposed rectifier includes two operational amplifiers, which are powered by 3.3V external power supply. Thus, this requirement makes the proposed method less appealing for the practical energy harvesters. To eliminate such a bottleneck, Wahbah *et al.* [171] proposed a voltage doubler rectifier, which was able to rectify a minimum 1.8V AC signal with efficiency of 24%. Obviously this circuit is not suitable for our application since most of harvested voltage would be dissipated due to its low efficiency.

Furthermore, Schlichting *et al.* [172] proposed a mechanical AC to DC converter, whose low-loss hybrid rectifier consisted of four reed switches, on or off according to the strength of magnetic field. In this way, a permanent magnet was attached to the piezoelectric cantilever tip to provide magnetic field, while the periodic movement of the cantilever changed the magnetic field strength around each reed switch. Their experiments showed that this proposed mechanical rectifier was

able to offer extremely high efficiency, although the input harvested voltage had to exceed 3V. Besides that, the required permanent magnet may enlarge the size of the devices such that the MEMS harvesters can hardly benefit from this proposed method. In a recent study of [173], the efficiency of the rectifier interface circuits for piezoelectric MEMS harvesters has been largely improved (up to 80%) with the aid of a pre-charged battery. Nevertheless, such efficiency is only obtainable if the amplitude of the harvested voltage is at least 2V, whereas the reported efficiency is almost zero for the millivolt-level input.

It is worth mentiong that, during the past decade, several commercial power management products have been introduced to the market [126]. However, the accepted minimum input voltage is typically relatively high (around 2V), which can be rarely provided by the general piezoelectric MEMS vibration energy harvesters. Hence, in this chapter we are also motivated to propose a new circuit structure as a self-supplied power management system. It consists of a MOSFET-based rectifier and a DC-DC booster controlled by a microcontroller. All the utilized components are powered by the rectified DC voltage. This self-powered feature makes our proposed power management system highly suitable for the piezoelectric MEMS vibration energy harvesters.

The contributions from this chapter are highlighted below:

- We propose a new T-shaped piezoelectric harvester with higher power density at lower resonant frequency in comparison with the conventional piezoelectric harvesters;
- The proposed T-shaped micro cantilever is mathematically modeled for analytically expressing its frequency response;
- By using micro-fabrication process, we have prototyped the device and demonstrated its manufacturability as well as high performance;

- We introduce a self-supplied power management system, which can generally operate with small harvested AC voltages.

The major work in this chapter has been formally documented in one journal manuscript, two conference papers, and one under-review patent application (as listed in the Appendix [Journal-5][Conferenc-3][Conferenc-4][Patent-2]).

5.2. Analytic Modeling of T-Shaped Piezoelectric Structure

3-D structural diagram of the proposed T-shaped piezoelectric MEMS vibration energy harvester is depicted in Fig. 39. As shown in this figure, the harvester is comprised of two segments, i.e., body and tip parts. In the body part, similar to the conventional straight-cantilever piezoelectric harvesters, one side of the beam (or called cantilever, both of which are exchangeable throughout this chapter) is anchored. However, the other side, which is called the tip part in this chapter, can freely oscillate. It is expanded by integrating another cantilever, while two proof masses are placed at both ends of this second cantilever. Consequently, this structure can be viewed as a unimorph T-shaped piezoelectric cantilever for MEMS vibration energy harvesters. Such a structure provides the capability of oscillating in the bending and torsional modes, due to its two DOF. In the following, an analytic model for estimating bending and torsional mode frequencies of the T-shaped structure will be discussed.

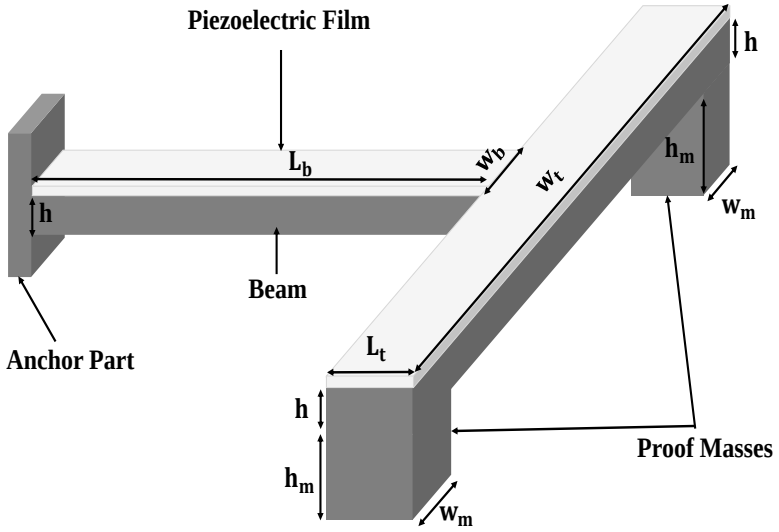

Fig. 39. Structure diagram of the T-shaped unimorph piezoelectric cantilever.

5.2.1. Resonant Frequency of Bending Mode

The resonant frequency of the bending mode shape for the T-shaped structure as illustrated in Fig. 40 (a) can be calculated by (41) [174]:

$$f_B = \frac{1}{2\pi}\sqrt{\frac{K_B}{m_{eff}}}, \tag{41}$$

where m_{eff} is the effective mass of the cantilever and $K_B$is the bending stiffness. The bending deflection of the conventional cantilever is related to radius of curvature, which is expressed by [143]:

$$\frac{1}{\rho} = \frac{d^2z}{dx^2} = \frac{-F}{YI}(x - L), \tag{42}$$

where ρ is the radius of curvature, z is the deflection along the Z-axis, F is the external excitation force, Y is the Young's modulus of the beam, I is the moment of inertia, x denotes the actuating force point on the X-axis, and L is the total length of the beam.

As demonstrated in Fig. 39, our proposed T-shaped cantilever comprises two segments: the first segment can be considered between $0 \leq x \leq L_b$ named as the body part, while the second segment is between $L_b < x \leq (L_b + L_t)$ named as the tip part. Thus, (42) can be rewritten as (43) for the T-shaped structure:

$$\frac{d^2z}{dx^2} = \begin{cases} \frac{d^2z_b}{dx^2} = \frac{-F}{YI_b}(x - (L_b + L_t)) & \text{If } x \leq L_b \\ \frac{d^2z_t}{dx^2} = \frac{-F}{YI_t}(x - (L_b + L_t)) & \text{If } x \geq L_b, \end{cases} \tag{43}$$

where L_b is the length of the body segment and L_t is the length of the tip segments. I_b and I_t are the moments of inertia of the body and tip segments, respectively, which can be computed by:

$$\begin{aligned} I_b &= \frac{w_b h^3}{12}, \\ I_t &= \frac{w_t h^3}{12} + 2\left[\frac{w_m h_m^3}{12} + \left[h_m w_m \times \left(\frac{h_m}{2} + \frac{h}{2}\right)^2\right]\right], \end{aligned} \tag{44}$$

where w_b, w_t and w_m are the widths of the body segment, tip segment and proof masses, respectively. And h and h_m denote the thicknesses of the cantilever and proof masses, respectively. The double integral of (43) gives the deflection along the Z-axis as follows:

$$z_{(x)} = \begin{cases} z_b = \frac{-F}{YI_b}\left(\frac{x^3}{6} - (L_b + L_t)\frac{x^2}{2} + Ax + B\right) & \text{If } x \leq L_b \\ z_t = \frac{-F}{YI_b}\left(\frac{x^3}{6} - (L_b + L_t)\frac{x^2}{2} + Cx + D\right) & \text{If } x \geq L_b, \end{cases} \tag{45}$$

where *A*, *B*, *C* and *D* are the integral constants, whose values can be calculated with respect to the clamped-free beam boundary conditions, thus:

$$\begin{aligned} &A = B = 0, \\ &C = -\frac{L_b\,(L_b + 2\,L_t)}{2\,h^3 w_b}.(h^3\,w_t - h^3 w_b + 8\,h_m^3 w_m + 12\,h\,h_m^2 w_m \\ &\qquad + 6\,h^2\,h_m w_m), \\ &D = \frac{L_b^2\,(L_b + 3\,L_t)}{6\,h^3\,w_b}.(h^3 w_t - h^3 w_b + 8\,h_m^{3s} w_m + 12\,h\,h_m^2 w_m \\ &\qquad + 6\,h^2\,h_m\,w_m). \end{aligned} \tag{46}$$

By substituting Equations (44) and (46) into (45), the deflection of the T-shaped cantilever along the Z-axis at the farthest point away from the anchor (i.e., $x=L_b + L_t$) can be expressed by:

$$\begin{aligned} z_{(x=L_b+L_t)} = {} & F \\ & \times \left(\frac{(L_b + L_t)^3}{3} - \frac{L_b^2 (L_b + 3L_t) \cdot \beta}{6\,h^3 w_b} \right. \\ & \left. + \frac{L_b (L_b + 2L_t)(L_b + L_t) \cdot \beta}{2\,h^3 w_b} \right) \times \left(Y \left(\frac{h^3 w_t}{12} + \frac{h_m^3\,w_m}{6} \right. \right. \\ & \left. \left. + 2\,h_m\,w_m \left[\frac{h}{2} + \frac{h_m}{2} \right]^2 \right) \right)^{-1}, \\ \beta = {} & h^3\,w_t - h^3 w_b + 8\,h_m^3 w_m + 12\,h\,h_m^2 w_m + 6\,h^2\,h_m w_m. \end{aligned} \tag{47}$$

In order to find the stiffness of the T-shaped cantilever, the general equation for stiffness, $K_B = F / z_{(x=L_b+L_t)}$, can be used. Therefore, the bending stiffness of the T-shaped cantilever is equal to:

$$K_B = Y\left(\frac{h^3 w_t}{12} + \frac{h_m^3\, w_m}{6} + 2\, h_m\, w_m \left[\frac{h}{2} + \frac{h_m}{2}\right]^2\right) \times \left(\frac{(L_b + L_t)^3}{3} - \frac{L_b^2(L_b + 3L_t).\beta}{6\, h^3 w_b} + \frac{L_b(L_b + 2L_t)(L_b + L_t).\beta}{2\, h^3 w_b}\right)^{-1}. \quad (48)$$

Since significant masses exist at the tip part, the effective mass can be estimated by [159]:

$$m_{eff} = \frac{33}{140} m_b + m_t. \quad (49)$$

where m_b and m_t denote the masses of the body and tip segments, respectively. Consequently, by applying (48) and (49) into (41), the resonant frequency of our proposed T-shaped structure in the bending mode can be obtained.

5.2.2. Resonant Frequency of Torsional Mode

The torsional mode shape of the T-shaped structure is depicted in Fig. 40 (b), and its amount can be computed by (50) [174]:

$$f_T = \frac{1}{2\pi}\sqrt{\frac{K_T}{I_P}}, \quad (50)$$

where K_T is the torsional stiffness of the cantilever, and I_P is the polar mass moment of inertia for the cantilever. As per the theory of torsion, the torsional stiffness is related to the angle of twist ($\emptyset$), which is given by (51) for the single rectangular cross-section cantilever:

$$\emptyset = \frac{T.L}{G.J}, \quad (51)$$

where T is the excitation torque, G is the shear modulus of the cantilever, L is the length of the cantilever, and J represents the torsional constant of the rectangular cross-section. With an assumption of constant torque through both body and tip segments, the total angle of twist for our proposed T-shaped structure can be estimated by (52),

$$\emptyset_T = \frac{T}{G}\left(\frac{L_b}{J_b} + \frac{L_t}{J_t}\right), \tag{52}$$

where J_b and J_t are the torsional constants of the body and tip segments, respectively, which are given by:

$$\begin{aligned} J_b &= C_b w_b h^3, \\ J_t &= C_t\, w_t h^3, \\ C_b &= \frac{1}{3}\left(1 - 0.63\frac{h}{w_b}\right), \\ C_t &= \frac{1}{3}\left(1 - 0.63\frac{h}{w_t}\right). \end{aligned} \tag{53}$$

Thus, based on the general definition of the stiffness, the required torsional stiffness for (50) can be expressed by (54):

$$K_T = G\,\frac{J_b\, J_t}{L_b J_t + L_t J_b}, \tag{54}$$

Eventually by considering both body and tip segments, the total polar mass moment of inertia for the T-shaped structure, which is computed by (55), can be also used in (50):

$$I_p = \frac{M_b}{12}\left(L_b^2 + w_b^2\right) + \frac{M_t}{12}\left(L_t^2 + w_t^2\right). \tag{55}$$

In the following sections, we will show that the presented analytic models above can accurately estimate the resonant frequencies of the bending and torsional mode shapes for the micro T-shaped structure.

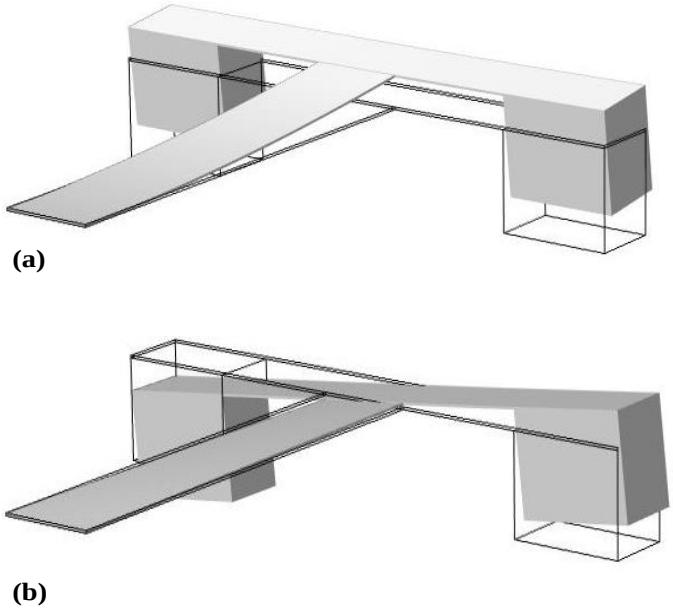

Fig. 40. Mode shapes of the T-shaped structure: (a) bending mode and (b) torsional mode.

5.3. Self-Supplied Power Management System

The structure of our proposed self-supplied power management system (SPMS) is illustrated in Fig. 41. It is comprised of four major functional blocks: rectifier, DC-DC converter, load limiter, and logic controller. In the following we will describe the construction of each functional block in detail.

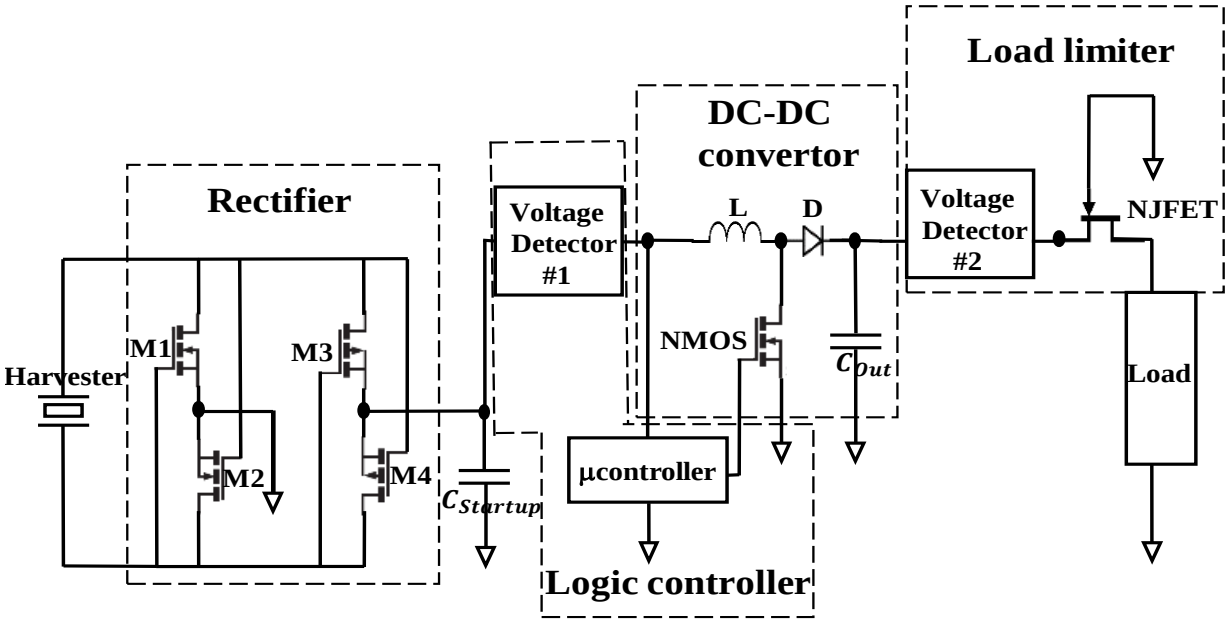

Fig. 41. Schematic of the proposed SPMS.

5.3.1. Rectifier

Since actuating stress on the piezoelectric vibration energy harvesters alternatively occurs, the generated voltage is an AC signal, which is infeasible to be directly stored. In order to convert the harvested AC voltage to a DC one, a MOSFET full-wave bridge rectifier is utilized as depicted within the leftmost dash-box of Fig. 41. In this way, two pairs of N-channel and P-channel MOSFETs in the fully cross-coupled structure is employed. In the positive cycle of the harvested voltage, the first pair of transistors (e.g., *M1* and *M4*) turns on and the second pair (e.g., *M2* and *M3*) gets off. Similarly, in the negative cycle the second pair turns on and the first pair gets off. Finally, the rectified voltage is able to be stored in a super capacitor (i.e., $C_{startup}$).

5.3.2. DC-DC Converter

The amplitude of the harvested voltage from the piezoelectric MEMS harvesters is normally very limited (e.g., several hundred millivolts). To increase the level of the harvested voltage to a

usable amount, a boosting converter, which is known as a DC-DC converter, has to be used. Our utilized DC-DC converter, as shown in the middle dash-box of Fig. 41, consists of one energy storage element at the input (i.e., inductor) and another one at the output (i.e., capacitor). In addition, an N-channel MOSFET operating as a switch, whose operational frequency is proportional to the generated clock signal by the microcontroller, is used to periodically deliver the stored energy from the inductor towards the output capacitor.

5.3.3. Load Limiter

To keep the output voltage at a certain level, we need to employ a sub-circuit for output voltage level control. In this regard, a feedback loop circuit would unnecessarily increase the power consumption of the SPMS. Instead we have utilized a voltage detector (i.e., #2) with the detecting voltage of 3.3V plus an N-channel JFET with the threshold voltage of 3.4V at the load side. Thus, once the boosted voltage of the output capacitor (i.e., C_{out}) reaches its specified level (i.e., 3.3V), the load part will be enabled. However, if the boosted voltage exceeds the JFET threshold voltage (i.e., 3.4V), the transistor will turn off. In other words, the level of the output voltage can be easily limited to the threshold voltage level of the JFET.

5.3.4. Logic Controller

Since the amount of the generated voltage by the piezoelectric vibration energy harvesters is a function of time, it is demanded to boost the stored voltage when its level reaches a sufficient amount. In this regard, the activity of the DC-DC converter and load limiter is controlled by using a voltage detector (i.e., #1). We have utilized a voltage detector with the detecting voltage of 1.5V to monitor the level of the stored voltage in the input super capacitor (i.e., $C_{startup}$). The functionality of the voltage detector is to make its output equal to its input whenever its input is

no less than the pre-defined detecting voltage. Thus, once the level of the accumulated voltage reaches this pre-defined detecting value (i.e., 1.5V), the voltage detector enables the microcontroller and the rest of the system. The microcontroller, which generates the constant clock signal for switching the DC-DC converter through the N-channel MOSFET, is powered by the rectified and stored voltage in the super capacitor $C_{startup}$. In the following section, the performance of our proposed SPMS will be demonstrated numerically and experimentally.

5.4. Experimental Results and Discussion

To experimentally validate the accuracy of the presented analytic models in Section 5.2, our proposed T-shaped piezoelectric structure, whose physical aspects are listed in Table 12, was fabricated by using the commercial PiezoMUMPs [175] micro-machining process. Its Scanning Electron Microscope (SEM) images are displayed in Fig. 42. In addition, to numerically investigate the frequency response of our proposed T-shaped piezoelectric structure, COMSOL Multiphysics software package was used for Finite Element Modeling (FEM) simulations. In this regard, a T-shaped piezoelectric structure, with the same dimensions as the fabricated one, was modeled in the 3-D space with isotropic materials for Eigenfrequency Analysis. Consequently, the frequency response of the T-shaped structure in the bending and torsional mode shapes was analytically, numerically, and experimentally obtained with their values as listed in Table 13.

Table 12. Physical aspects of the T-shaped piezoelectric structure for studying its performance analytically, numerically and experimentally.

Parameter	Description	Value
L_b	Length of the beam for the body segment	2100 μm
L_t	Length of the beam for the tip segment	500 μm
w_b	Width of the beam for the body segment	500 μm
w_t	Width of the beam for the tip segment	3100 μm
w_m	Width of the proof masses	780 μm
h	Thickness of the beam	10 μm
h_m	Thickness of the proof masses	400 μm
Y	Young's modulus of the beam	170 GPa

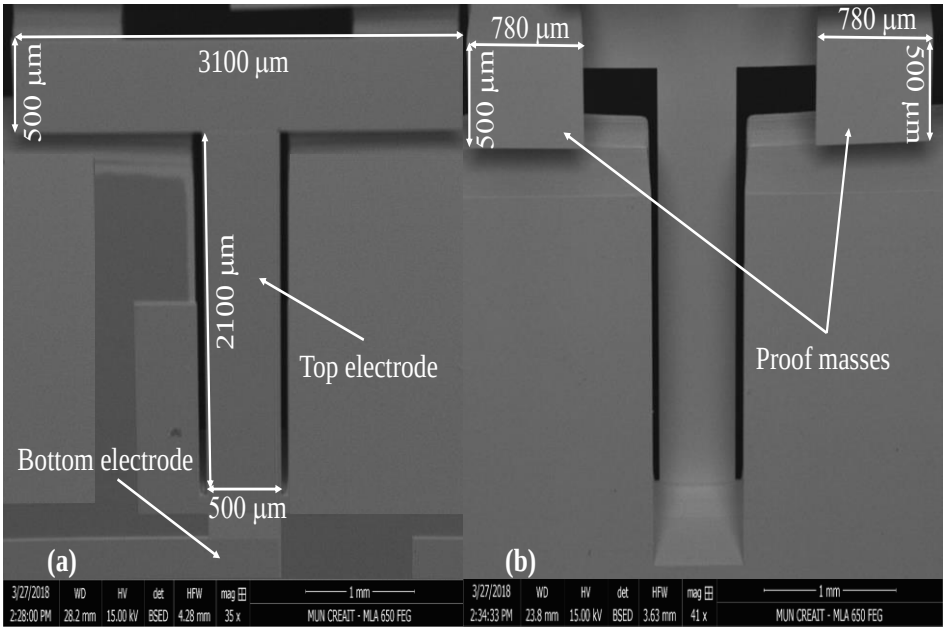

Fig. 42. SEM images of the fabricated micro T-shaped piezoelectric cantilever for prototype measurement, (a) top view and (b) bottom view.

Table 13. Estimated frequencies of the T-shaped piezoelectric structure by using analytical, numerical, and experimental techniques.

Technique / **Frequency**	**Analytical**	**Numerical**	**Experimental**
Bending mode	277	271.8	269.1
Torsional mode	415	401	371

As reflected in Table 13, our presented analytic models are able to estimate the resonant frequencies of the T-shaped piezoelectric structure in the bending and torsional modes with the accuracy of above 90%, with reference to the numerical and experimental techniques. Thus, the observed small discrepancy among the analytical, numerical, and experimental results accredits the capability of our presented analytic models for estimating the frequency response of the T-shaped piezoelectric structure.

In our experiments, the prototyped harvester was testified in the air medium, whose density may shift the resonant frequencies of the T-shaped structure. As reflected in Table 13, the measured frequency amounts of both bending and torsional modes are less than their estimated values by the analytical and experimental techniques. This is because the device is assumed to operate in the vacuum medium in our analytical and numerical techniques, which actually fully neglects the impact from air density. It is worth mentioning that the resonant frequencies of the micro-cantilevers are highly sensitive to the operational environment especially at their higher modes [176]. Consequently, larger frequency shift in our T-shaped piezoelectric structure, due to air density, can be observed for the higher mode resonant frequencies (e.g., torsional mode).

One can further conclude that our proposed T-shaped structure has two DOF, through which the bending and torsional modes can be observed relatively in the vicinity frequencies of each other. The frequency spectra of the T-shaped MEMS piezoelectric structure, which were acquired by the numerical FEM simulation and the experimental prototype measurement, are illustrated Fig. 43.

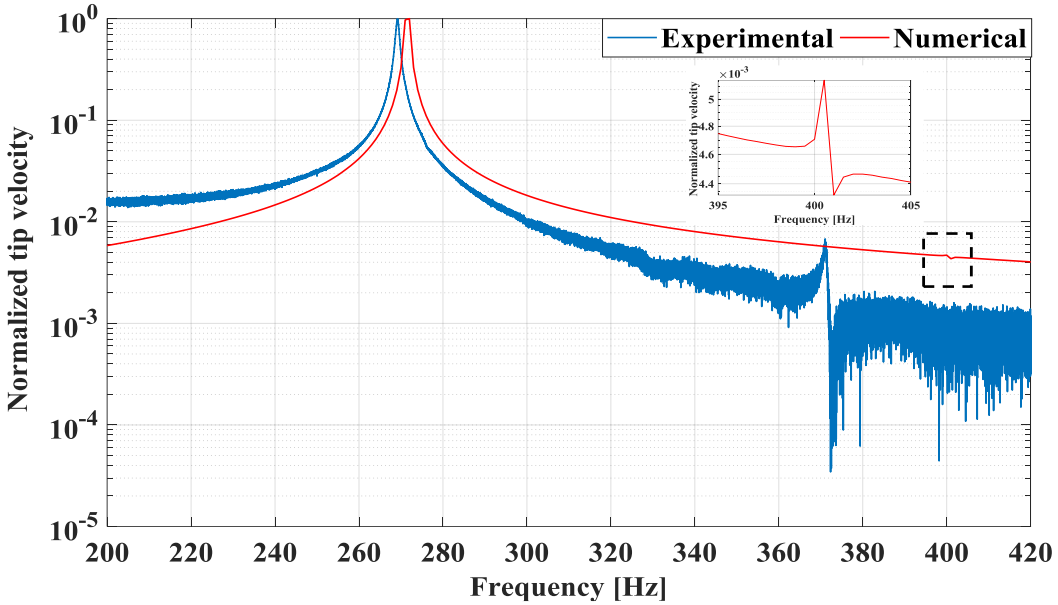

Fig. 43. Numerical and experimental frequency spectra of the T-shaped piezoelectric MEMS harvester.

The amplitude of the device deflection in the torsional mode is much less than its counterpart in the bending mode. As shown in Fig. 43, a large amount of oscillation amplitude along the Z-axis for the T-shaped piezoelectric structure is attainable when the harvester operates in its bending mode. On the other hand, since the electrodes in our energy harvester are arranged in the Z-axis capacitor style, the energy harvesting is mainly functional in the 3-1 mode. Consequently, harnessing a considerably large amount of energy is expected to take place during the device oscillation in its bending mode. In the following the performance of our proposed T-shaped structure in the bending mode will be studied in more detail.

The stress distribution across the T-shaped piezoelectric structure, which operates in the bending mode, is graphically demonstrated in Fig. 44 (a). For the comparison purpose, the stress distribution for a straight cantilever with a proof mass placed at the end but lacking the T-segment is computed and depicted in Fig. 44 (b).

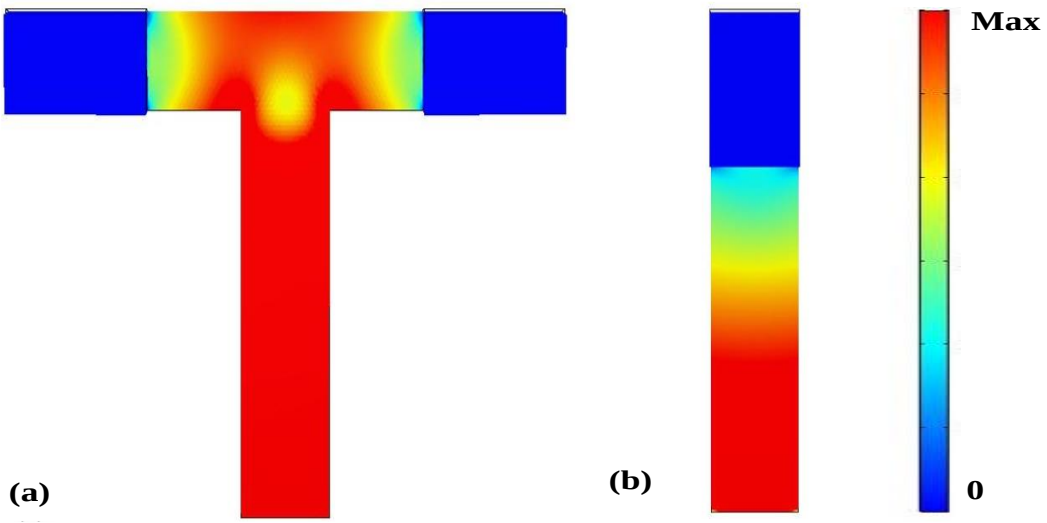

Fig. 44. Von Mises stress distribution on the cantilever surface when the device oscillates in the bending mode for (a) our proposed T-shaped structure and (b) the conventional straight cantilever.

According to Fig. 44, uniform stress distribution across the cantilever can be achieved if the tip region is expanded by the T-segment. Furthermore, it can be seen that the stress at the tip region in the conventional straight cantilever is almost zero. In contrast, in the T-shaped structure a considerably large amount of stress can be also observed at the tip region besides the anchor region. It is worth noting that, since the proof masses of our proposed T-shaped structure are located at the T-segment, the effective length of the cantilever in the body segment would not be reduced even though the size of the proof masses is increased. That is to say, a larger size of the proof masses in our proposed T-shaped structure is clearly feasible. This feature would make our proposed device capable of oscillating at lower resonant frequencies with higher bending amplitude in comparison with the conventional straight cantilevers.

To demonstrate superiority of the T-shaped piezoelectric structure in absorbing strain, volumetric strain along the piezoelectric film for the T-shaped structure and conventional straight cantilever estimated by FEM simulations is presented in Fig. 45. The maximum strain concentrations for the T-shaped and conventional straight cantilevers are all attributed to the regions very close to the anchor locations with the magnitude of 4.4×10^{-4} and 1.14×10^{-4}, respectively. The strain at the furthest point away from the anchor location, which is known as the tip region, is close to zero for the conventional straight cantilever, whereas this amount is quite high for the T-shaped structure. Therefore, it can be concluded that the active beam area (i.e., the area having the capability of harnessing strain/stress) of the T-shaped piezoelectric structure is much larger than that of the convention straight cantilever. Furthermore, since the sign of strain along the beam length remains constant, a single electrode is good enough for harnessing the energy from the surface of the piezoelectric material besides the other ground electrode. This would definitely reduce the complexity of the associated electrode routing and power management system.

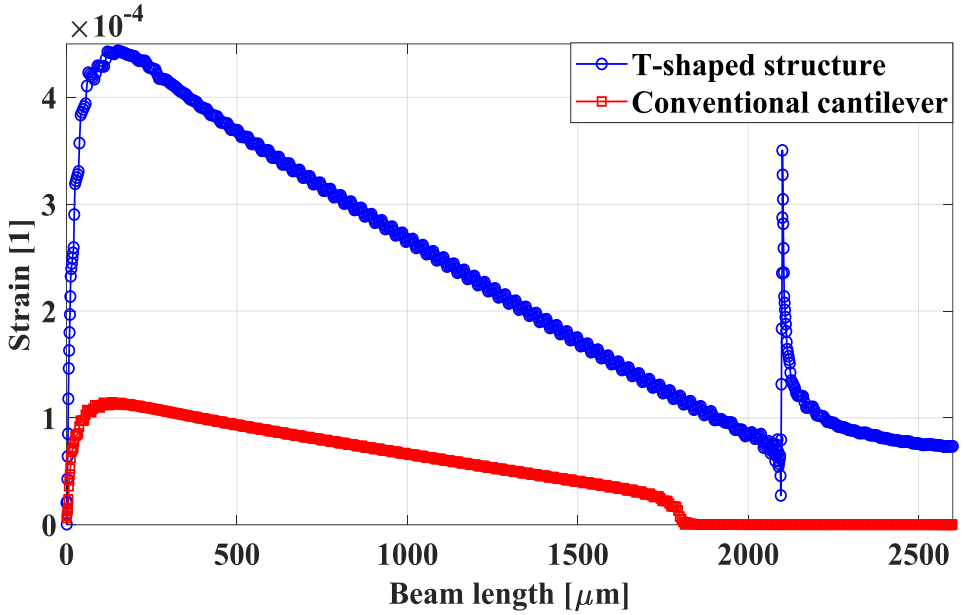

Fig. 45. Absorbed mechanical strain along the harvester beam length for the T-shaped structure and conventional straight piezoelectric cantilever.

According to the IEEE standard on piezoelectricity, if the electrodes are arranged in the capacitor configuration, the harvested open-circuit voltage by the piezoelectric material, which is proportional to the applied strain, can be expressed by [138]:

$$V_{o.c} = g_{31} t_p Y_p \varepsilon_p, \tag{56}$$

where g_{31} is the piezoelectric constant, t_p is the piezoelectric film thickness, Y_p is the piezoelectric material Young's modulus, and ε_p denotes the absorbed mechanical stain by the piezoelectric film. By integrating the strain distribution along the beam length (i.e., $\varepsilon_p = \int_0^{L_b+L_t} \varepsilon_p(x)dx$), the amplitude of strain can be obtained. In this regard, the mechanical strains as per Fig. 45 are 0.1256 and 0.0256 for the T-shaped and conventional straight cantilevers, respectively. Obviously, the capability of absorbing strain in the conventional straight-cantilever piezoelectric MEMS vibration energy harvester can be increased by a factor of 4.9 if the tip region is expanded by our proposed T-segment structure.

To demonstrate the direct effect of the absorbed mechanical strain on the amount of the harvested voltage, Fig. 46 illustrates the generated voltage by the T-shaped structure and the conventional straight cantilever. It can be seen that the amplitude of the generated voltage by the T-shaped piezoelectric structure is 2.33V, while the amount is only 0.49V for the conventional one. That is to say, the harvested voltage of the T-shaped piezoelectric harvester is larger than that of the conventional one by 4.75 times. This comparison clearly confirms the direct relationship between the harvested voltage and absorbed mechanical strain. Moreover, the T-shaped structure has a much lower resonant frequency in comparison with the conventional straight cantilever. Thus, we can conclude that the T-segment structure has a considerable contribution to the efficiency enhancement and resonant frequency reduction of the piezoelectric MEMS energy harvesters.

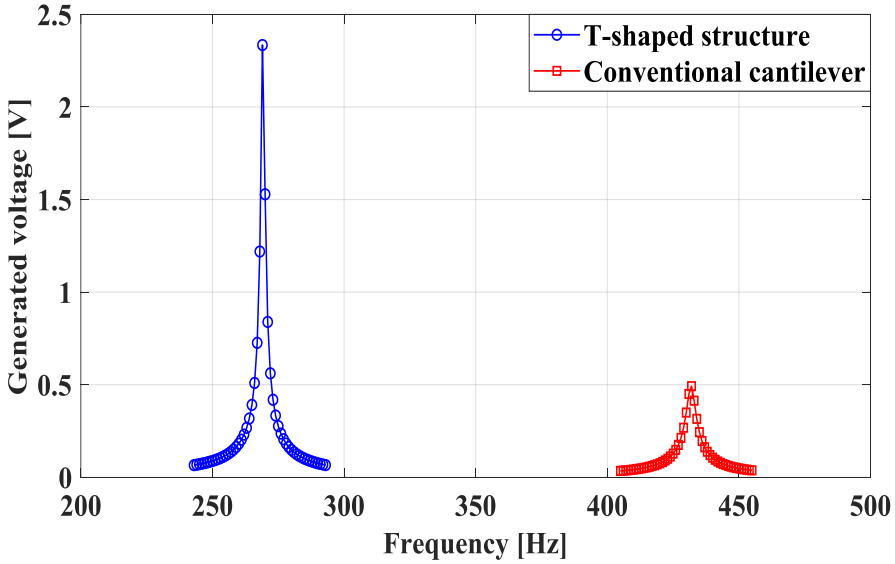

Fig. 46. Simulated generated voltage by the T-shaped structure and conventional straight cantilever, when they are excited by sinusoidal acceleration with the amplitude of 0.5g at their resonant frequencies.

To experimentally verify the performance of our T-shaped piezoelectric structure in terms of both energy conversion efficiency and operational frequency, we compare it with an optimized conventional straight-cantilever piezoelectric MEMS harvester. The associated information regarding the utilized optimization methodology for performance enhancement of this fabricated comparison harvester can be found in Chapter 4 [177]. The SEM images of such a conventional

straight-cantilever piezoelectric MEMS harvester with its optimized aspects are presented in Fig. 47. Its capability of harnessing energy was testified and compared with that of the prototyped T-shaped structure as illustrated in Fig. 42.

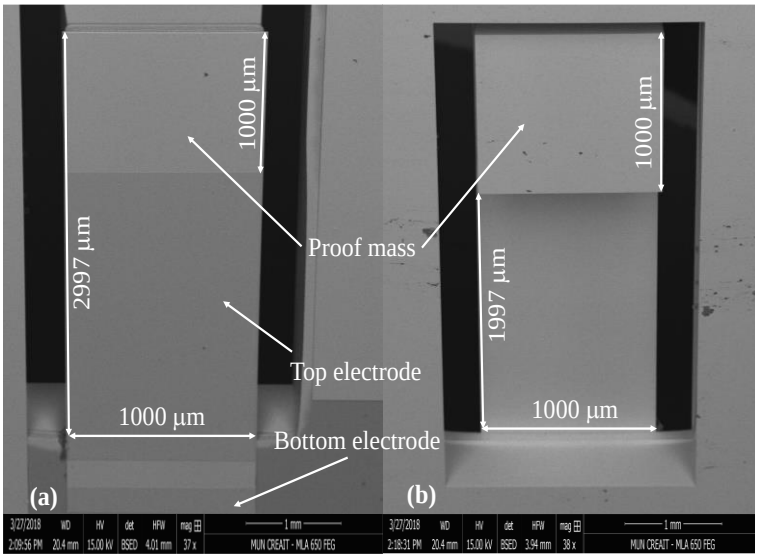

Fig. 47. SEM images of the fabricated conventional straight-cantilever harvester for prototype measurement: (a) top and (b) bottom views, respectively.

At first, the generated open-circuit voltages by both harvesters (i.e., the T-shaped and conventional ones) were measured. Both harvesters were excited by a mechanical shaker at their first mode-shape resonant frequencies (i.e., 269.1 Hz and 425 Hz for the T-shaped and conventional harvesters, respectively). The generated voltage by both piezoelectric MEMS harvesters were measured through high impedance probes of an oscilloscope. Fig. 48 (a) illustrates the harvested open-circuit voltages by the T-shaped and conventional piezoelectric harvesters as a function of acceleration. As expected from our prior numerical study, the amplitude of the harvested voltage by the proposed T-shaped harvester is significantly higher than that of the conventional harvester with straight-cantilever plus proof mass by over 2 times. More important, this feature is not dependent on the amplitude of the acceleration input. It is also obtainable for a large amplitude of acceleration (e.g., 10 m/s^2).

Fig. 48 (b) shows the harvested power by the prototyped T-shaped and conventional

piezoelectric harvesters. The measurement was conducted under optimal load resistances, which were 549 KΩ and 464 KΩ for the T-shaped and conventional piezoelectric harvesters, respectively. Similar to the harvested open-circuit voltages, the proposed T-shaped piezoelectric harvester is capable of generating larger power than the conventional one. The level of the harvested power is proportional to the acceleration amplitude.

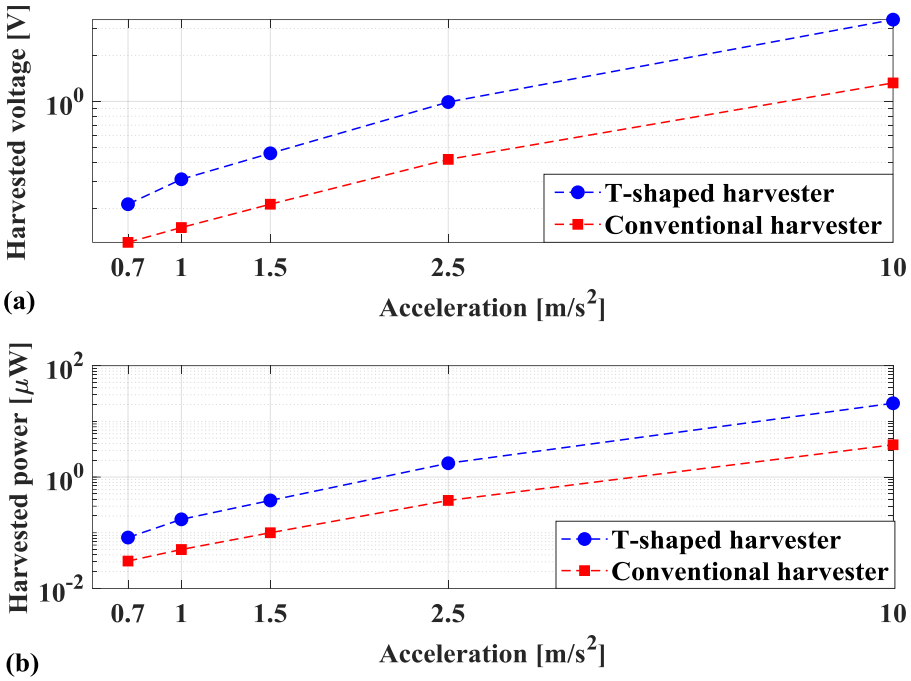

Fig. 48. Prototype measurement of (a) harvested voltage and (b) harvested power for the proposed T-shaped and conventional piezoelectric harvesters.

To provide a fair comparison between the performance of different MEMS energy harvesters, the normalized power density (NPD), which is the amount of the harvested power over occupied volume of the harvester times square of the acceleration magnitude ($\mu W \cdot cm^{-3} \cdot m^{-2} \cdot s^4$), a popular metric for determining the energy harvesting efficiency in the literature [5], is used in this work. In this regard, the prototyped T-shaped and conventional piezoelectric harvesters are analyzed based on their NPDs. According to the noted dimensions for the prototyped harvesters, the occupied silicon volumes of the T-shaped and conventional piezoelectric cantilevers are

3.4×10^{-4} cm^3 and 4.34×10^{-4} cm^3, respectively. If both harvesters are excited by the input acceleration of 1.5 m/s^2, the NPDs of the T-shaped and conventional harvesters are equal to 497 and 103, respectively. This comparison confirms that the T-shaped piezoelectric harvester is 4.8 times more efficient than the conventional one in energy harvesting. Moreover, such an energy conversion efficiency enhancement is favorably accompanied by the operational frequency reduction for our proposed T-shaped piezoelectric MEMS harvester.

In the following, the performance of our proposed power management system presented in Section 5.3 will be studied. We will show that our proposed T-shaped piezoelectric harvester with the integration of this SPMS can be considered as a practical solution deployed in the real environment for powering up a wide range of low-power electronic devices.

In our experiments, the functionality of the proposed SPMS was investigated by utilizing the discrete components available in the market. The detailed information regarding the components, their nominal values, and manufacturers are listed in Table 14. First of all, a numerical study was carried out by using LTspice simulator. It was assumed that the piezoelectric MEMS vibration harvester can maximally generate 1.5V. So the input voltage (i.e., V_{in}) of our SPMS was considered to be an AC signal with the amplitude of 1.5V. The performance of each particular section within the SPMS is depicted in Fig. 49 when the system reached its steady state. From this figure, it can be seen that the generated AC signal was rectified, and the boosted voltage by the DC-DC converter reached up to 5 volts (i.e., V_{Cout}). The converter switching frequency was determined to be 30 kHz. The threshold voltage of the N-channel JFET was 3.4V. Based on the JFET behavior, the current flowing through the output was limited and the voltage at the load side (i.e., V_{out}) was stabilized around 3.4V.

Table 14. Description of the utilized off-the-shelf discrete components for our proposed SPMS in the prototype measurement.

Components	Description
Zero-threshold NMOS transistor	ALD110800 (manufactured by Advanced Linear Devices)
Zero-threshold PMOS transistor	ALD310700 (manufactured by Advanced Linear Devices)
Super-capacitor ($C_{Starrup}$)	5000 uF aluminum electrolytic capacitor (manufactured by Illinois capacitor)
Voltage detector#1	S-1009 series threshold voltage of 1.5V (manufactured by ABLIC U.S.A. Inc.)
Microcontroller	ATTINY 43U-SU (manufactured by Atmel AVR)
NMOS switch transistor	SI5515DC (manufactured by Vishay Siliconix)
Inductor	100 mH fixed inductor (manufactured by Bourns Inc.)
Diode	Schottky diode (manufactured by ON Semiconductor)
Capacitor (C_{Out})	100 uF aluminum electrolytic capacitor (manufactured by Illinois capacitor)
Voltage detector#2	S-1009 series threshold voltage of 3.3V (manufactured by ABLIC U.S.A. Inc.)
N-JFET	2N5458 (manufactured by Central Semiconductor Corp)

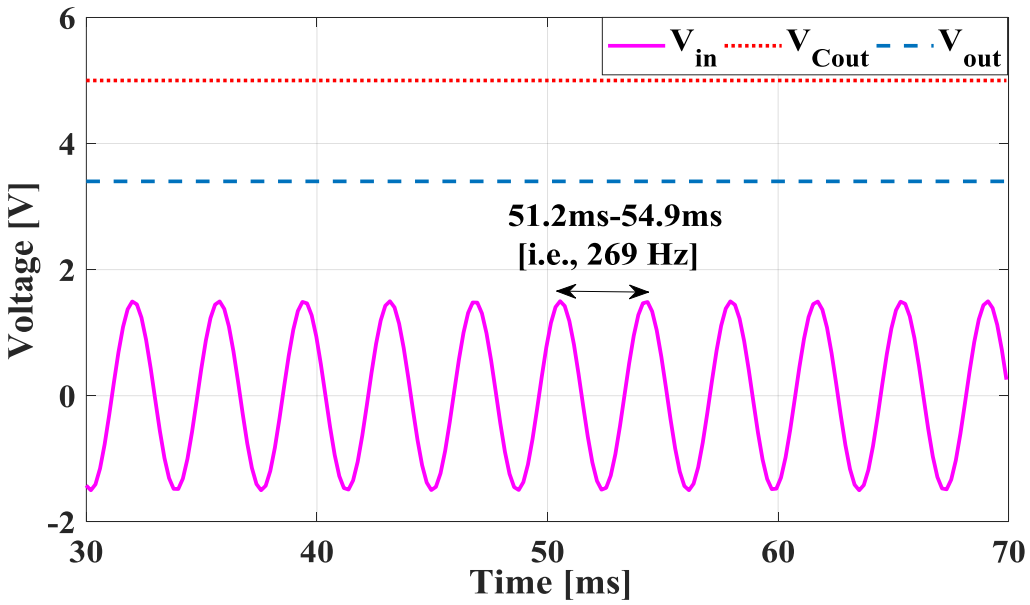

Fig. 49. Performance evaluation of the proposed SPMS structure by using LTspice software.

To demonstrate the capability of gaining higher rectification efficiency by the MOSFET rectifier in comparison with the conventional diode bridge rectifiers, we experimentally rectified

the AC input signal with different amplitudes by using our developed zero-threshold MOSFET rectifier in addition to the conventional diode bridge one. The prototype measurements with their rectification efficiencies for both rectifiers are illustrated in Fig. 50. As shown in this figure, the amount of voltage drop in the rectified output signal for the zero-threshold MOSFET rectifier is considerably smaller than that of the diode-based one. Once the amplitude of the input AC signal is relatively small (i.e., 700 mV), a large portion of the harvested energy is dissipated by the diodes (i.e., rectification efficiency of only 65%). In contrast, with the same input AC signal, our proposed zero-threshold MOSFET rectifier provides much higher rectification efficiency (i.e., 95%). Since the amplitude of the generated voltage by the MEMS harvesters is typically relatively small, our proposed zero-threshold MOSFET rectifier has promising advantages for being used as the AC-DC converter for the general MEMS vibration harvesters.

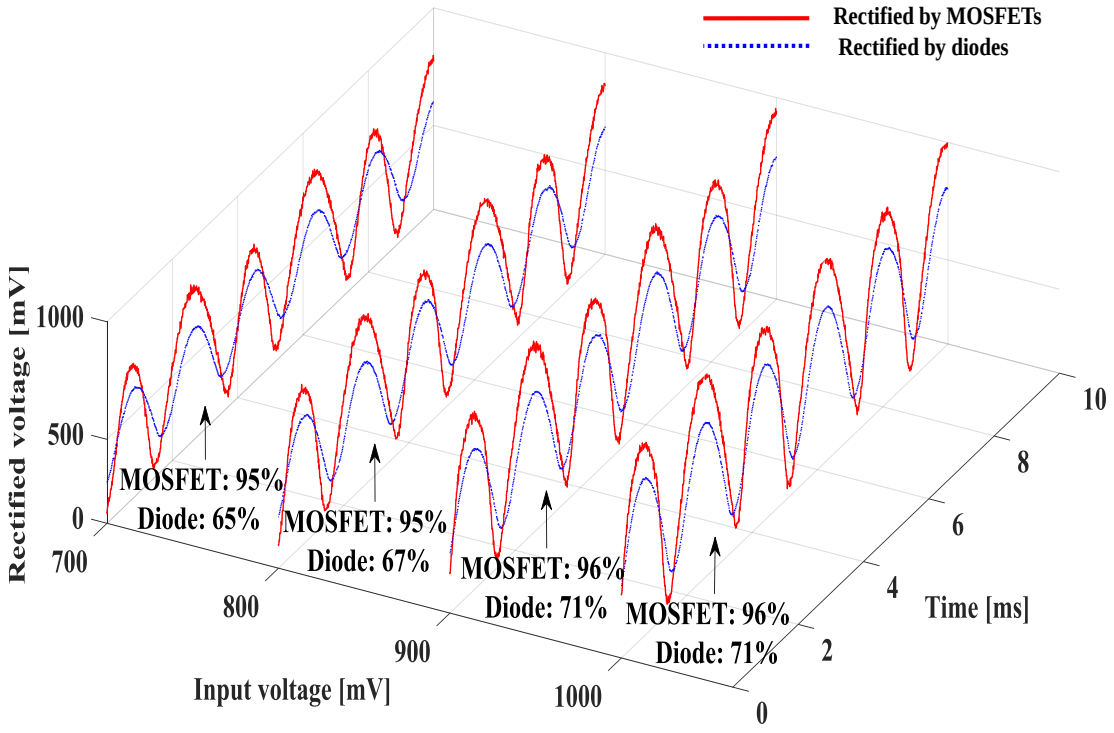

Fig. 50. Prototype measurement of the rectified voltage by the zero-threshold MOSFET (red) and conventional diode bridge (blue) rectifiers with their computed rectification efficiencies under different input voltages.

The overall performance of the proposed SPMS from our prototype measurement is demonstrated in Fig. 51. First of all, the input AC signal (i.e., V_{in}) with the amplitude of 1.5V is effectively converted to a rectified DC voltage (i.e., V_{rec}) by the zero-threshold MOSFET rectifier. Once the level of the accumulated voltage in the super capacitor reaches 1.5V, which is identical to the microcontroller power supply voltage and the detecting voltage of Voltage-Detector#1, the microcontroller becomes active to generate clock signal for the subsequent DC-DC converter. As shown in Fig. 51, the clock signal commences at 5ms, while the booster is activated to increase the rectified voltage (i.e., V_{Cout}) up to 4.7V at 50ms. When the boosted voltage reaches 3.3V at 10ms, the Voltage-Detector#2 at the load limiter part is enabled. Thereafter, the voltage can be delivered to the load (i.e., V_{out}). It is worth pointing out that after 10ms the amplitude of the delivered voltage to the load would be maintained at 3.4V, while the boosted voltage keeps increasing up to 4.7V.

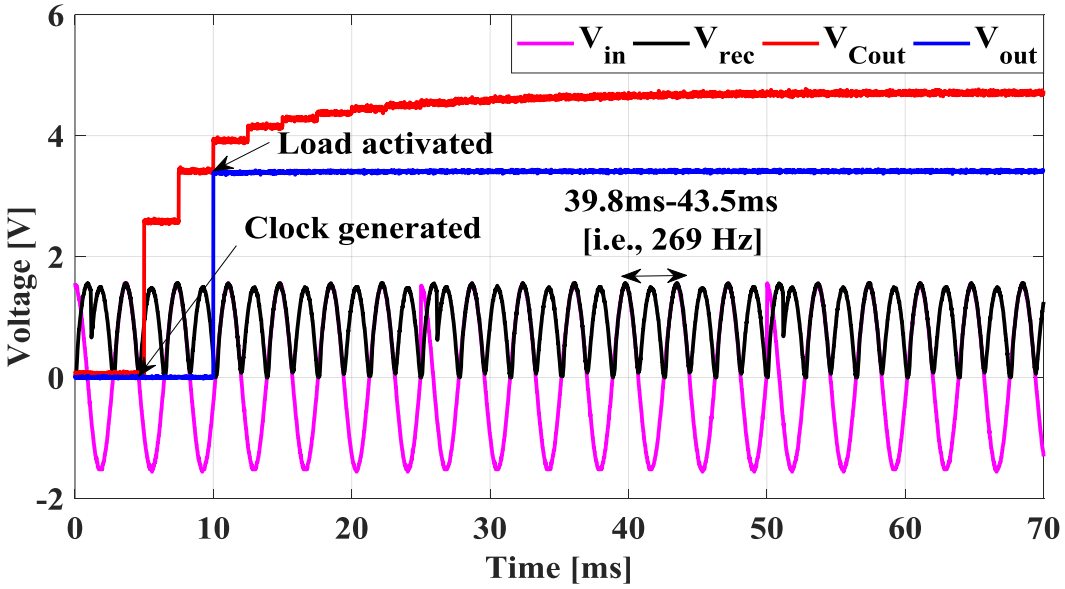

Fig. 51. Performance demonstration of the proposed SPMS structure from our prototype measurement.

The comparison between the illustrated results in Figs. 49 and 51 shows a good agreement between our obtained results from the numerical simulation and experimental measurement. In addition, since our proposed circuit as the power management system of the piezoelectric MEMS harvesters does not require any external power supplies, the entire system can just operate by the harvested AC power. Without using any active feedback, our proposed SPMS is able to increase the level of the input voltage to be delivered to the load side reliably.

5.5. Summary

In this chapter a new T-shaped piezoelectric MEMS harvester featuring higher power density and lower resonant frequency was proposed. We demonstrated that a large amount of stress/strain can be obtained not only from the anchor region just as the conventional straight-cantilever harvesters, but also from the tip part of the T-shaped piezoelectric structure. We presented analytic models for estimating frequency response and validated their accuracy numerically and experimentally. The contributions of the T-segment structure in enhancing the energy conversion efficiency (by over 4.8 times) and reducing the operational frequency (by 36%) in the prototype measurement were discussed. Furthermore, we proposed a new circuit structure as the indispensable self-supplied power management system for general MEMS energy harvesters with its functionality numerically and experimentally validated.

Chapter 6 Nonlinear Multi-Mode Wideband Piezoelectric MEMS Vibration Energy Harvester

6.1. Introduction

Ordinarily, piezoelectric MEMS energy harvesters comprise a cantilever and a proof mass at the tip location. This type of harvesters, which operate on a single-degree-of-freedom (SDOF), can be modeled by using a spring-mass system [178]. Although such a simple mechanical structure makes the fabrication process easier, it has a very narrow operational bandwidth [179]. Consequently, any variation in the ambient vibration frequency, which may occur in the real environment, would dramatically reduce the harvesting efficiency. During the past decade, to address the narrow operational bandwidth of the SDOF harvesters, several approaches have been proposed.

A feasible solution to enlarging the operational bandwidth of the electromagnetic- [102] and piezoelectric-based [180] energy harvesters is to utilize multiple cantilevers/diaphragms, which have different operational frequencies, to be arranged as an array [181]. Therefore, at each particular frequency at least one cantilever/diaphragm is capable of generating electrical voltage. Since such a method requires a large silicon area, the overall harvester power density is relatively low. Accordingly, there is a demand for the MEMS energy harvesters to be able to operate in a wide range of frequency with a considerable amount of power efficiency/density.

Another approach to broaden the operational bandwidth of piezoelectric MEMS energy harvesters is to utilize the mechanical stopper to limit space of the harvester oscillation [182]. A big silicon proof mass for reducing the resonant frequency along with several silicon cantilevers were integrated together with piezoelectric thin film (PZT). The mechanical collision between the

proof mass and harvester stopper provided nonlinear behavior. The reported experimental results in this study demonstrated that the proposed configuration could widen the operational bandwidth up to 17 Hz if the magnitude of excitation was high enough (around 1g). However, any decrease in the acceleration magnitude could dramatically reduce the operational bandwidth, that is, the effectiveness of the proposed method was unfortunately dependent on the input while in the real environment both magnitude and frequency of vibration are time variant.

Zhou *et al.* [183] proposed a piezoelectric harvester, which contained double beams and two tip masses attached together in a series configuration. The piezoelectric film for energy harvesting was placed on the surface of the second beam, while the first beam functioned as a dynamic magnifier. Although the proposed configuration in this study could enlarge the operational bandwidth based on the multi-mode phenomenon, it can hardly be considered as a practical method for MEMS piezoelectric harvesters due to its prerequisite of utilizing different thicknesses or materials for each particular segment [184].

The combination of electromagnetic force and piezoelectric effect, which can turn out to be bistable harvesters [185], was utilized by Tang *et al*. [186] for broadening operational bandwidth of the piezoelectric vibratory energy harvester. In this regard, the proposed harvester comprised two stages, while two permanent magnets were mounted at each stage. The experimental results showed that the widest bandwidth with this configuration was 20 Hz if the harvester was excited with 1g acceleration. However, the harvester bandwidth was strongly dependent on the magnitude of acceleration and, more important, utilizing permanent magnets makes the device fabrication somehow impractical for the general micromachining process.

A wideband piezoelectric harvester with a capability of being fabricated by MEMS process was introduced by Rezaeisaray *et al.* [187]. The proposed energy harvester comprised a big silicon

proof mass at the centre and two beams at the corners for suspending the proof mass. In this design, the piezoelectric films were deposited on the surface of the beams. Since the proposed configuration required a big proof mass and had narrow area for piezoelectric material deposition, the power density of the device was apparently quite low due to the size difference between its active (i.e., piezoelectric film) and passive (i.e., proof mass) regions.

To overcome the aforementioned issues, in this chapter we are motivated to propose a new wideband piezoelectric MEMS vibratory energy harvester, whose operational bandwidth can remain broad even though the magnitude of input acceleration is extremely small. Moreover, it can convert the ambient vibration to electricity more effectively and efficiently, while the entire device can be fabricated by using a regular micromachining process. Therefore, a doubly clamped unimorph piezoelectric cantilever associated with three proof masses at distinct locations is designed. Such a geometry features multiple-degrees-of-freedom (MDOF), which means that the harvesters with this geometry can harvest energy at multiple vibration modes (i.e., with multiple resonant frequencies). Since the proposed harvester has an unique geometry with nonlinear behavior, the conventional optimization methodologies for enhancing performance of MEMS piezoelectric harvesters, such as variant-mesh analysis [130] and correlation matrix [131], are useless due to the stringent requirement of acute human observation. To obtain the optimal performance of the harvester, we propose an automated design and optimization methodology based on GA, which can be performed with minimum human efforts.

The contributions of this chapter can be summarized as follows:

- We propose a new multi-mode wideband piezoelectric MEMS energy harvester with the capability of MDOF vibration, which ensures the device can generate voltage at multiple vibration modes.

- To optimize the performance of the proposed harvester, we introduce an automated design and optimization methodology based on GA.
- To demonstrate the manufacturability of the proposed harvester with the regular MEMS fabrication process, the optimized piezoelectric MEMS energy harvester was fabricated and testified.
- Our analysis and prototype measurement show that the uniform proof mass distribution in the proposed MEMS harvester geometry offers much higher power density in comparison with the conventional piezoelectric harvesters.

The major work in this chapter has been formally documented in one journal manuscript, one conference paper, and one filed patent application (as listed in the Appendix [Journal-4][Conference-2][Patent-1]).

6.2. Design and Modeling

The schematic of the proposed multi-mode piezoelectric MEMS vibration energy harvester with the capability of MDOF vibration is depicted in Fig. 52. It has special geometry anchored on two opposite sides, which can be viewed as a doubly clamped set of cantilevers or beams (two interchangeable terms throughout this chapter). As shown in Fig. 52, the proposed energy harvester is comprised of three proof masses, including a main central mass (i.e., $Mass_c$) and two lateral masses (i.e., $Mass_{l1}$ and $Mass_{l2}$) at various locations such that this configuration offers a uniform mass distribution in the entire MEMS harvester geometry. These three proof masses are suspended by the serpentine cantilevers, which have a deposition of piezoelectric material on their surface. With this geometry, the serpentine cantilevers are considered as the active area of the energy harvester. This arrangement associated with the proof masses at different locations makes the

proposed energy harvester capable of harnessing the vibration energy effectively at multi-mode frequencies.

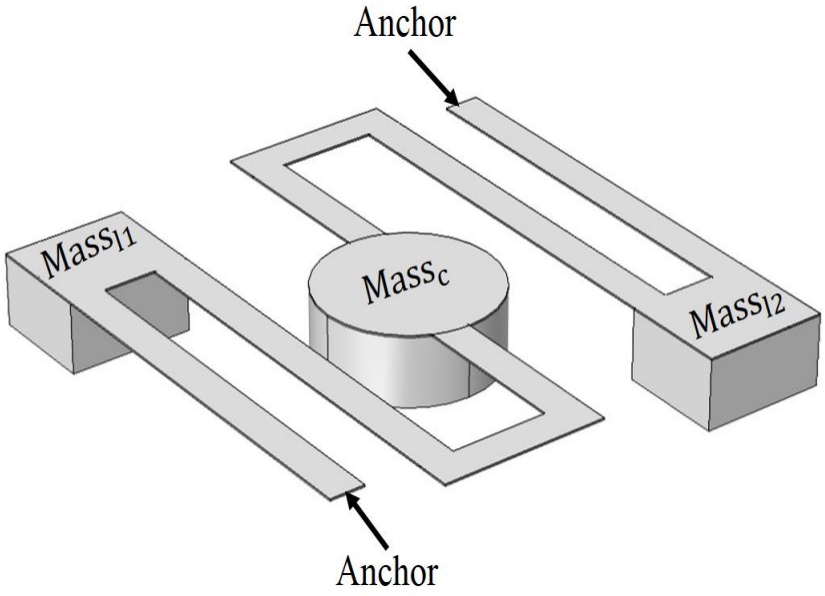

Fig. 52. Schematic of the proposed wideband multimode piezoelectric MEMS energy harvester.

To graphically demonstrate the performance of the energy harvester at different resonant frequencies, the COMSOL Multiphysics (Version 5.2a) software package was used. In this study, the piezoelectric MEMS energy harvester was modeled by using isotropic materials for both beams and piezoelectric film. By using *Eigenfrequency Study* in the Finite Element Modeling (FEM), the simulation results for the first three modes are shown in Fig. 53. To clearly exhibit the oscillation of the simulated energy harvester, each mode was recorded for one cycle in 5 continuous frames showing the vibration in the time domain. Frame-1 and Frame-5 show the maximum of the possible displacements in one cycle, while Frame-3 displays the neutral position.

Frames Number	1	2	3	4	5
1st Mode	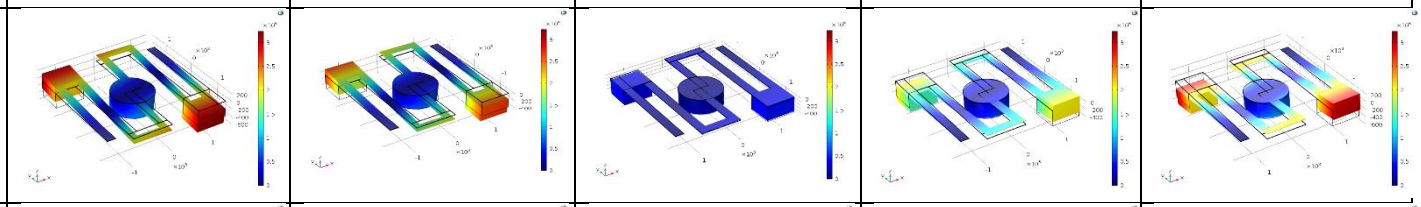				
2nd Mode	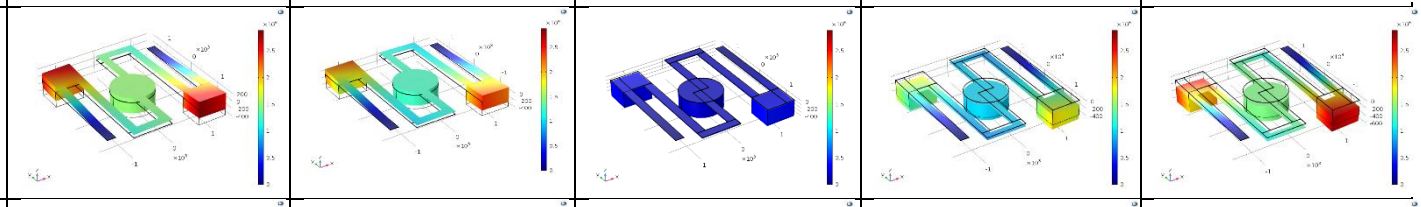				
3rd Mode	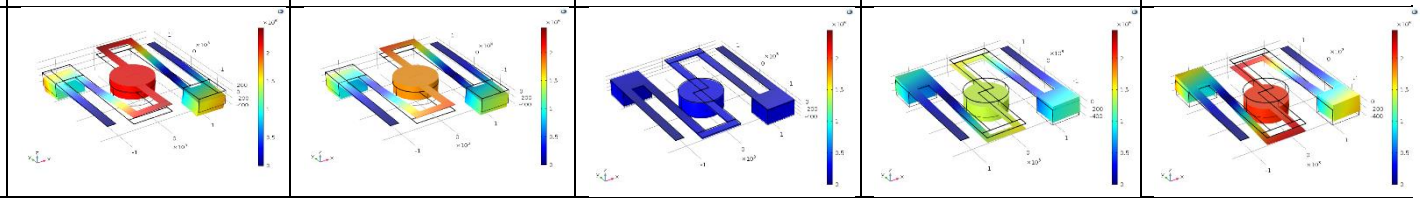				

Fig. 53. FEM simulations of the first three mode shapes for the proposed wideband piezoelectric MEMS vibration energy harvester.

As demonstrated in Fig. 53, in the first mode the central proof mass (i.e., $Mass_c$) has no motion, while the two lateral proof masses (i.e. $Mass_{l1}$ and $Mass_{l2}$) maximally oscillate in an opposite phase. In the second mode, the central proof mass is not fixed any more. Similar to the previous mode, the lateral proof masses have maximum upward and downward oscillations, while all these three proof masses vibrate in the same phase. The maximum oscillation in the third mode occurs to the central proof mass. In this mode, the two lateral proof masses at the corners have oscillations in the same phase with reference to each other, whereas their oscillation phase is opposite to that of the central proof mass.

The preliminary FEM simulations conducted on the geometry of the proposed harvester show that our harvester has nonlinear behavior during its operation in the second mode, while in the two other modes (i.e., the first and third modes) it behaves as a linear mechanical resonator. In the past,

the performance of the linear harvesters has been studied quite well [188]. Hence, the nonlinear behavior of our proposed harvester geometry during its operation in the second mode shape will be explained here in more detail. To demonstrate the nonlinear behavior of the energy harvester, the mechanical stiffness of the proposed structure is analyzed. From the literature, it is shown that the load-deflection equation for a nonlinear mechanical resonator can be expressed by [189][190]:

$$F(x)_{load} = k_L x + k_N x^3 \quad (57)$$

where k_L is the linear stiffness and k_N denotes the cubic (or nonlinear) stiffness. In order to identify those two mechanical stiffness coefficients, in the second mode by using FEM simulations, different forces were applied to a known node inside the device geometry and the corresponding relative deflections were measured. Based on the measurement results as depicted in Fig. 54, we used the curve fitting technique to determine the amount of the linear and cubic stiffness coefficients as follows: k_L=1.17 N/m and k_N=4.04e10 N/m^3. Consequently, it is expected to observe such nonlinear behavior when the device operates in its second mode. In Section 6.4, the effect of the specific mode and the nonlinear behavior of the harvester associated with the mechanical and electrical properties will be discussed in more detail numerically and experimentally.

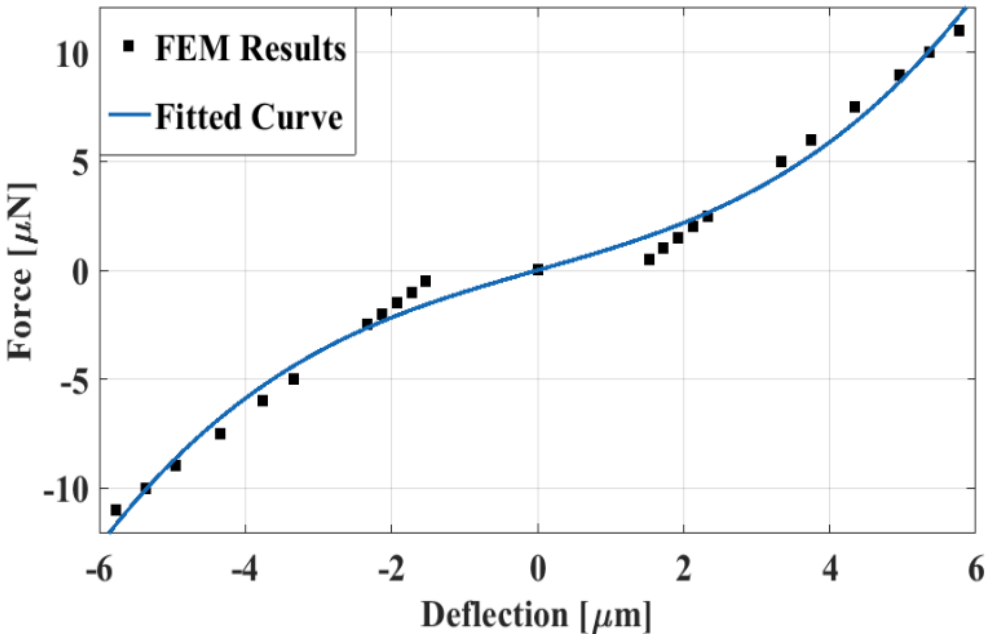

Fig. 54. FEM simulation results and fitted curve for estimation of linear and nonlinear mechanical stiffness coefficients, when the harvester operates in the second mode.

6.3. GA-Based Optimization

The genetic algorithm (GA), which is known as an evolutionary optimization methodology, is a procedure that can be used to optimize constrained and unconstrained complex problems by searching through a group of variables. Its capability in escaping from local optima and pinpointing the global optimum has made it as an outstanding optimization method [191]. The basic working flow of a standard GA is described in Algorithm 1. The optimization methodology commences by generating a random population of *n* individual chromosomes. In this regard, some variables, known as genes, are presented in the form of binary, which can randomly join to the fixed-length binary strings to create the chromosomes.

Once *n* chromosomes are generated, the fitness of each individual chromosome in the entire population is evaluated so that its suitability is ranked according to the fitness score. In the

selection-phase, two chromosomes that have the highest fitness scores in the population are selected. In the crossover-phase that is one of the most important operations in the genetic algorithm, a certain part of the chromosomes is exchanged between two individuals. Consequently, certain offspring are created. In the newly generated offspring, some of their genes are subject to a mutation, which means one bit (i.e., gene) is changed from 1 to 0 or vice versa.

After the completion of the mutation-phase, by using the newly created offspring, a new population is produced. Thereafter, in the replace-phase, the initial population is replaced with the newly created one from the accepting-phase for further algorithmic evolution and fitness evaluation. We normally call this updated population as new generation in terms of evolution. If a termination condition is satisfied for the current population, the algorithm will be stopped and the best solution will be reported. Otherwise, the algorithm will be repeated for g times, where g is the generation number determined by the users.

Depending on the number of the objectives in the fitness evaluation, the optimization problems can be categorized into single-objective and multi-objective problems. The single-objective optimization problem can only hold one objective along with multiple constraints, while a number of objectives and constraints can be included into the multi-objective problems. Most of the real-world search and optimization puzzles actually fall into the multi-objective optimization problems that need to strive for optimality to multiple ends with certain trade-offs anyway. From the literature, it is known that the GA-based optimization methodology features solid potential to be used for both single-objective and multi-objective problems [192].

Algorithm 1: The working flow of the GA.

1:	**Start:** Generate a random population with a size of *n* chromosomes
2:	**Fitness:** Evaluate the fitness of each chromosome in the entire population
3:	**Selection:** Select two chromosomes from the population based on their fitness
4:	**Crossover:** Exchange part of the chromosomes according to crossover probability for generating offspring
5:	**Mutation:** Mutate the offspring according to a mutation probability
6:	**Accepting:** Interpolate new offspring in the new population
7:	**Replace:** Utilize the newly generated population for a further run of the algorithm
8:	**Test:** If termination conditions are satisfied, stop, and report the best solution(s) from the current population
9:	**Repeat:** Go to step 2 for further evolution and evaluation. Repeat the algorithm for *g* times (i.e., generations)

In this chapter, the multi-objective GA has been utilized to optimize frequency operation of the proposed piezoelectric MEMS harvester. In this way, the lateral proof masses located at the corners, i.e., $Mass_{l1}$ and $Mass_{l2}$, and the anchor locations have been considered as optimizable parameters. The GA fitness functions, for the multi-objective optimization, are defined as:

$$\begin{aligned} &\text{Minimize: } \mathrm{mean}(f_1, f_2, f_3), \\ &\text{Minimize: } \begin{Bmatrix} \text{sum of the intervals between} \\ (f_2, f_1) \text{and } (f_3, f_2) \end{Bmatrix}, \\ &\text{Subject to: design rules of the optimizable parameters,} \end{aligned} \tag{58}$$

where f_1, f_2 and f_3 are the resonant frequencies of the first, second, and third modes, respectively. Their amounts can be obtained from numerical FEM simulation conducted by COMSOL Multiphysics. Therefore, an optimization engine can be built up by linking the GA implemented in MATLAB to COMSOL Multiphysics by the LiveLink module [193], as shown in Fig. 55. The functionality of the GA-based optimization method aimed for reducing resonant frequencies and enhancing bandwidth by selecting a geometry with nonlinear behavior will be illustrated and analyzed in the following sections.

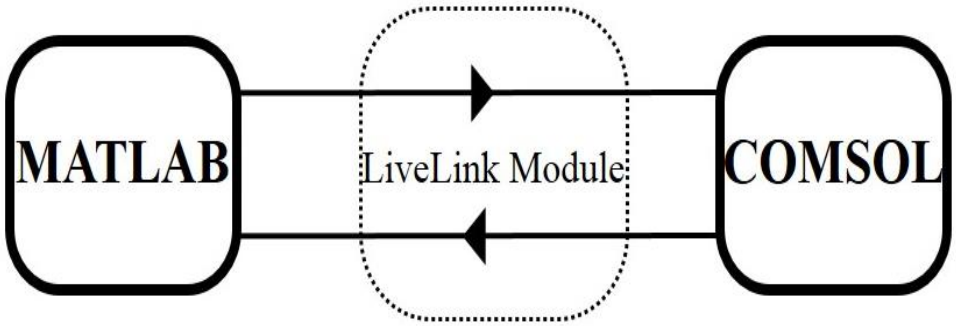

Fig. 55. Flow diagram of the utilized MATLAB-COMSOL optimization methodology.

By utilizing the GA-based optimization methodology described in this Section, an optimum size for the dimensions of various elements in the energy harvester can be determined in accordance with the defined fitness functions. In this regard, the anchored beam length L_a (i.e., the distance from the lateral proof masses $Mass_{l1}$ and $Mass_{l2}$ to their corresponding anchors), and the length L_m of $Mass_{l1}$ and $Mass_{l2}$, as shown in Fig. 56, were defined as optimizable parameters. The GA-based optimization method then strives to satisfy the defined fitness functions by optimizing the values of these two parameters subject to their design rule constraints. During the optimization process, the rest of the geometric features in the proposed energy harvester are assumed to be un-optimized and constant as listed in Table 15.

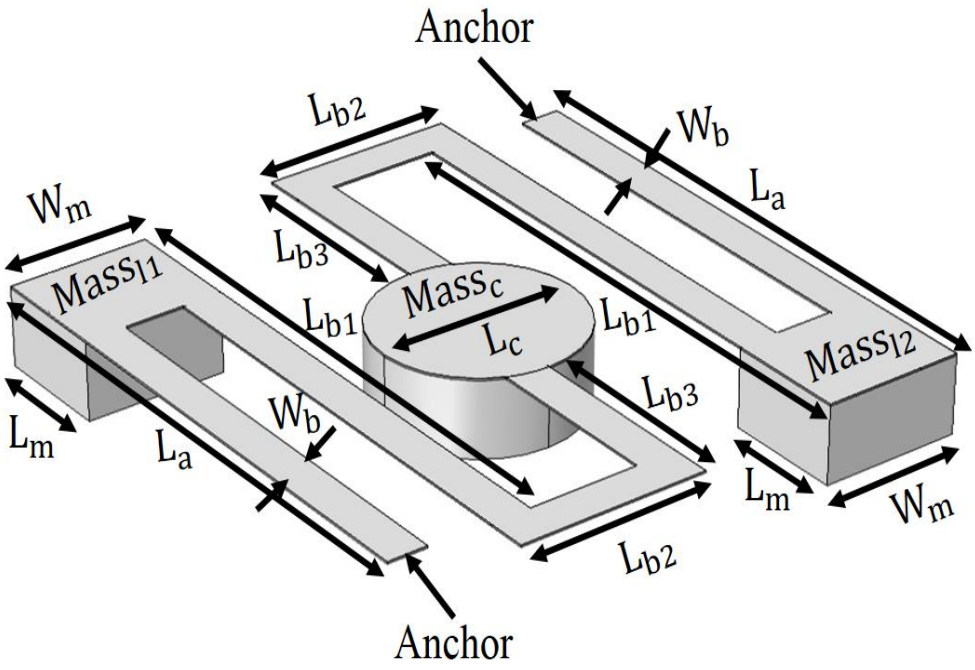

Fig. 56. Schematic of the proposed multimode piezoelectric MEMS energy harvester with its specified physical parameters.

Table 15. Sizes of the un-optimized parameters for estimation of the frequency response during the GA-based optimization.

Parameters	**Description**	**Size [μm]**
L_c	Diameter of the proof mass in the center	1000
L_{b1}	Length of the first beam	3000
L_{b2}	Length of the second beam	950
L_{b3}	Length of third beam	1055
W_b	Beam width	200
W_m	Width of the proof masses at the corners	700

6.4. Experimental Results and Discussion

The effectiveness of the GA-based optimization method is dependent on the size of the search space, which can be determined by two user-defined parameters, i.e., population size and generation number. To show the effect of these user-defined values on optimization results, the GA-based optimization method was executed with two different population sizes, 10 and 20, under the same generation number of 20. To demonstrate the capability for enhancing the frequency operation of the energy harvester by using the GA-based optimization methodology, we defined an un-optimized structure, where the optimizable variables were chosen to be the median values as per their allowed ranges. In addition, for the comparison purpose, COMSOL optimization module [150] as a widely available commercial optimization tool for optimizing the MEMS structures was utilized. The obtained results for the un-optimized and optimized energy harvester devices are summarized in Table 16. In this table, the allowed ranges for the optimizable parameters, which are defined by their design rule constraints, are listed in the second and third columns. The calculated fitness functions for mean frequency and frequency interval sum are presented in the 7^{th} and 8^{th} columns, respectively. The calculated mean harvested voltage at the operational bandwidth of the device is listed in the 9^{th} column. Moreover, the required runtime to conduct the GA- and COMSOL-based optimization is shown in the 11^{th} column.

Table 16. Simulated resonant frequencies and calculated fitness functions for the un-optimized and optimized wideband piezoelectric MEMS energy harvesters.

Parameter	**Mass length L_m [μm]**	**Anchor location L_a [μm]**	**1st mode f_1 [Hz]**	**2nd mode f_2 [Hz]**	**3rd mode f_3 [Hz]**	**Mean frequency [Hz]**	**Frequency interval sum [Hz]**	**Mean harvested voltage [mV]**	**Population size [Number]**	**Run time [min]**
Range	[500-1000]	[500-3100]								
Un-OPT	750	2050	314	338.82	429.6	360.8	115.6	26.01	-	-
Com-OPT	745	3000	196	218	305	239	109	31.25	-	283
OPT1	546	2380	284.46	288.41	348.92	307.26	64.46	37.98	10	141
OPT2	603	2780	227.48	258.58	291.01	259.02	63.53	53.69	20	280

As listed in Table 16, the un-optimized harvester, labeled as *Un-OPT*, has to operate at higher frequencies, while the various modes are observed largely separate from one another in the frequency domain. The optimized device by the COMSOL optimization module, named as *Com-OPT*, can operate in the lower frequencies in comparison with the un-optimized one. However, its first three modes are not sufficiently close to one another. In all, the *Com-OPT* objective fitness functions of the mean frequency and the frequency interval sum are reduced by 34% and 5.7%, respectively, in comparison to the un-optimized harvester. Moreover, the obtained result by executing the GA-based optimization with a population size of 10, labeled as *OPT1*, shows that our proposed optimization methodology can reduce the operational frequencies and frequency intervals by a factor of 15% and 44%, respectively, with reference to *Un-OPT*. The reduction in the operational frequency and frequency interval for the optimized harvester with a population size

of 20, named as *OPT2*, can be further improved to 28% and 45%, respectively, compared to *Un-OPT*. Thus, it can be seen that increasing the population size of the GA process can improve the effectiveness of the optimization method in searching for optimum solutions, since a larger population size provides broader search space for the GA to pinpoint optimal values for the due parameters. On the other side, by increasing the population size, the required runtime also goes up.

A comprehensive comparison on the summarized data in Table 16 shows that for the optimized device *Com-OPT* with the COMSOL optimization module, only one objective fitness function (i.e., mean frequency) is reduced considerably, whereas its multiple mode frequencies located far away from one another make its mean harvested voltage relatively small. As a results, it may not be considered as a wideband piezoelectric harvester. In contrast, in our proposed GA based optimization, if a proper population size is determined, both objective fitness functions can be significantly reduced. This means all the modes are coupled together at the lower frequencies, which can help enhance the mean harvested voltage. Therefore, one can observe that *OPT2* achieves the highest mean harvested voltage. In summary, the optimized energy harvester *OPT2* can vibrate at lower frequencies, while its various resonant frequencies in different modes are sufficiently close to one another with a considerable amount of mean harvested voltage. Consequently, it is considered as a qualified wideband piezoelectric MEMS vibration energy harvester, whose performance will be further evaluated numerically and experimentally in the following.

Frequency spectrum obtained by performing FEM simulation on the finally optimized energy harvester, i.e., *OPT2*, is depicted in Fig. 57. To compute the device frequency response, the velocity of the three proof masses, (*i.e.*, $Mass_c$, $Mass_{l1}$, and $Mass_{l2}$) are measured individually. From these simulation results, one can observe that the energy harvester *OPT2* has its maximum

oscillation at the resonant frequency of the second mode. Furthermore, Fig. 57 clearly shows that at the resonant frequency of the first mode, the central proof mass (i.e., $Mass_c$) has almost no oscillation, while the other two lateral proof masses (i.e., $Mass_{l1}$ and $Mass_{l2}$) are able to vibrate. Thus, by considering the oscillation among all the parts, the energy harvester *OPT2* can function in three modes, where the first, second, and third resonant frequencies are observed at 227.48 Hz, 258.58 Hz, and 291.01 Hz, respectively.

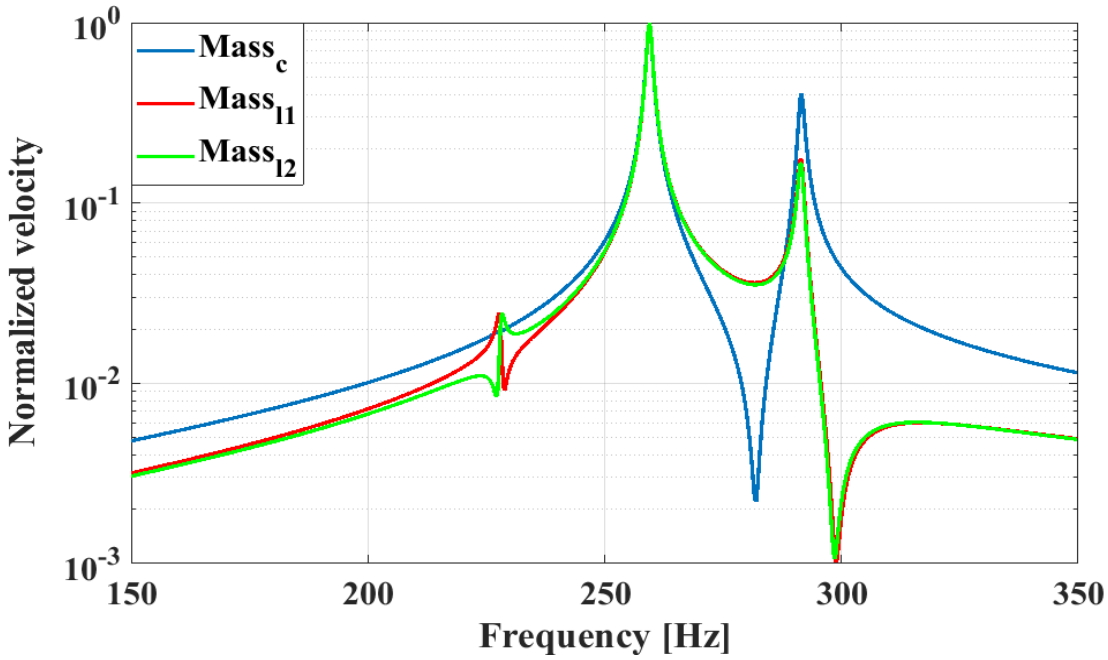

Fig. 57. Frequency spectrum obtained by performing FEM simulation on the optimized nonlinear multi-mode piezoelectric MEMS harvester.

According to the IEEE standard on piezoelectricity [138], if the electrodes are arranged according to a capacitor model [137], the harvested open circuit voltage V_{op} is represented by equation (59):

$$V_{op} = g_{31} t_p \sigma_p, \tag{59}$$

where g_{31} is the piezoelectric coefficient, t_p is piezoelectric material thickness, and σ_p is the applied stress on the piezoelectric material. Consequently, the efficiency of these energy harvesters is proportional to the capability of their geometries in absorbing mechanical stress. To demonstrate the active areas of the energy harvester *OPT2* for harnessing mechanical stress, its stress profile at each individual mode is shown in Figs. 58(a)-58(c).

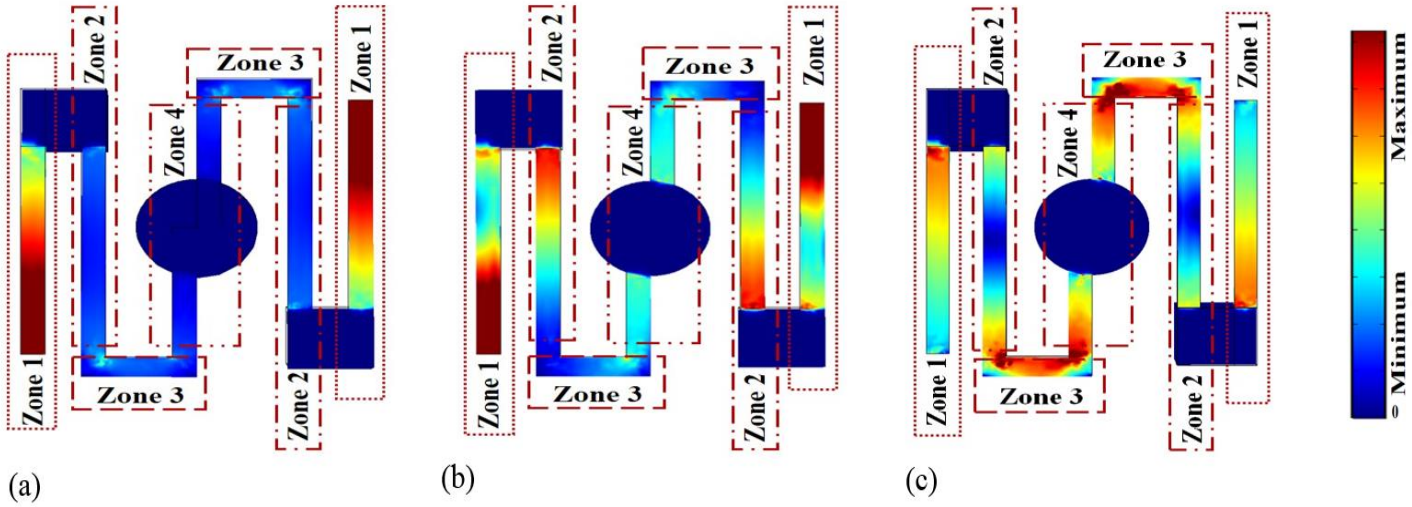

Fig. 58. Von-Mises stress distributions on piezoelectric film of the proposed multimode harvester in the: (a) first, (b) second and (c) third modes.

According to Fig. 58(a), when the energy harvester *OPT2* is operating at its resonant frequency in the first mode, the maximum actuating stress can be observed in Zone-1. Once the energy harvester *OPT2* is excited at the resonant frequency in the second mode as shown in Fig. 58(b), a considerable amount of stress is observed in Zones 1-2. In addition, a certain amount of applied stress is formed in Zone-4 besides Zone-3. In Fig. 58(c), it is demonstrated that if the energy harvester *OPT2* oscillates at the resonant frequency in its third mode, Zones 3 and 4 can considerably absorb the applied stress, while Zones 1 and 2 are also capable of converting the absorbed stress to electricity in these regions. This analysis of stress distribution shows that at

various resonant frequencies the stress can be harnessed almost all over the entire body of the energy harvester. In other words, all segments of the energy harvester are involved in energy harvesting, which results in extremely high power density for this device.

In Figs. 59(a)-(d) strain distributions along the individual beams for each specific mode are depicted to illustrate the efficiency of the piezoelectric MEMS energy harvester *OPT2*. The magnitude of strain is considerable only in Zones 1 and 2 when the harvester is excited in its first mode, where the active area for accumulation of strain is 43% with average strain magnitude of 4.3×10^{-6}. In contrast, during the operation in its second and third modes, all the geometric zones are functional. That is to say, 60% of the device surface area is attributed to the active area for energy harvesting in the second and third modes with an average strain magnitude of 6.5×10^{-6} and 4.7×10^{-6}, respectively. Since the majority of the device surface area (i.e., 60%) is active for collecting and converting mechanical energy to electricity, it can be seen that the structure of the energy harvester *OPT2* with our proposed unique geometry and balanced mass distribution has high efficiency in generating voltage. Furthermore, as shown in Figs. 59(a)-(d), the proof masses cause stiffening phenomenon so that the magnitude of strain on the proof masses is zero. Thus from the simulation results, it can also be seen that the peak strains always take place in such regions as the anchor locations, corners, and vicinities of the proof masses. Based on a comprehensive comparison between Figs. 58(a)-(c) and 59(a)-(d), it can be understood that the higher efficiency in energy harvesting occurs in the second and third modes, while the stress/strain is distributed along the entire geometry of the proposed energy harvester.

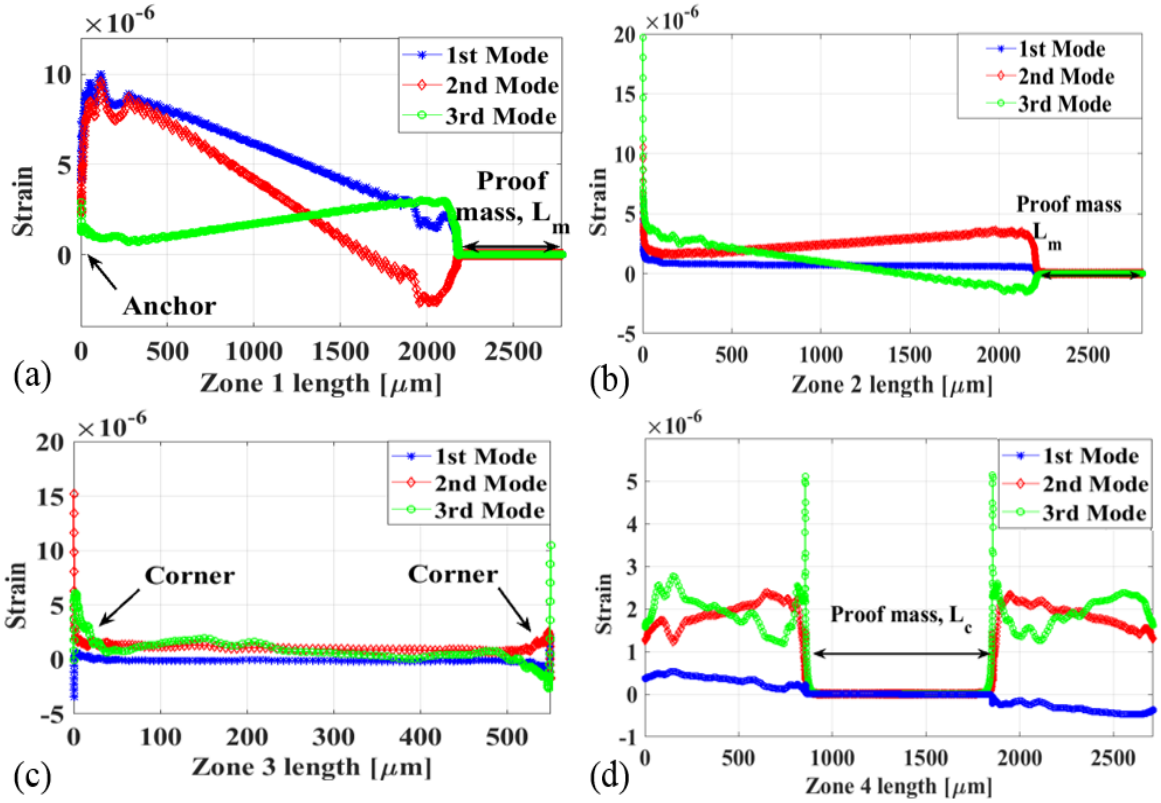

Fig. 59. Strain distribution magnitude in the specific zones: (a) Zone 1, (b) Zone 2, (c) Zone 3, and (d) Zone 4.

The optimized harvester *OPT2* was fabricated by using the micro-fabrication process described in Section 3.4.1. The finger-top and SEM images of the prototyped energy harvester are depicted in Figs. 60(a)-(b).

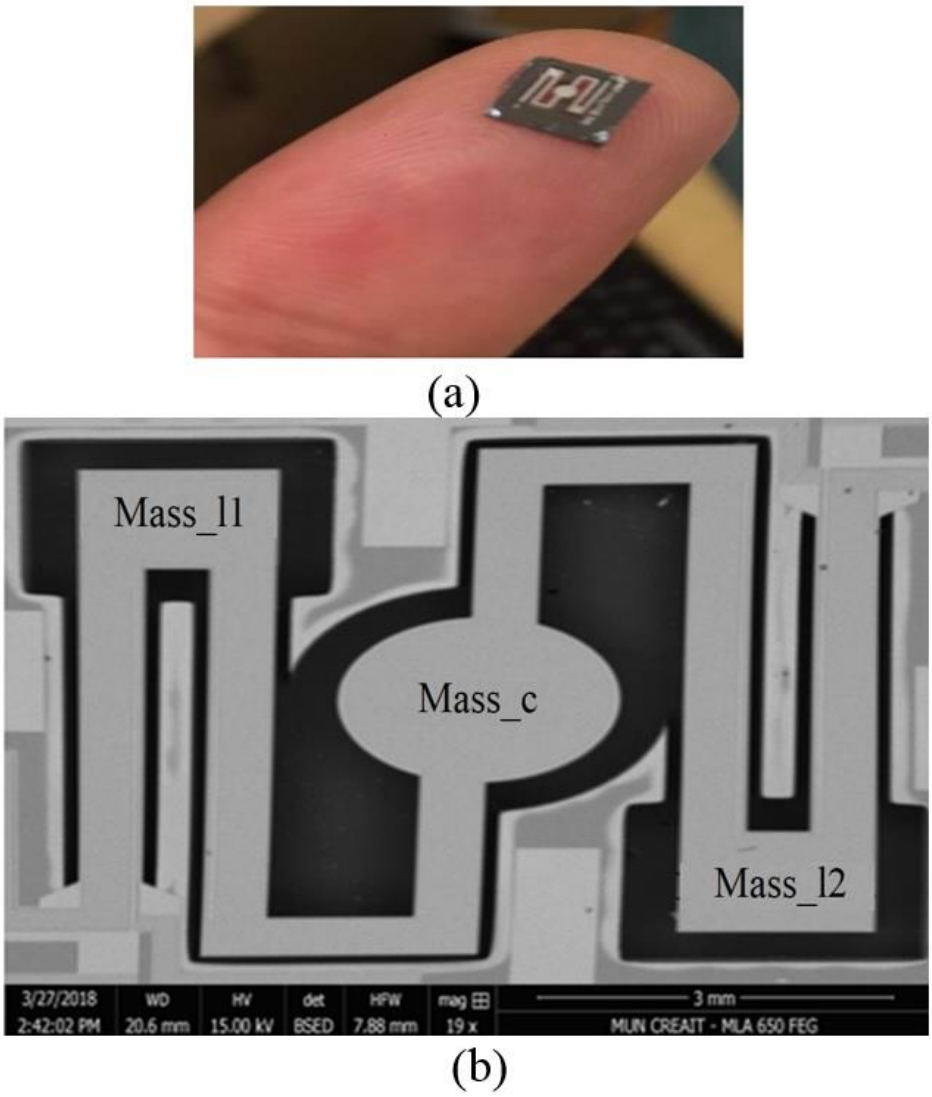

Fig. 60. The prototyped nonlinear multi-mode piezoelectric MEMS vibration harvester with its (a) finger-top, and (b) SEM top view images.

The frequency response in terms of deflection and harvested voltage was measured by using the following experimental setup. The prototyped energy harvester was excited by using a mechanical shaker (Type 4809 manufactured by Brüel & Kjær), whose vibration frequency and magnitude were controlled by a function generator (Agilent 3250) and amplified by a high power amplifier (manufactured by Brüel & Kjær). The shaker acceleration amplitude was monitored by an accelerometer (DXL 3350 manufactured by Analog Devices), which was attached to the shaker

platform. Laser displacement sensors (LK-H022 manufactured by Keyence) were mounted on a support system on the top of the harvester to measure the deflection of the proof masses along the Z-axis over the time when the prototyped energy harvester was excited. The velocity of the proof masses can be determined by using a ratio between the measured deflection and the time spent. The generated voltage by the prototyped MEMS piezoelectric harvester was measured by using a high performance oscilloscope (DSA 7040 manufactured by Tektronix) through a high impedance probe.

Figure 61 shows the experimental measurement of frequency spectrum for the prototyped energy harvester. The velocity of each proof mass, i.e., $Mass_c$, $Mass_{l1}$ and $Mass_{l2}$, was measured by using the laser displacement sensors when sweeping the operational frequency of the shaker in the range of 150 Hz-350 Hz. The first three peak velocities, which represent the first three modes of the MEMS energy harvester, were observed at 227 Hz, 261.8 Hz and 286 Hz, respectively. The vicinity of the resonant frequencies in these three modes confirms that the structure of such a piezoelectric MEMS vibration energy harvester described herein has MDOF behavior. The maximum deflection was seen in the second mode, while the central proof mass $Mass_c$ experienced little oscillation in the first mode. The velocity magnitude of the central proof mass $Mass_c$ in the third mode is considerably higher than that of the other two lateral proof masses $Mass_{l1}$ and $Mass_{l2}$. It is worth noting that this measured performance from the fabricated MEMS harvester (i.e., Fig. 61) matches the numerical result from the FEM simulation (i.e., Fig. 57) very well. The maximum discrepancy between the obtained results by the prototyped measurement and numerical simulation belongs to the higher order mode (i.e., the third mode) with an error of less than 2%. Thus, this high level of accuracy can help validate the correctness of our applied FEM model in the numerical simulations.

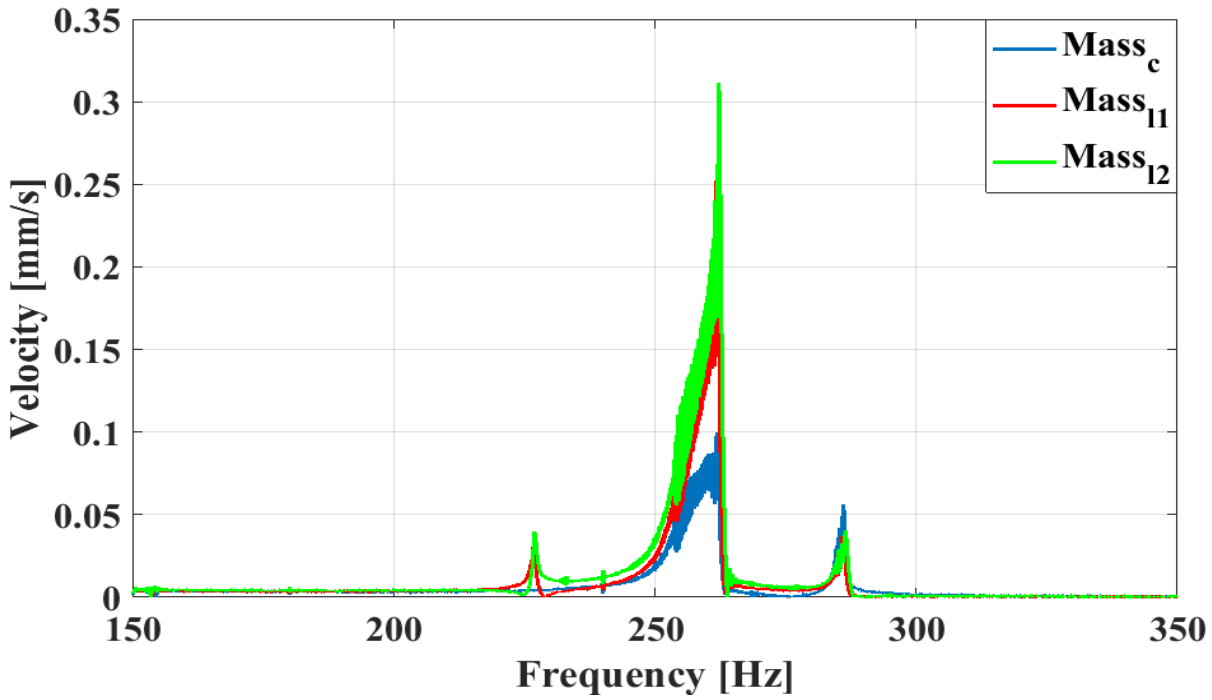

Fig. 61. Frequency spectrum obtained by performing experimental measurements on the fabricated nonlinear multi-mode piezoelectric MEMS harvester.

Furthermore, according to the illustrated frequency spectrum in Fig. 61, it can be seen that the prototyped energy harvester in the second mode is highly nonlinear, due to the jump phenomenon behavior [194]. This nonlinear response was investigated under different magnitudes of acceleration. In Fig. 62(a), by forward frequency sweeping, the $Mass_c$ velocity responses in the time domain, under acceleration of 0.2 m/s^2, 0.5 m/s^2, 0.7 m/s^2, and 1m/s^2, are shown. Moreover, to demonstrate its response in the frequency domain, based on the recorded data in the time domain their Fast Fourier Transforms (FFTs), which were computed by using MATLAB, are presented in Fig. 62(b). Once the prototyped harvester was excited with a quite small acceleration amplitude (i.e., 0.2 m/s^2), its nonlinearity was observed with a jump phenomenon, due to the geometric stiffness hardening, at 257 Hz (black curve). By increasing the acceleration amplitude to 1 m/s^2, the jump phenomenon shifted to 271 Hz. That is to say, the nonlinear behavior of the proposed

energy harvester is available even if the amplitude of excitation is significantly smaller [154]. In the second mode when the prototyped energy harvester was under excitation, the vibration accelerations of 0.2 m/s^2, 0.5 m/s^2, 0.7 m/s^2 and 1 m/s^2 correspond to the bandwidths of 5.3 Hz, 9.8 Hz, 14 Hz and 16 Hz, respectively.

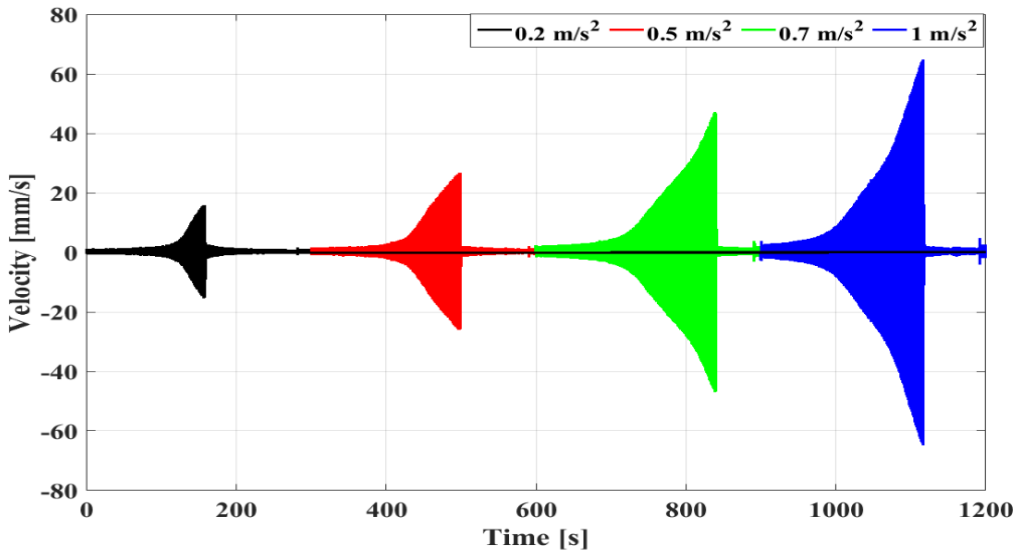

(a)

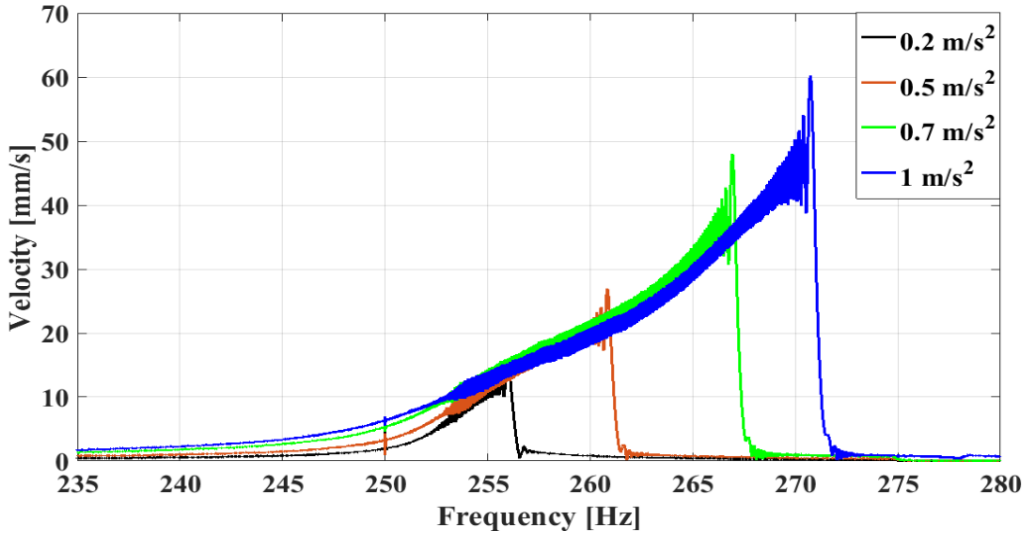

(b)

Fig. 62. Measured velocity of the central proof mass (i.e. *Mass$_c$*) when the energy harvester was excited by forward frequency sweeping in the second mode, where the data is shown (a) in the time domain and (b) in the frequency domain

The capability of the prototyped energy harvester was further studied by measuring the real time generated voltage. Figures 63(a)-(c) illustrate the oscilloscope traces at the resonant frequency in each individual mode when the prototyped energy harvester was excited by a sinusoidal acceleration with a magnitude of 0.5 m/s^2. A comparison between the magnitude of the harvested voltages in each mode shows that once the prototyped energy harvester is excited in its second mode, the maximum harvested voltage can be obtained with a 119 mV peak voltage. The peak harvested voltages are 20 mV and 57 mV in the first and third modes, respectively. While the prototyped energy harvester in the third mode has a higher efficiency than its first mode, it can be seen that the prototyped piezoelectric MEMS vibration harvester can generate voltage at multimode frequencies. Moreover, such a level of harvested voltage clearly confirms our proper geometric design in terms of strain/stress distribution inside the energy harvester.

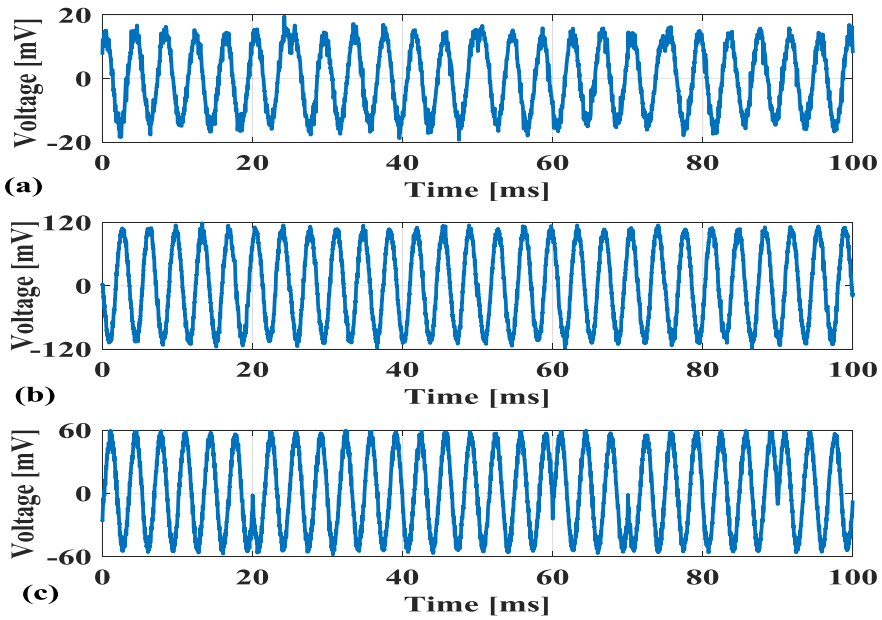

Fig. 63 Measured harvested voltage with acceleration of 0.5 m/s^2: (a) in the first (i.e., 227 Hz), (b) second (i.e., 261.8 Hz), and (c) third (i.e., 286 Hz) modes, respectively

In order to estimate the delivered power to a load by the prototyped piezoelectric MEMS energy harvester, the impedance of the harvester, which is known as a source impedance [151], was measured by an LCR meter (Model 889B manufactured by BK Precision). It was found that for the low frequencies, the source impedance was around 11.65 kΩ. Thus, it is expected that by providing an optimal load resistance, whose value is equal to the source impedance of 11.65 kΩ, a perfect impedance matching network between the source and load parts can be achieved. In this way, it is assumed that the load impedance is purely resistive and the average output power can be estimated by:

$$\mathrm{P_{avg}} = \frac{\mathrm{V_{rms}^2}}{\mathrm{R_L}}; \tag{60}$$

where V_{rms} is the RMS voltage measured at the output and R_L denotes the optimum load resistance. Under such assumptions, it is determined that when the prototyped MEMS energy harvester is excited with a sinusoidal acceleration having magnitude of 0.5 m/s^2, it is able to generate 0.02 μW, 0.61 μW and 0.14 μW in the first, second, and third modes, respectively.

When comparing harvester efficiency among the different energy harvesters, the normalized power density (NPD), which is a ratio between harvested power and volumetric size of the harvester per acceleration squared, is widely utilized in the literature [195]. By considering this metric, a comparison of the properties (such as NPD and operational frequency) among our prototyped energy harvester and various energy harvesters previously reported in the literature was conducted as listed in Table 17. According to the summarized data, it is clear that our prototyped energy harvester (i.e., the last row in Table 17) is one of the most efficient piezoelectric harvesters with a considerably large bandwidth. It is worth noting that the structure of the proposed energy

harvester described in this chapter provides sound advantages in terms of energy efficiency in the MEMS scale, with a smaller occupied volume of silicon wafer, due to the serpentine structure.

Table 17. Comparison of the properties among the recently reported wideband MEMS/portable vibration energy harvesters.

Ref.	Tech.	Volume [mm^3]	Substrate	Accel. [m/s^2]	Freq. Range [Hz]	Power [μW]	NPD [$\mu W \cdot cm^{-3} \cdot m^{-2} \cdot s^4$]
[196]	El*	27.1	Si	1.372	520-591	0.083	1.63
[197]	El	187	Si	0.9	148-172	4.95	32.68
[198]	Eg	35	Si	9.8	840-1490	0.0055	0.00163
[199]	Eg	43.35	FR4	10	190-244	0.45	0.0045
[200]	Pi	112	Si	19.6	859.9-924.5	82.24	1.91
[201]	Pi	1419.35	Steel	0.392	4-8	2610	11969.8
[202]	Pi	6500	Si	0.5	387-398	52.9	32.55
[182]	Pi	10	Si	9.8	30-47	0.5	0.52
[203]	Pi	17.5	Si	7.84	12-26	0.87	0.008
[187]	Pi	18	Si	1.96	71.8-188.4	0.136	1.97
This work	Pi	4.1	Si	0.5	227-286	0.61	595.12

*El: electrostatic, Eg: electromagnetic, Pi: piezoelectric

6.5. Summary

In this chapter we presented a structure with the capability of multiple-degrees-of-freedom (MDOF) for widening the operational bandwidth of the piezoelectric MEMS vibration energy harvesters. The proposed structure has a unique geometry comprising a doubly clamped set of piezoelectric cantilevers with a serpentine shape and three proof masses located at different positions to provide uniform mass distribution. By using modal analysis and mechanical stiffness

computation, it is shown that the harvester is able to operate in the multiple modes with a strong nonlinear behavior at the resonant frequency in its second mode. Moreover, we proposed an automated optimization method based on genetic algorithm with minimal human effort. The optimization result was verified through FEM-based simulations and measurement of the prototyped MEMS harvester. It is shown that the performance of the proposed piezoelectric MEMS vibration harvester is well superior to that of the recently published portable energy harvesters in the literature.

Chapter 7 Design and Optimization of Piezoelectric MEMS Energy Harvesters Based on Artificial Intelligence and Fatigue Lifetime Analysis

7.1. Introduction

The silicon-based piezoelectric MEMS energy harvesters normally have a high operational resonate frequency (i.e., in the range of 500 Hz ~10 kHz) owning to their small physical aspects and the utilization of the silicon wafer as a substrate, which is strongly stiff and brittle. In contrast, the natural frequencies of the ambient vibration resources are mostly less than 200 Hz [152]. Thus, there have been multiple endeavors in the literature to offer the piezoelectric MEMS energy harvesters with the capability of operating in the real environment. Using a big proof mass at the tip of the piezoelectric cantilever was proposed as a practical method for resonant frequency reduction and conversion efficiency enhancement of the MEMS harvesters. In our previous study, as described in Chapter 6 [149], the multimodal behavior, which was obtained by using three discrete proof masses at different locations within the MEMS harvester, could successfully reduce the device resonant frequency. In more recent studies, the capability of micro-fabricated spiral [195] and T-shaped [188] piezoelectric energy harvesters were investigated. It was shown that such energy harvesters were more suitable than the conventional ones for being utilized in the real environment.

As a matter of fact, the obtained frequency reduction in the prior studies is not that considerable, which means further reduction along with the energy conversion efficiency enhancement for the silicon-based piezoelectric harvesters to make them a better fit for the

operation in the real environment is highly demanded. Therefore, in this chapter a doubly clamped cantilever with a serpentine pattern associated with several proof masses is proposed for resonant frequency reduction and efficiency improvement. Our proposed structure can offer sound features in reducing the MEMS geometry stiffness and increasing the total weight. Moreover, to optimize the performance of the proposed MEMS energy harvester, a new optimization methodology based on Artificial Intelligence (AI) has been also proposed. In this regard, a deep neural network for prediction of resonant frequency and harvested voltage is trained. Thereafter, this network is integrated with a genetic-algorithm-based optimization platform for tuning the harvester dimensions.

In addition, several previous studies have shown that the efficiency of the piezoelectric MEMS harvesters can be improved by using special mechanical topologies, such as cantilevers-on-membrane [169], serpentine cantilever associated with uniform mass distribution [149], and T-shaped piezoelectric cantilever [188]. Nevertheless, all of the methods above are solely focused on enhancing the efficiency of the piezoelectric MEMS harvesters regardless of the device failure status. It is obvious that the piezoelectric harvesters are only functional when being subject to cyclic loading conditions. On the other hand, these cyclic loadings make critical impact on damage and durability of the whole system. Consequently, in the piezoelectric MEMS harvesters as the sustainable power supplies, besides the high energy conversion efficiency, a high degree of reliability and durability is essentially required.

To the best of our knowledge, thus far no study has been done to assess the fatigue damage of the micro-sized silicon-based piezoelectric harvesters. Thus, in this chapter we are further motivated to first investigate the effect of the physical aspects of the MEMS harvesters on the fatigue damage, and then propose a new mechanical geometry that can enlarge both energy

conversion efficiency and durability of the micro-sized harvesters. The major work in this chapter has been formally documented in multiple conference papers (as listed in the Appendix [Conference-5][Conference-6]).

7.2. Low-Resonant-Frequency Piezoelectric MEMS Harvester

The 3-D structural diagram of the proposed low-resonant-frequency MEMS vibration is illustrated in Fig. 64. This energy harvester comprises seven piezoelectric cantilevers, which are connected together by the proof masses. Thus, the overall device can be overviewed as a serpentine cantilever, which is clamped on two sides. In comparison to the conventional clamped-free piezoelectric cantilevers, the serpentine cantilever can increase the device deflection. Moreover, by using seven discrete proof masses, we can provide the uniform mass distribution along the harvester geometry. Consequently, with this structure lower mechanical stiffness and larger overall mass are attained. In the following section, the capability of the proposed structure in harnessing the vibration energy will be discussed.

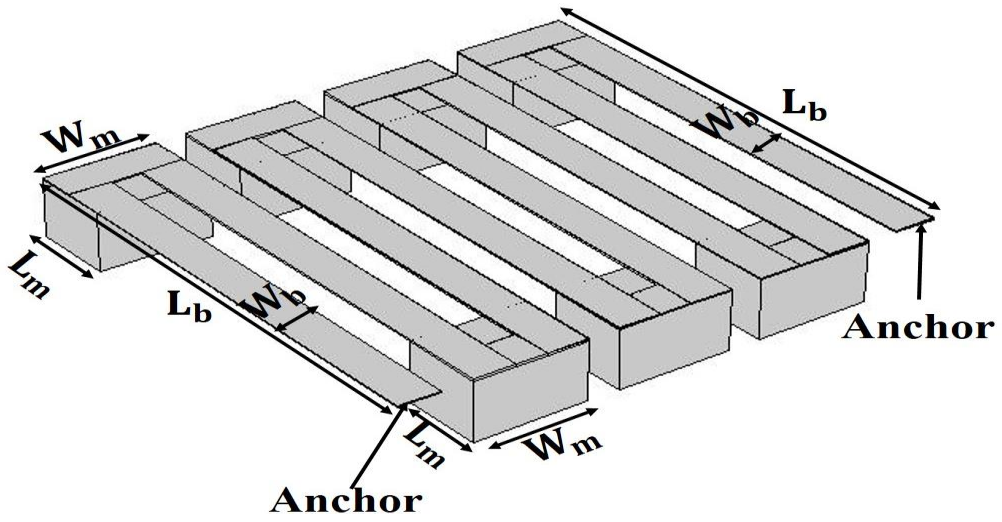

Fig. 64. Structural diagram of the proposed low-resonant-frequency piezoelectric MEMS energy harvester.

7.2.1. AI-Based Optimization Methodology

In order to obtain the optimum physical aspects of the proposed piezoelectric MEMS harvester in terms of resonant frequency and harvested voltage, the AI-based optimization method, where a deep neural network (DNN) is integrated with genetic algorithm (GA), has been developed. The working principle of the DNN on the decision making process is inspired by human brains. It is categorized as an artificial intelligence technique. In this study, the displayed DNN in Fig. 65 was implemented in MATLAB to minimize computation time of the optimization process. As shown in this figure, the utilized network consists of three different layers, namely, input, hidden and output layers. In the input layer four optimizable variables, i.e., L_b, w_b, L_m, w_m, as indicated in Fig. 65, can be imported to the network. The hidden layer, is comprised of seven sequential individual layers, which are made up of 60, 55, 45, 30, 20, 10 and 5 sigmoid neurons, respectively. Eventually, the output layer for reporting the amounts of both resonant frequency and harvested voltage is

formed with two neurons. At the first step, the constructed DNN was trained with 108 data sets, which were obtained by conducting the FEM simulations with COMSOL Multiphysics software.

Once the network was trained and its accuracy level was confirmed, the GA, which is an evolutionary computation method for optimizing complex problems [133], was integrated with the DNN. Therefore, the algorithm generates the random numbers for the input variables and their effects on the performance of the energy harvester in terms of resonant frequency and harvested voltage were evaluated within a few seconds. Finally, the GA selects those variables, which can provide both lower resonant frequency and higher amplitude of harvested voltage, as the optimal solutions.

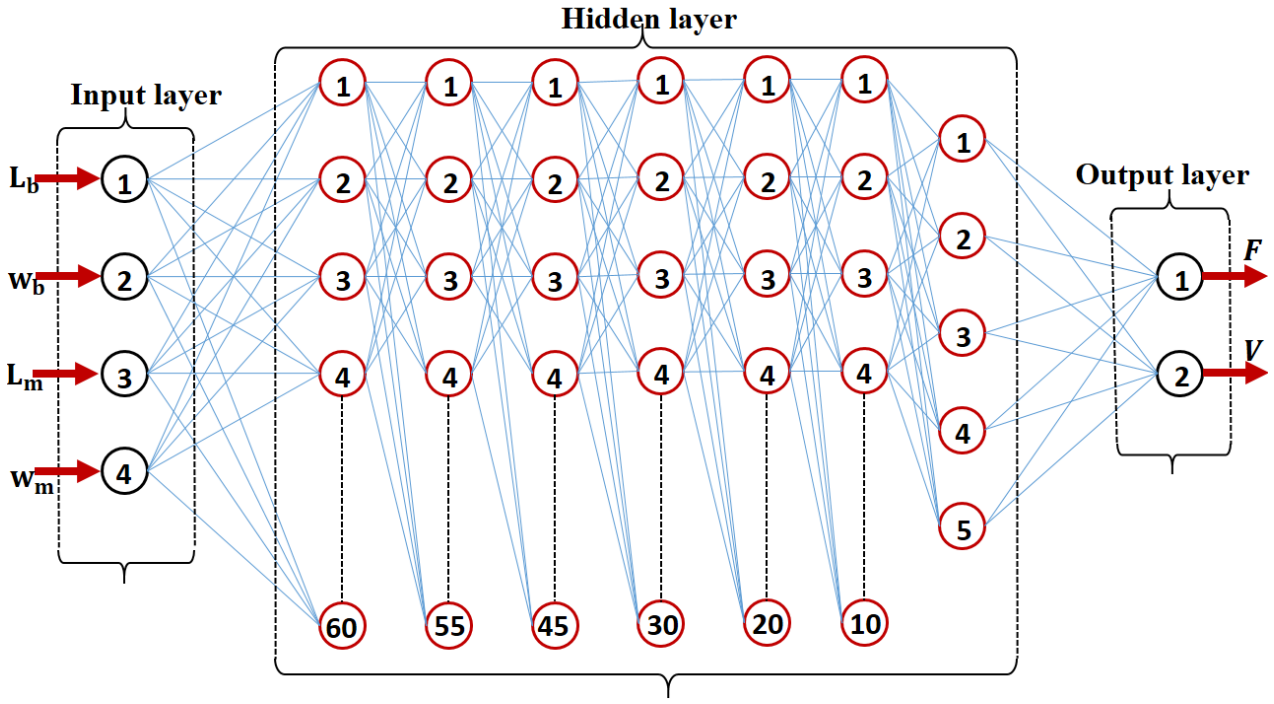

Fig. 65. Illustration of the utilized deep neural network (DNN) for estimating the performance of the proposed low-resonant-frequency piezoelectric MEMS energy harvester.

7.2.2. AI-Based Optimization Results

To demonstrate the effectiveness of the proposed AI-based optimization methodology, we defined an un-optimized structure, where the optimizable variables (i.e., L_b, w_b, L_m and w_m) were chosen to be the median values as per their allowed ranges. To improve the performance out of the un-optimized devices, our AI-based optimization method was executed with the population size of 20 and the generation number of 50 for the GA setup. Further information regarding the selection of these two user-defined factors can be found in Chapter 3 [164]. The obtained results for the un-optimized (*un-opt*) and optimized (*opt*) MEMS energy harvesters are listed in Table 18. In this table, the allowed ranges for the optimizable parameters, which are specified by their design rule constraints, are listed in the second rows. The computed resonant frequencies by the DNN and FEM simulations for the un-optimized and optimized structures are presented in the 6th and 7th columns, while the estimated harvested voltages by the DNN and FEM simulations are listed in the 8th and 9th columns, respectively.

Table 18. The physical dimensions of the un-optimized and optimized MEMS piezoelectric energy harvesters.

Parameter	**L_b [μm]**	**w_b [μm]**	**L_m [μm]**	**w_m [μm]**	**Freq. (DNN) [Hz]**	**Freq. (FEM) [HZ]**	**Voltage (DNN) [V]**	**Voltage (FEM) [V]**
Range	(1550,3050)	(150,250)	(500,1000)	(600,614)	-	-	-	-
un-opt	2300	200	750	607	162	169	2.7	2.5
opt	2945	216	907	609	105	110.5	3.5	3.25

From the summarized data in Table 18, it can be seen that the DNN can estimate both resonant frequency and harvested voltage with over 90% accuracy in reference to the FEM simulations. Therefore, by utilizing the DNN as a performance simulator, we can significantly reduce the required computation time dedicated to the FEM simulations. On the other hand, with the aid of this computation time reduction, a larger number of optimizable variables can be testified. Hence, the effectiveness of the optimization algorithm in entrapping the global optima can be further enhanced.

Frequency spectra of the un-optimized and optimized piezoelectric MEMS energy harvesters, which were computed by the FEM simulations under the excitation of 0.25g, are illustrated in Fig. 66. It is shown that the un-optimized device operates at 169Hz, while it can generate the maximum voltage of 2.5V. In contrast, by optimizing the harvester dimensions, its resonant frequency can be reduced to 110.5Hz, and its capability of the voltage harvesting can be considerably enlarged to 3.4V.

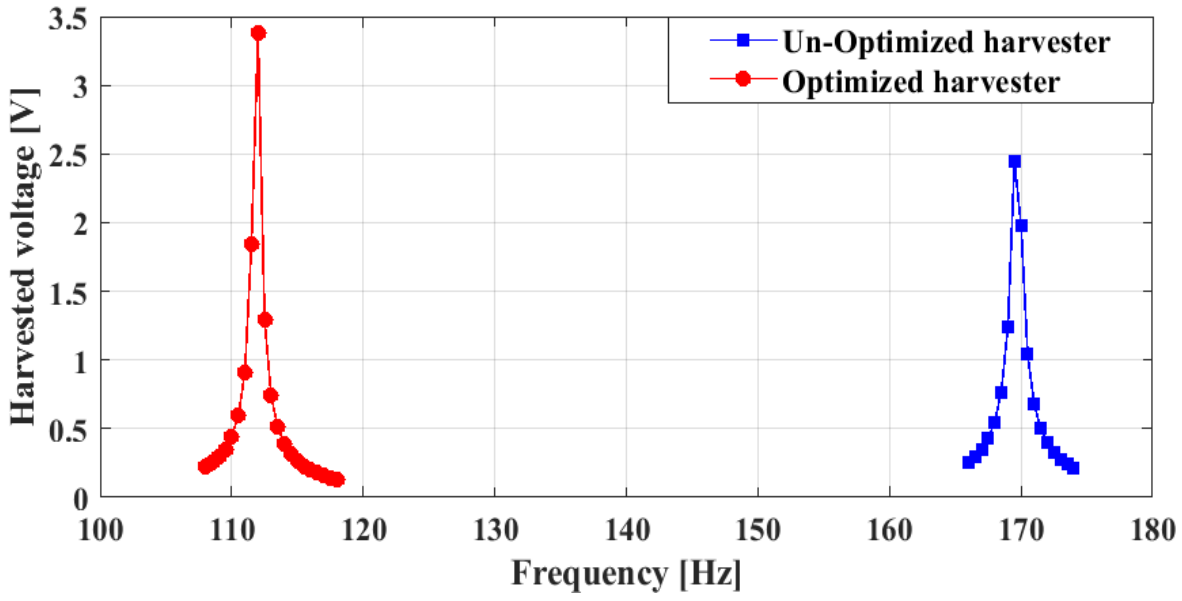

Fig. 66. Frequency spectra of the un-optimized and optimized low-resonant-frequency piezoelectric MEMS energy harvesters.

7.3. Fatigue Lifetime Analysis and Experimental Results

7.3.1. New Structure for Improving Fatigue Lifetime

In the mechanical devices, the life time (i.e., fatigue damage time) is proportional to the amplitude of stress. This relationship can be expressed by the Coffin-Manson equation as follows:

$$\sigma_a = \sigma_f' (2N_f)^b, \tag{61}$$

where σ_a is the stress amplitude, σ_f' is the fatigue strength coefficient, $2N_f$ is the number of reversals cycles to failure and b denotes the fatigue strength exponent. The fatigue strength coefficient and exponent (i.e., σ_f' and b) are dependent on materials properties. This means that amounts are basically constant for a particular material [204]. Consequently, to increase the number of reversal cycles to failure (i.e., N_f), the stress amplitude (i.e., σ_a) must be reduced by expanding the active area of the device.

In order to increase the active area of the MEMS harvester with the minimum impact on the device energy conversion efficiency, a new curve-shaped anchor is proposed. The structural diagram of our proposed MEMS energy harvester is illustrated in Fig. 67. As shown in this figure, the anchor area is expanded by a doubly clamped curve beam, while a straight beam with a tip mass is integrated to the centre of the anchor. In this structure the stress can be distributed uniformly along the whole anchor region. Therefore, the small stress concentration region, which causes damage fatigue, is considerably eliminated. Moreover, it is highly demanded that the MEMS harvester operates at lower frequencies. To this end, the second proof mass, for further

increasing the overall weight of the device, is attached to the centre of the curve-shaped anchor. In the following sections, the capability of the proposed geometry in energy harvesting will be discussed numerically and experimentally.

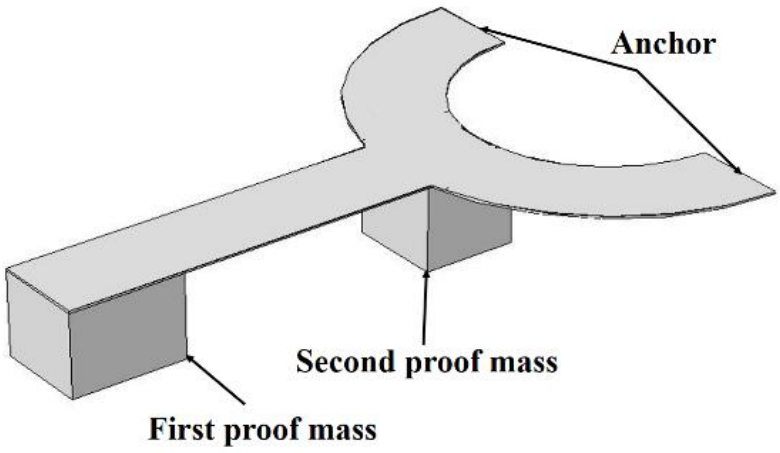

Fig. 67. Structural diagram of the proposed piezoelectric MEMS harvester with the curve-shaped anchor.

7.3.2. Fatigue Lifetime Analysis Results

As discussed in the previous section, the stress concentration in a small region causes damage fatigue. In the conventional MEMS cantilever-based energy harvesters, only the anchor part experiences a considerable amount of stress. For the comparison purpose, the stress distribution, as depicted in Fig. 68, between the conventional harvester geometry and our proposed curve-shaped anchor topology were simulated by COMSOL Multiphysics software (Version 5.2a). It can be seen that the stress is uniformly distributed in the whole area of the curve-shaped anchor. Thus, it is expected that this anchor area expanding by using the proposed curve-shaped anchor can increase the durability of the MEMS harvester.

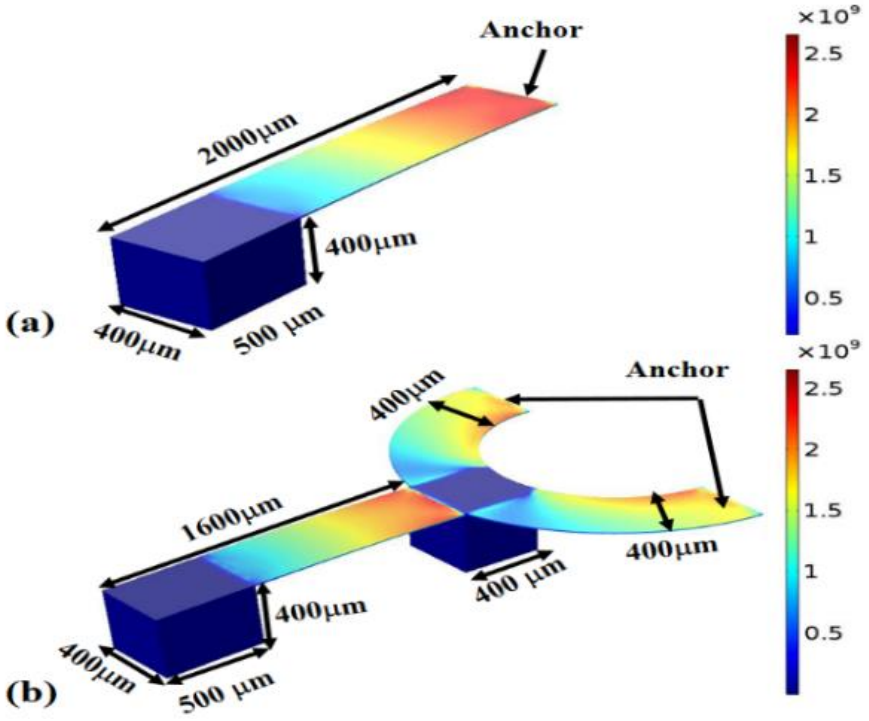

Fig. 68. Von-Mises stress distribution of (a) the conventional and (b) curve-shaped piezoelectric MEMS energy harvesters, respectively.

To examine the durability of the proposed MEMS harvester with the curve-shaped anchor, the fatigue test (i.e., Coffin-Manson approach) by COMSOL fatigue module [205] was performed. In this regard, the cyclic force with different amplitudes in the tip part of the device was applied. Moreover, the same experiment was conducted for the conventional MEMS harvester with the normal anchor shape. According to Fig. 69, it is obvious that the curve-shaped anchor harvester can work for a sufficiently large number of cycles ($>4*10^6$) under the excitation force of 9.4 mN, while the conventional harvester under this amount of force breaks at its anchor place (red slot in Fig. 69(a)). Thus, we can say the number of cycles to failure is zero for the curve-shaped anchor harvester.

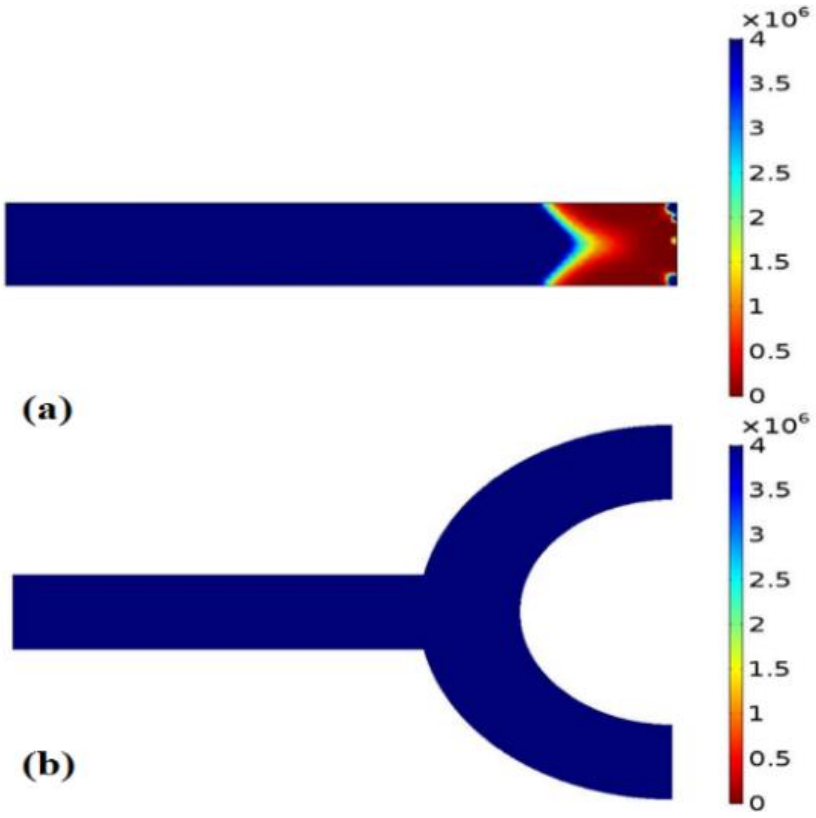

Fig. 69. Simulated fatigue lifetime distribution under cyclic mechanical loading with the amplitude of 9.5mN for (a) the conventional and (b) the curve-shaped piezoelectric MEMS energy harvesters, respectively.

To further investigate the mechanical behaviour of the proposed harvester, the cyclic loading of 10.5 mN, which exceeds the maximum device failure force, was applied. The obtained fatigue result is illustrate in Fig. 70. It is shown that under this excitation the initial cracks would be observed in the region sufficiently far away from the contact areas, while the curve-shaped anchor itself experiences no cracks or fractures. That is to say, unlike the conventional harvester geometry, the anchor is not the most fragile region any more that is subject to failure.

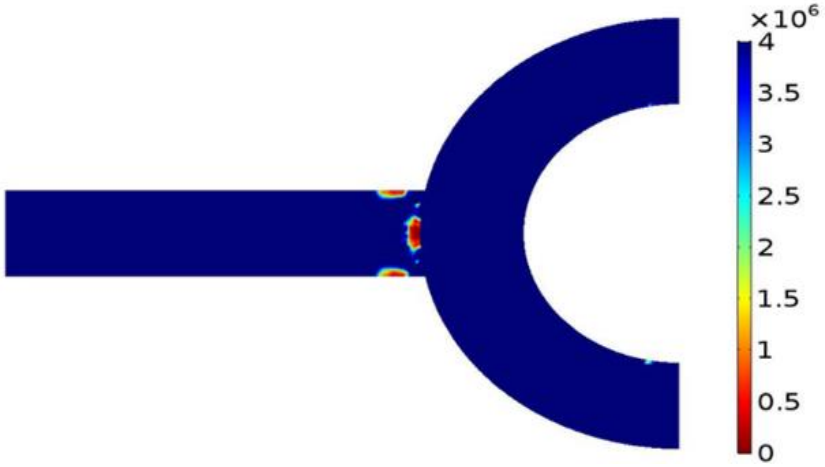

Fig. 70. Simulated fatigue lifetime distribution under cyclic mechanical loading with the amplitude of 10.5mN for the curve-shaped piezoelectric MEMS energy harvester, where the three cracks are observed in the region far away from the anchor places.

By using FEM simulations, the frequency responses of the demonstrated MEMS harvesters in Fig. 69 under the acceleration of 1g were computed and presented in Fig. 71. It can be seen that in the energy harvester with our proposed curve-shaped anchor the resonant frequency is reduced to 688 Hz. As a matter of fact, this reduction is highly desirable for the MEMS energy harvesters. Moreover, its capability in harvesting voltage is also considerably improved with reference to the conventional one.

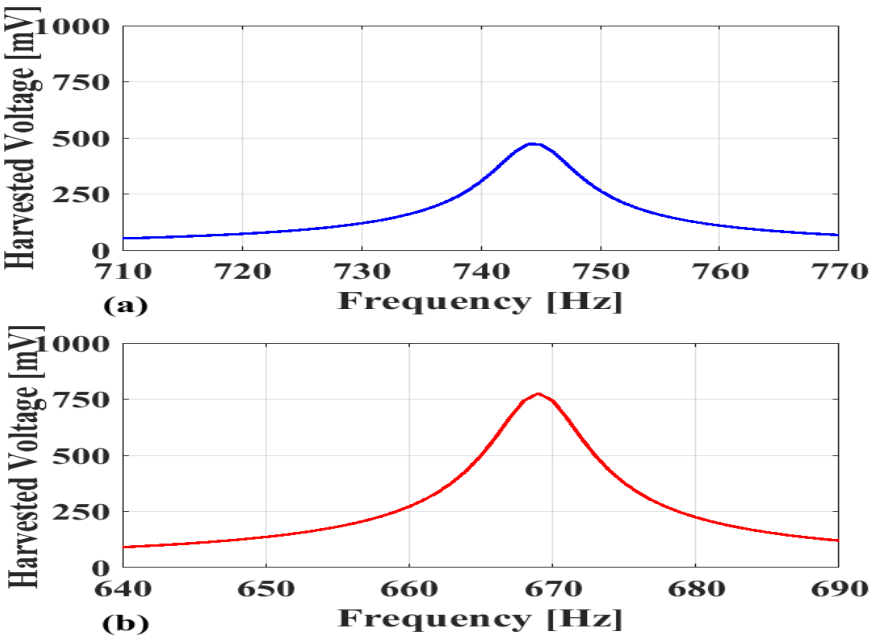

Fig. 71. Frequency responses of (a) the conventional and (b) the curve-shaped piezoelectric MEMS energy harvesters, respectively, under the acceleration magnitude of 1g.

To validate the correctness of the obtained results by the numerical simulations, as well as manufacturability of the proposed structures, the studied MEMS harvesters were fabricated by using the fabrication process explained in Section 3.4.1. The cross-section-view SEM image of the prototyped devices is shown in Fig. 72, and their performance measurements are listed in Table 19. A comprehensive comparison on the summarized data in this table shows that the curved-shape anchor can considerably improve the failure force and durability of the piezoelectric MEMS harvester. In addition, the harvested power can be improved by a factor of 2.66 in reference to the conventional geometry.

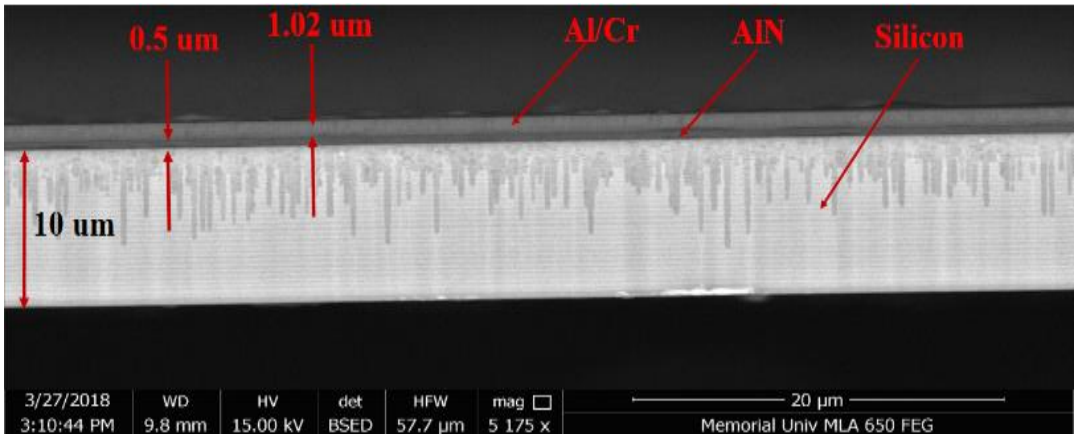

Fig. 72. The cross-section view SEM image of the fabricated MEMS harvesters for illustrating the layers arrangement.

Table 19. Summarized behaviour of the conventional and curve-shaped anchor piezoelectric MEMS harvesters.

Parameters	**Failure Force [mN]**	**Resonant Freq. [Hz]**	**Harvested Voltage [mV]**	**Matched Load [kΩ]**	**Harvested Power [µW]**
Conventional	7.3	743	473	288	0.77
Curved-Anchor	9.4	668	776	294	2.05

7.4. Summary

In this chapter, we proposed a low-resonant-frequency piezoelectric MEMS energy harvester. In order to optimize its performance, an AI optimization methodology based on DNN and GA was proposed. It is shown that the trained network could estimate the device performance with accuracy of over 90%. By taking advantage of this efficient AI-based performance estimator, the GA was able to reduce the device operational frequency from 169Hz to 110.5Hz and increase its energy conversion efficiency in terms of harvested voltage from 2.5V to 3.4V under 0.25g excitation.

In addition, we proposed a curve-shaped anchor structure for durability and efficiency improvement in the piezoelectric MEMS harvesters. The proposed harvester performance was studied numerically and experimentally. To demonstrate its high durability, the fatigue test under different cyclic loading was conducted. It is shown that in our proposed harvester the harvested power can be improved by a factor of 2.66 at the lower resonant frequency in comparison with the convention MEMS harvester.

Chapter 8 Conclusion

In this thesis, we first conducted a comprehensive survey on recent portable vibration-based wind energy harvesting devices. In the wind energy harvesters that are actually focused on how to harness vibration, the kinetic energy of vibration can be converted to electricity by using the following three techniques: piezoelectric-, electromagnetic- and electrostatic-based techniques. The functionality of the piezoelectric-based harvesters is dependent on the direct effect of piezoelectric materials, while in the electromagnetic-based harvesters magnetic field strength, which is provided by permanent magnets, plays a crucial role. The electrostatic-based harvesters, which require the external power supplies or electret materials, can be offered by utilizing capacitance variation. In addition, the required mechanical mechanisms for collecting the vibration from wind flow can be categorized into the rotational and aeroelastic mechanisms. The aeroelastic mechanism itself consists of two major groups, namely, vortex-induced vibrations and movement-induced vibrations. Furthermore, regarding their physical aspects, the portable wind energy harvesters are classified into macro-scale and micro-scale MEMS ones. Since the generated power amount is strongly dependent on the harvester size, the macro-scale energy harvesters can normally generate more power than the MEMS ones.

The current status of research and development exhibits that the aeroelastic mechanism is promising for the portable wind (i.e., vibration-based) energy harvesting systems, due to their simple structure and ease of fabrication. However, the rotational mechanism is highly effective for generating power from wind flow. One should not ignore that the aeroelastic mechanism can operate with high power conversion efficiency only if the direction of wind flow is perpendicular to the structures. Consequently, deploying some new symmetric structures seems to be necessary to provide omnidirectional functionality. The piezoelectric-based power generation technique

associated with micromachining fabrication technology can offer a wide range of vibration energy harvesters with high level of portability and appropriate output power.

The piezoelectric-based technique, thanks to the piezoelectric material deposition compatibility with the regular micromachining process and the independence from external voltage supply, has attracted more attention in producing the MEMS-based vibration energy harvesters. Therefore, in this thesis we have focused on the study of design and optimization methodologies for the MEMS-based vibration energy harvesters. In this regard, we proposed a GA-based design and optimization method for MEMS unimorph piezoelectric energy harvesters. In the first step, for estimating the generated voltage by the MEMS unimorph piezoelectric harvesters, the analytic models based on the Euler-Bernoulli beam theory was presented. The accuracy of the presented analytic models was validated numerically and experimentally by using COMSOL Multiphysics, and experimental measurement of our prototype devices, respectively. It is demonstrated that our proposed GA-based optimization methodology is able to enlarge energy harvesting efficiency by 31% in comparison with un-optimized harvesters. This improvement was observed with the overall device size reduction in multiple aspects, such as beam width and piezoelectric film length, which is highly desirable during the MEMS design process. Furthermore, a comprehensive comparison between our proposed optimization methodology and widely available commercial product (e.g., COMSOL optimization module) was shown that our GA-based optimization method is considerably more effective in both increasing the harvested voltage magnitude and reducing the required computation time. In addition, we studied impacts of the geometry optimization on mechanical and electrical properties of the harvester, such as resonant frequency, mass, stiffness, and internal impedance.

Furthermore, for simultaneously reducing resonant frequency and enhancing energy conversion of the piezoelectric MEMS energy harvesters, the analytic models to estimate the resonant frequency and harvested voltage for the unimorph MEMS piezoelectric harvesters with and without integration of a proof mass were presented. Their accuracy with reference to the FEM simulations and the experimental measurement from the prototyped harvesters were validated. Thanks to the observed high accuracy, they were utilized as the required objective fitness functions of our proposed GA-based optimization. To aim for multiple objectives, the GA, which is identified as an evolutionary computation method for optimizing complex problems, was executed to optimize the physical dimensions of the harvester, i.e., beam length, beam/piezoelectric width, piezoelectric length, and proof mass length (if existing). By using the micro-fabrication process, two different groups of piezoelectric MEMS harvesters, namely, un-optimized harvesters without any special considerations and optimized ones based on obtained results from the proposed optimization methodology were fabricated. It is found that the piezoelectric MEMS harvester with optimized geometry by the GA-based optimization methodology can generate the peak voltage of 1900 mV at the reduced resonant frequency of 425 Hz with the highest NVP of 163.8 in comparison with the previously proposed harvesters.

The most commonly utilized configuration for piezoelectric MEMS vibration energy harvesters is the unimorph cantilever-based one with integration of a proof mass at the tip part of the cantilever. Although such a simple structure can be fabricated by the general MEMS fabrication process, its energy conversion efficiency is relatively low since stress/strain can be only absorbed in a relatively small region (i.e., anchor region) during the device oscillation. Therefore, to provide more uniform stress distribution along the piezoelectric MEMS cantilever, in this thesis we proposed a T-shaped structure with two DOF, where both bending and torsional mode

frequencies can be located close to each other. The proposed structure was mathematically modeled and its analytic model of frequency response was validated by FEM simulations and prototype measurements. It was demonstrated that our proposed T-shaped piezoelectric cantilever structure can help distribute mechanical stress in broader areas with higher magnitude and lower resonant frequency in comparison with the conventional straight-cantilever configuration.

Typically the conventional piezoelectric MEMS energy harvesters have a very narrow operational frequency bandwidth. To increase the operational frequency of piezoelectric MEMS harvesters, we further developed and optimized a structure with the capability of multiple-degrees-of-freedom (MDOF). The proposed structure is anchored on two sides. To increase its total deflection, a set of piezoelectric cantilevers with a serpentine shape associated with three discrete proof masses at different locations is used. Thus, this unique geometry provides uniform mass distribution in the entire device. The behaviors of the proposed structure were studied by using modal analysis and mechanical stiffness computation. It is demonstrated that the harvester can oscillate in the multiple modes with a strong nonlinear behavior at its second mode frequency. Since the proposed harvester is highly nonlinear (due to its MDOF), accurate estimation of its performance is almost impossible. As a result, to save human designs efforts, we used a GA-based optimization method. The optimization result was verified by FEM-based simulations and measurement of the prototyped MEMS harvester. A performance comparison between the proposed MEMS harvester and the recently published vibration energy harvesters from the literature shows that our proposed harvester is well superior to offer a promising vibration energy harvesting system for being deployed in the real environment.

In order to speed up the optimization process of the unimorph piezoelectric MEMS harvesters, we also proposed an AI optimization method based on DNN. In this way, a neural network with

the configuration of 4 inputs, 7 hidden layers, and 2 outputs was utilized as a performance simulator of the MEMS harvester. Firstly, this implemented network was trained by 108 data sets, which were obtained by conducting the FEM simulations. After that, the accuracy of the trained network in estimating the harvested voltage and resonant frequency for a given size of MEMS harvesters was examined. It was found that the trained network can estimate the device performance with accuracy of over 90% with reference to the FEM simulations. By taking advantage of this highly efficient AI-based performance estimator, the GA optimization was performed with the aim of increasing the harvested voltage efficiency and reducing the operational frequency for a piezoelectric MEMS vibration harvester. It is numerically shown that our proposed AI-based optimization methodology is able to reduce the device operational frequency from 169Hz to 110.5Hz and increase its energy conversion efficiency in terms of harvested voltage from 2.5V to 3.4V under 0.25g excitation with reference to the un-optimized one.

Finally in this thesis we also studied the lifetime of the piezoelectric MEMS harvesters, as an important parameter for the energy harvesting systems. To improve the durability and energy conversion efficiency of the piezoelectric MEMS harvesters, we proposed a new curve-shaped anchoring scheme. This proposed structure is comprised of a doubly clamped curve beam with a mass at its center as an anchor, and an attached straight beam with the tip mass to the center of this anchor. To assess the fatigue damage, which is actually critical to the micro-sized silicon-based piezoelectric harvesters, we used the Coffin-Manson method and FEM to comprehensively study the fatigue lifetime of the proposed geometry. Our proposed piezoelectric MEMS harvester was fabricated and its capability in harnessing the vibration energy was examined numerically and experimentally. It was found that the harvested energy can be enlarged by a factor of 2.66, while this improvement is attained by the resonant frequency reduction and failure force magnitude

enlargement, in comparison with the conventional geometry of the regular piezoelectric MEMS harvesters.

Chapter 9 Future Work

In this thesis we have mainly focused on design and optimization of mechanical structures in the unimorph piezoelectric harvesters, which are identified as the core of energy harvesting systems. In order to deploy the MEMS harvesters in the real environment, a special package needs to be considered. In the future research work, according to the harvester operational medium, a unique surrounding frame should be designed to protect the harvester from any environmental changes. It is highly desirable that the utilized packaging solutions have the minimum impacts on the performance (i.e., energy conversion efficiency and operation frequency) of the energy harvesting systems as well as the overall size of the device. Furthermore, enhancing the MEMS harvester lifetime by using its package is another subject that should be taken into account. One way to do this is to use air damping as a soft spring. In this regard, the MEMS harvester will be placed within a cavity. Thus, air will be readily accumulated inside the cavity. Then the moveable part of harvester cannot oscillate largely, which means the device deflection is limited to a certain level. By using this method, the harvester under large amplitude of acceleration (i.e., shock) will be able to survive.

The electrode coverage of piezoelectric cantilevers plays an important role in the amount of the extracted power from the energy harvesting system. In this thesis, the electrode coverage is not considered in analytic modeling and our optimization methodologies. However, our presented analytic equations can be further expanded by taking into account of the electrode size. Then the electrode coverage can be considered as an optimizable variable for enhancing the energy conversion efficiency and reducing the operational frequency of the piezoelectric MEMS harvesters.

The quality factor is a crucial metric that describes the energy losses of the underdamped resonant elements, such as energy harvesting systems. This parameter is dependent on both bandwidth and center frequency of the resonators. In order to further enhance the capability of the piezoelectric MEMS energy harvesters, the quality factor can be considered as another objective function for optimization methodology. To reach this objective, we need to investigate the analytic modeling of the quality factor for the MEMS unimorph piezoelectric energy harvesters. Moreover, we should develop more advanced evolutionary algorithms for the purpose of multi-objective optimization.

It is highly demanded that the overall size of the piezoelectric MEMS energy harvesting system remains as small as possible, while it is integrated with the power management system. The proposed and investigated power management system in this thesis was implemented by using off-the-shelf discrete components, whose physical size is relatively big. Consequently, to miniaturize our proposed power management system, we can use CMOS or other technologies to integrate the required MOSFET, JFET, microcontroller, etc., into one IC (integrated circuit). It is worth pointing out that to further reduce the size of the energy harvesters and diminish the complexity of the electrical routing, the patterns of the electrical and mechanical parts can be exposed on the same silicon wafer during the micro-fabrication process. Under such an integration, the tiny piezoelectric vibration energy harvesting systems with the capability of signal processing and energy storage will be produced.

References

[1] M. Rasouli and L. S. J. Phee, "Energy sources and their development for application in medical devices," *Expert Rev. Med. Devices*, vol. 7, no. 5, pp. 693–709, 2010.

[2] S. Nabavi, G. Yaralioglu, "High Quality Factor Resonant Mass Sensors Based on CMUT for Immersion in Liquid," in *14th international workshop on Micromachined Ultrasonic Transducers (MUT)*, 2015.

[3] P. D. Mitcheson, E. M. Yeatman, G. K. Rao, A. S. Holmes, and T. C. Green, "Energy harvesting from human and machine motion for wireless electronic devices," in *Proc. IEEE*, vol. 96, no. 9, pp. 1457–1486, 2008.

[4] S. R. Anton and D. J. Inman, "Vibration energy harvesting for unmanned aerial vehicles," in *Proc. The 15th International Symposium on: Smart Structures and Materials & Nondestructive Evaluation and Health Monitoring*, 2008, p. 692824.

[5] S. P. Beeby, M. J. Tudor, and N. M. White, "Energy harvesting vibration sources for microsystems applications," *Meas. Sci. Technol.*, vol. 17, no. 12, p. R175, 2006.

[6] C. C. Enz, A. El-Hoiydi, J.-D. Decotignie, and V. Peiris, "WiseNET: an ultralow-power wireless sensor network solution," *Computer (Long. Beach. Calif).*, vol. 37, no. 8, pp. 62–70, 2004.

[7] G. T. A. Kovacs, N. I. Maluf, and K. E. Petersen, "Bulk micromachining of silicon," in *Proc. IEEE*, vol. 86, no. 8, pp. 1536–1551, 1998.

[8] J. M. Bustillo, R. T. Howe, and R. S. Muller, "Surface micromachining for microelectromechanical systems," in *Proc. IEEE*, vol. 86, no. 8, pp. 1552–1574, 1998.

[9] E. Becker, W. Ehrfeld, P. Hagmann, A. Maner, and D. Münchmeyer, "Fabrication of microstructures with high aspect ratios and great structural heights by synchrotron radiation lithography, galvanoforming, and plastic moulding (LIGA process)," *Microelectron. Eng.*, vol. 4, no. 1, pp. 35–56, 1986.

[10] L. Zhang, N. Jangkrajarng, S. Bhattacharya, and C. J. R. Shi, "Parasitic-aware optimization and retargeting of analog layouts: A symbolic-template approach," *Comput. Des. Integr. Circuits Syst. IEEE Trans.*, vol. 27, no. 5, pp. 791–802, 2008.

[11] A. A. I. Ahmed and L. Zhang, "Fast parasitic-aware synthesis methodology for high-performance analog circuits," in *Proc. IEEE International Symposium on Circuits and Systems (ISCAS)*, 2012, pp. 2155–2158.

[12] C.-M. Ho and Y.-C. Tai, "Micro-electro-mechanical-systems (MEMS) and fluid flows," *Annu. Rev. Fluid Mech.*, vol. 30, no. 1, pp. 579–612, 1998.

[13] R. W. Miles, K. M. Hynes, and I. Forbes, "Photovoltaic solar cells: An overview of state-of-the-art cell development and environmental issues," *Prog. Cryst. Growth Charact. Mater.*, vol. 51, no. 1, pp. 1–42, 2005.

[14] J. Simon and T. Caroff, "Device for generating current and/or voltage based on a thermoelectric module placed in a flowing fluid." Google Patents, 2015.

[15] J. Chen, Z. Yan, and L. Wu, "The influence of Thomson effect on the maximum power output and maximum efficiency of a thermoelectric generator," *J. Appl. Phys.*, vol. 79, no. 11, pp. 8823–8828, 1996.

[16] A. Baranov, D. Spirjakin, S. Akbari, and A. Somov, "Optimization of power consumption for gas sensor nodes: A survey," *Sensors Actuators A Phys.*, vol. 233, pp. 279–289, 2015.

[17] M. Al Ahmad, "Piezoelectric water drop energy harvesting," *J. Electron. Mater.*, vol. 43, no. 2, pp. 452–458, 2014.

[18] S. Roundy and P. K. Wright, "A piezoelectric vibration based generator for wireless electronics," *Smart Mater. Struct.*, vol. 13, no. 5, pp. 1131, 2004.

[19] A. R. Jha, *Wind turbine technology*. CRC press, 2010.

[20] C. Zhang, X.-F. He, S.-Y. Li, Y.-Q. Cheng, and Y. Rao, "A wind energy powered wireless temperature sensor node," *Sensors*, vol. 15, no. 3, pp. 5020–5031, 2015.

[21] R. Song, X. Shan, F. Lv, and T. Xie, "A study of vortex-induced energy harvesting from water using PZT piezoelectric cantilever with cylindrical extension," *Ceram. Int.*, vol. 41, pp. 768-773, 2015.

[22] H. Zhang *et al.*, "A flexible and implantable piezoelectric generator harvesting energy from the pulsation of ascending aorta: in vitro and in vivo studies," *Nano Energy*, vol. 12, pp. 296–304, 2015.

[23] A. Moure *et al.*, "Feasible integration in asphalt of piezoelectric cymbals for vibration energy harvesting," *Energy Convers. Manag.*, vol. 112, pp. 246–253, 2016.

[24] Q. Zhang and E. S. Kim, "Microfabricated Electromagnetic Energy Harvesters With Magnet and Coil Arrays Suspended by Silicon Springs," *IEEE Sens. J.*, vol. 16, no. 3, pp. 634–641, 2016.

[25] Y. Zhu, S. O. R. Moheimani, and M. R. Yuce, "A 2-DOF MEMS ultrasonic energy harvester," *IEEE Sens. J*, vol. 11, no. 1, pp. 155–161, 2011.

[26] M. Perez, S. Boisseau, P. Gasnier, J. Willemin, M. Geisler, and J. L. Reboud, "A cm scale electret-based electrostatic wind turbine for low-speed energy harvesting applications," *Smart Mater. Struct.*, vol. 25, no. 4, pp. 45015, 2016.

[27] A. Rivadeneyra *et al.*, "Tunable MEMS piezoelectric energy harvesting device," *Microsyst. Technol.*, vol. 22, no. 4, pp. 823–830, 2016.

[28] S. Saxena, R. Sharma, and B. D. Pant, "Design and development of guided four beam cantilever type MEMS based piezoelectric energy harvester," *Microsyst. Technol.*, pp. 1–9, 2016.

[29] H. Liu, S. Zhang, T. Kobayashi, T. Chen, and C. Lee, "Flow sensing and energy harvesting

characteristics of a wind-driven piezoelectric Pb (Zr0. 52, Ti0. 48) O 3 microcantilever," *Micro Nano Lett. IET*, vol. 9, no. 4, pp. 286–289, 2014.

[30] C. B. Carroll, "Energy harvesting eel." Google Patents, 2002.

[31] A. Betz and D. N. From, "Windmills in the Light of Modern Research," *Naturwissenschaften*, vol. 15, no. 46, 1927.

[32] R. Xu and S. G. Kim, "Figures of merits of piezoelectric materials in energy harvesters," in *Proc. POWER MEMS*, 2012.

[33] E. E. Aktakka, R. L. Peterson, and K. Najafi, "Thinned-PZT on SOI process and design optimization for piezoelectric inertial energy harvesting," in *Proc. Solid-State Sensors, Actuators and Microsystems Conference (TRANSDUCERS)*, 2011, pp. 1649–1652.

[34] A. S. Holmes, "Micro Energy Harvesting," in *Micro Energy Harvesting*, J. Briand, D., Yeatman, E., Roundy, S., & Troccaz, Ed. 2015.

[35] B. Yang *et al.*, "Electromagnetic energy harvesting from vibrations of multiple frequencies," *J. Micromechanics Microengineering*, vol. 19, no. 3, pp. 35001, 2009.

[36] S. Meninger, J. O. Mur-Miranda, R. Amirtharajah, A. P. Chandrakasan, and J. H. Lang, "Vibration-to-electric energy conversion," *Very Large Scale Integr. Syst. IEEE Trans.*, vol. 9, no. 1, pp. 64–76, 2001.

[37] G. Shomalnasab and L. Zhang, "New Analytic Model of Coupling and Substrate Capacitance in Nanometer Technologies," *Very Large Scale Integr. Syst. IEEE Trans.*, vol. 23, no. 7, pp. 1268–1280, 2015.

[38] A. Erturk and D. J. Inman, *Piezoelectric energy harvesting*. John Wiley & Sons, 2011.

[39] D. Spreemann and Y. Manoli, *Electromagnetic vibration energy harvesting devices: Architectures, design, modeling and optimization*, vol. 35. Springer Science & Business Media, 2012.

[40] E. Arroyo, A. Badel, F. Formosa, Y. Wu, and J. Qiu, "Comparison of electromagnetic and piezoelectric vibration energy harvesters: model and experiments," *Sensors Actuators A Phys.*, vol. 183, pp. 148–156, 2012.

[41] P. Basset, E. Blokhina, and D. Galayko, *Electrostatic Kinetic Energy Harvesting*. John Wiley & Sons, 2016.

[42] A. D. T. Elliott, L. M. Miller, E. Halvorsen, P. K. Wright, and P. D. Mitcheson, "Which is better, electrostatic or piezoelectric energy harvesting systems?," in *Journal of Physics: Conference Series*, 2015, vol. 660, no. 1, p. 12128.

[43] T. Sulchek *et al.*, "Parallel atomic force microscopy with optical interferometric detection," *Appl. Phys. Lett.*, vol. 78, no. 12, pp. 1787–1789, 2001.

[44] J. Ajitsaria, S.-Y. Choe, D. Shen, and D. J. Kim, "Modeling and analysis of a bimorph piezoelectric cantilever beam for voltage generation," *Smart Mater. Struct.*, vol. 16, no. 2,

pp. 447, 2007.

[45] G. Yaralioglu, "Ultrasonic heating and temperature measurement in microfluidic channels," *Sensors Actuators A Phys.*, vol. 170, no. 1, pp. 1–7, 2011.

[46] M. E. Levinshtein, S. L. Rumyantsev, and M. S. Shur, *Properties of Advanced Semiconductor Materials: GaN, AIN, InN, BN, SiC, SiGe*. John Wiley & Sons, 2001.

[47] B. S. Lee, S. C. Lin, W. J. Wu, X. Y. Wang, P. Z. Chang, and C. K. Lee, "Piezoelectric MEMS generators fabricated with an aerosol deposition PZT thin film," *J. Micromechanics Microengineering*, vol. 19, no. 6, p. 65014, 2009.

[48] H. Bardaweel, O. Al Hattamleh, R. Richards, D. Bahr, and C. Richards, "A Comparison of piezoelectric materials for MEMS power generation," in *Proc. the 6th international workshop on micro and nanotechnology for power generation and energy conversion applications*, 2006.

[49] S.-D. Kwon, "A T-shaped piezoelectric cantilever for fluid energy harvesting," *Appl. Phys. Lett.*, vol. 97, no. 16, p. 164102, 2010.

[50] M. Renaud, P. Fiorini, R. van Schaijk, and C. Van Hoof, "Harvesting energy from the motion of human limbs: the design and analysis of an impact-based piezoelectric generator," *Smart Mater. Struct.*, vol. 18, no. 3, pp. 35001, 2009.

[51] G. Poulin, E. Sarraute, and F. Costa, "Generation of electrical energy for portable devices: Comparative study of an electromagnetic and a piezoelectric system," *Sensors Actuators A Phys.*, vol. 116, no. 3, pp. 461–471, 2004.

[52] P. J. Schubel and R. J. Crossley, "Wind turbine blade design," *Energies*, vol. 5, no. 9, pp. 3425–3449, 2012.

[53] R. Xu *et al.*, "Screen printed PZT/PZT thick film bimorph MEMS cantilever device for vibration energy harvesting," *Sensors Actuators A Phys.*, vol. 188, pp. 383–388, 2012.

[54] Z. Wen, L. Deng, X. Zhao, Z. Shang, C. Yuan, and Y. She, "Improving voltage output with PZT beam array for MEMS-based vibration energy harvester: theory and experiment," *Microsyst. Technol.*, vol. 21, no. 2, pp. 331–339, 2015.

[55] M. Norhisam, A. Norrimah, R. Wagiran, R. M. Sidek, N. Mariun, and H. Wakiwaka, "Consideration of theoretical equation for output voltage of linear displacement sensor using meander coil and pattern guide," *Sensors Actuators A Phys.*, vol. 147, no. 2, pp. 470–473, 2008.

[56] S. Cheng, N. Wang, and D. P. Arnold, "Modeling of magnetic vibrational energy harvesters using equivalent circuit representations," *J. Micromechanics Microengineering*, vol. 17, no. 11, p. 2328, 2007.

[57] M. A. Weimer, R. Zane, and others, "Remote area wind energy harvesting for low-power autonomous sensors," in *Proc. IEEE Power Electronics Specialists Conference*, 2006, pp. 1–5.

[58] S.-H. Kim *et al.*, "An electromagnetic energy scavenger from direct airflow," *J. Micromechanics Microengineering*, vol. 19, no. 9, pp. 94010, 2009.

[59] H.-J. Jung, I.-H. Kim, and S.-J. Jang, "An energy harvesting system using the wind-induced vibration of a stay cable for powering a wireless sensor node," *Smart Mater. Struct.*, vol. 20, no. 7, p. 75001, 2011.

[60] F. Wang and O. Hansen, "Electrostatic energy harvesting device with out-of-the-plane gap closing scheme," *Sensors Actuators A Phys.*, vol. 211, pp. 131–137, 2014.

[61] S. Boisseau, G. Despesse, and B. A. Seddik, "Electrostatic conversion for vibration energy harvesting," *arXiv Prepr.*, 2012.

[62] S. Boisseau, G. Despesse, T. Ricart, E. Defay, and A. Sylvestre, "Cantilever-based electret energy harvesters," *Smart Mater. Struct.*, vol. 20, no. 10, pp. 105013, 2011.

[63] M. Perez, S. Boisseau, P. Gasnier, J. Willemin, and J. L. Reboud, "An electret-based aeroelastic flutter energy harvester," *Smart Mater. Struct.*, vol. 24, no. 3, p. 35004, 2015.

[64] J. M. Jonkman, S. Butterfield, W. Musial, and G. Scott, *Definition of a 5-MW reference wind turbine for offshore system development*. National Renewable Energy Laboratory Golden, CO, 2009.

[65] D. A. Howey, A. Bansal, and A. S. Holmes, "Design and performance of a centimetre-scale shrouded wind turbine for energy harvesting," *Smart Mater. Struct.*, vol. 20, no. 8, pp. 85021, 2011.

[66] S. Priya, C.-T. Chen, D. Fye, and J. Zahnd, "Piezoelectric windmill: a novel solution to remote sensing," *Jpn. J. Appl. Phys.*, vol. 44, no. 1L, pp. L104, 2005.

[67] Y. Yang, Q. Shen, J. Jin, Y. Wang, W. Qian, and D. Yuan, "Rotational piezoelectric wind energy harvesting using impact-induced resonance," *Appl. Phys. Lett.*, vol. 105, no. 5, pp. 53901, 2014.

[68] A. Bibo, "Investigation of Concurrent Energy Harvesting from Ambient Vibrations and Wind," 2014.

[69] A. Deivasigamani, J. M. McCarthy, S. John, S. Watkins, P. Trivailo, and F. Coman, "Piezoelectric energy harvesting from wind using coupled bending-torsional vibrations," *Mod. Appl. Sci.*, vol. 8, no. 4, pp. 106, 2014.

[70] J. M. McCarthy, S. Watkins, A. Deivasigamani, and S. J. John, "Fluttering energy harvesters in the wind: A review," *J. Sound Vib.*, vol. 361, pp. 355–377, 2016.

[71] A. Abdelkefi, "Aeroelastic energy harvesting: A review," *Int. J. Eng. Sci.*, vol. 100, pp. 112–135, 2016.

[72] D. Zhu, S. Beeby, J. Tudor, N. White, and N. Harris, "A novel miniature wind generator for wireless sensing applications," in Proc. *IEEE Sensors*, 2010, pp. 1415–1418.

[73] M. Zhang and J. Wang, "Experimental Study on Piezoelectric Energy Harvesting from

Vortex-Induced Vibrations and Wake-Induced Vibrations," *J. Sensors*, vol. 2016, 2016.

[74] H. L. Dai, A. Abdelkefi, Y. Yang, and L. Wang, "Orientation of bluff body for designing efficient energy harvesters from vortex-induced vibrations," *Appl. Phys. Lett.*, vol. 108, no. 5, pp. 53902, 2016.

[75] M. Argentina and L. Mahadevan, "Fluid-flow-induced flutter of a flag," *Proc. Natl. Acad. Sci. U. S. A.*, vol. 102, no. 6, pp. 1829–1834, 2005.

[76] A. Bibo and M. F. Daqaq, "Investigation of concurrent energy harvesting from ambient vibrations and wind using a single piezoelectric generator," *Appl. Phys. Lett.*, vol. 102, no. 24, pp. 243904, 2013.

[77] T. W. Strganac, J. Ko, and D. E. Thompson, "Identification and control of limit cycle oscillations in aeroelastic systems," *J. Guid. Control. Dyn.*, vol. 23, no. 6, pp. 1127–1133, 2000.

[78] A. Abdelkefi, M. R. Hajj, and A. H. Nayfeh, "Piezoelectric energy harvesting from transverse galloping of bluff bodies," *Smart Mater. Struct.*, vol. 22, no. 1, pp. 15014, 2012.

[79] J. Sirohi and R. Mahadik, "Harvesting wind energy using a galloping piezoelectric beam," *J. Vib. Acoust.*, vol. 134, no. 1, p. 11009, 2012.

[80] S. Li, J. Yuan, and H. Lipson, "Ambient wind energy harvesting using cross-flow fluttering," *J. Appl. Phys.*, vol. 109, no. 2, p. 26104, 2011.

[81] S. Li and H. Lipson, "Vertical-stalk flapping-leaf generator for wind energy harvesting," in *Proc. ASME Conference on Smart Materials, Adaptive Structures and Intelligent Systems*, 2009, pp. 611–619.

[82] R. Violette, E. De Langre, and J. Szydlowski, "Computation of vortex-induced vibrations of long structures using a wake oscillator model: comparison with DNS and experiments," *Comput. Struct.*, vol. 85, no. 11, pp. 1134–1141, 2007.

[83] H. L. Dai, A. Abdelkefi, and L. Wang, "Vortex-induced vibrations mitigation through a nonlinear energy sink," *Commun. Nonlinear Sci. Numer. Simul.*, vol. 42, pp. 22–36, 2017.

[84] H. Abdelmoula and A. Abdelkefi, "The potential of electrical impedance on the performance of galloping systems for energy harvesting and control applications," *J. Sound Vib.*, vol. 370, pp. 191–208, 2016.

[85] J. Zhao *et al.*, "An arc-shaped piezoelectric generator for multi-directional wind energy harvesting," *Sensors Actuators A Phys.*, vol. 236, pp. 173–179, 2015.

[86] J.-K. Park, K.-M. Kim, S.-D. Kwon, and K. H. Law, "An aero-elastic flutter based electromagnetic energy harvester with wind speed augmenting funnel,", in *Proc. International Conference on Advances in Wind and Structures*, 2012.

[87] F. Fei, J. D. Mai, and W. J. Li, "A wind-flutter energy converter for powering wireless sensors," *Sensors Actuators A Phys.*, vol. 173, no. 1, pp. 163–171, 2012.

[88] S. P. Matova, R. Elfrink, R. J. M. Vullers, and R. Van Schaijk, "Harvesting energy from airflow with a michromachined piezoelectric harvester inside a Helmholtz resonator," *J. Micromechanics Microengineering*, vol. 21, no. 10, p. 104001, 2011.

[89] D. Zhu, S. P. Beeby, M. J. Tudor, N. M. White, and N. R. Harris, "Novel miniature airflow energy harvester for wireless sensing applications in buildings," *Sensors Journal, IEEE*, vol. 13, no. 2, pp. 691–700, 2013.

[90] J. Sirohi and R. Mahadik, "Piezoelectric wind energy harvester for low-power sensors," *J. Intell. Mater. Syst. Struct.*, 2011.

[91] D. Ramasur and G. P. Hancke, "A wind energy harvester for low power wireless sensor networks," in *Proc. IEEE Instrumentation and Measurement Technology Conference (I2MTC)*, 2012, pp. 2623–2627.

[92] F. J. Xu, F.-G. Yuan, J. Z. Hu, and Y. P. Qiu, "Design of a miniature wind turbine for powering wireless sensors," in *SPIE Smart Structures and Materials+ Nondestructive Evaluation and Health Monitoring*, 2010, p. 764741.

[93] Y. K. Tan and S. K. Panda, "A novel piezoelectric based wind energy harvester for low-power autonomous wind speed sensor," in *Proc. IEEE Industrial Electronics Society*, 2007, pp. 2175–2180.

[94] Y. Yang, L. Zhao, and L. Tang, "Comparative study of tip cross-sections for efficient galloping energy harvesting," *Appl. Phys. Lett.*, vol. 102, no. 6, pp. 6–10, 2013.

[95] L. Zhao, L. Tang, and Y. Yang, "Comparison of modeling methods and parametric study for a piezoelectric wind energy harvester," *Smart Mater. Struct.*, vol. 22, no. 12, p. 125003, 2013.

[96] A. Abdelkefi, J. M. Scanlon, E. McDowell, and M. R. Hajj, "Performance enhancement of piezoelectric energy harvesters from wake galloping," *Appl. Phys. Lett.*, vol. 103, no. 3, p. 33903, 2013.

[97] A. H. Alhadidi, A. Bibo, and M. F. Daqaq, "Flow Energy Harvesters With a Nonlinear Restoring Force," in *Proc. ASME 2014 Conference on Smart Materials, Adaptive Structures and Intelligent Systems*, 2014

[98] M. Bryant and E. Garcia, "Modeling and testing of a novel aeroelastic flutter energy harvester," *J. Vib. Acoust.*, vol. 133, no. 1, p. 11010, 2011.

[99] R. R. Mahadik and J. Sirohi, "Harvesting Wind Energy Using a Galloping Piezoelectric Beam," in *Proc. ASME Conference on Smart Materials, Adaptive Structures and Intelligent Systems*, 2009, pp. 443–450.

[100] D. Pimentel, P. Musilek, A. Knight, and J. Heckenbergerova, "Characterization of a wind flutter generator," in *Proc. Environment and Electrical Engineering (EEEIC)*, 2010, pp. 81–84.

[101] L. Zhang, V. Masek, and N. N. Sanatdoost, "Structural optimization of Z-axis tuning-fork

MEMS gyroscopes for enhancing reliability and resolution," *Microsyst. Technol.*, vol. 21, no. 6, pp. 1187–1201, 2015.

[102] I. Sari, T. Balkan, and H. Kulah, "An electromagnetic micro power generator for wideband environmental vibrations," *Sensors Actuators A Phys.*, vol. 145, pp. 405–413, 2008.

[103] J. C. Park, D. H. Bang, and J. Y. Park, "Micro-fabricated electromagnetic power generator to scavenge low ambient vibration," *Magn. IEEE Trans.*, vol. 46, no. 6, pp. 1937–1942, 2010.

[104] D. Rancourt, A. Tabesh, and L. G. Fréchette, "Evaluation of centimeter-scale micro windmills: aerodynamics and electromagnetic power generation," in *Proc. PowerMEMS*, vol. 20079, 2007.

[105] H. J. Jung, Y. Song, S. Hong, C. Yang, S. Hwang, S. Jeong, and T. Sung , "Design and optimization of piezoelectric impact-based micro wind energy harvester for wireless sensor network," *Sensors Actuators A Phys.*, vol. 222, pp. 314–321, 2015.

[106] H. Liu, S. Zhang, R. Kathiresan, T. Kobayashi, and C. Lee, "Development of piezoelectric microcantilever flow sensor with wind-driven energy harvesting capability," *Appl. Phys. Lett.*, vol. 100, no. 22, pp. 2010–2013, 2012.

[107] X. He, Z. Shang, Y. Cheng, and Y. Zhu, "A micromachined low-frequency piezoelectric harvester for vibration and wind energy scavenging," *J. Micromechanics Microengineering*, vol. 23, no. 12, p. 125009, 2013.

[108] A. Bansal, D. A. Howey, and A. S. Holmes, "Cm-scale air turbine and generator for energy harvesting from low-speed flows," in *Proc. Solid-State Sensors, Actuators and Microsystems Conference (TRANSDUCERS)*, 2009, pp. 529–532.

[109] K. X. Wang, L. Bu, J. M. Chen, and L. Song, "Frequency-tunable airflow energy harvester using variable aperture helmholtz resonator and piezoelectric cantilever," in *Proc. Solid-State Sensors, Actuators and Microsystems (TRANSDUCERS)*, 2015, pp. 1945–1948.

[110] A. Flammini, D. Marioli, E. Sardini, and M. Serpelloni, "An autonomous sensor with energy harvesting capability for airflow speed measurements," in *Proc. IEEE Instrumentation and Measurement Technology Conference (I2MTC)*, 2010, pp. 892–897.

[111] X. Wu and D.-W. Lee, "An electromagnetic energy harvesting device based on high efficiency windmill structure for wireless forest fire monitoring application," *Sensors Actuators A Phys.*, vol. 219, pp. 73–79, 2014.

[112] X. Gao, W.-H. Shih, and W. Y. Shih, "Flow energy harvesting using piezoelectric cantilevers with cylindrical extension," *Ind. Electron. IEEE Trans.*, vol. 60, no. 3, pp. 1116–1118, 2013.

[113] S. Priya, "Modeling of electric energy harvesting using piezoelectric windmill," *Appl. Phys. Lett.*, vol. 87, no. 18, p. 184101, 2005.

[114] D. Carli, D. Brunelli, D. Bertozzi, and L. Benini, "A high-efficiency wind-flow energy

harvester using micro turbine," in *Proc. Power electronics electrical drives automation and motion (SPEEDAM)*, 2010, pp. 778–783.

[115] Y. Wang, L. Wang, T. Cheng, Z. Song, and F. Qin, "Sealed piezoelectric energy harvester driven by hyperbaric air load," *Appl. Phys. Lett.*, vol. 108, no. 3, p. 33902, 2016.

[116] D. J. Li *et al.*, "Polymer piezoelectric energy harvesters for low wind speed," *Appl. Phys. Lett.*, vol. 104, no. 1, p. 12902, 2014.

[117] X. Zhao, Z. Shang, G. Luo, and L. Deng, "A vibration energy harvester using AlN piezoelectric cantilever array," *Microelectron. Eng.*, vol. 142, pp. 47–51, 2015.

[118] F. Pan and T. Samaddar, *Charge pump circuit design*. McGraw Hill Professional, 2006.

[119] R. N. Torah, M. J. Tudor, K. Patel, I. N. Garcia, and S. P. Beeby, "Autonomous low power microsystem powered by vibration energy harvesting," in *Sensors, 2007 IEEE*, 2007, pp. 264–267.

[120] A. Zargarani and N. Mahmoodi, "Investigating Piezoelectric Energy Harvesting Circuits for Piezoelectric Flags," in *ASME 2015 Conference on Smart Materials, Adaptive Structures and Intelligent Systems*, 2015.

[121] Y. K. Tan and S. K. Panda, "Optimized wind energy harvesting system using resistance emulator and active rectifier for wireless sensor nodes," *Power Electron. IEEE Trans.*, vol. 26, no. 1, pp. 38–50, 2011.

[122] K. Niazi and M. Goudarzi, "Pyroelectric effect in PZT and PMN-0.25 PT ceramics for hybrid energy harvesting in different interface circuits," *Ger. J. Renew. Sustain. Energy Res.*, vol. 1, no. 1, 2015.

[123] G. Shi, Y. Xia, Y. Ye, L. Qian, and Q. Li, "An efficient self-powered synchronous electric charge extraction interface circuit for piezoelectric energy harvesting systems," *J. Intell. Mater. Syst. Struct.*, 2016.

[124] L. Zhao and Y. Yang, "Analytical solutions for galloping-based piezoelectric energy harvesters with various interfacing circuits," *Smart Mater. Struct.*, vol. 24, no. 7, p. 75023, 2015.

[125] J. Wei, S. Risquez, H. Mathias, E. Lefeuvre, and F. Costa, "Simple and efficient interface circuit for vibration electrostatic energy harvesters," in *Proc. IEEE SENSORS*, 2015, pp. 1–4.

[126] "Linear Technology." [Online]. Available: http://www.linear.com. [Accessed: 10-Dec-2018].

[127] "Infinit Power Solutions." [Online]. Available: http://www.cytech.com/products-ips.

[128] Y. Jia and A. A. Seshia, "Power optimization by mass tuning for MEMS piezoelectric cantilever vibration energy harvesting," *J. Microelectromechanical Syst.*, vol. 25, no. 1, pp. 108–117, 2016.

[129] D. S. Ibrahim, A. G. A. Muthalif, N. H. D. Nordin, and T. Saleh, "Comparative study of conventional and magnetically coupled piezoelectric energy harvester to optimize output voltage and bandwidth," *Microsyst. Technol.*, pp. 1–12, 2016.

[130] S. Sunithamani, P. Lakshmi, and E. E. Flora, "PZT length optimization of MEMS piezoelectric energy harvester with a non-traditional cross section: simulation study," *Microsyst. Technol.*, vol. 20, no. 12, pp. 2165–2171, 2014.

[131] G. Sordo, E. Serra, U. Schmid, and J. Iannacci, "Optimization method for designing multimodal piezoelectric MEMS energy harvesters," *Microsyst. Technol.*, vol. 22, no. 7, pp. 1811–1820, 2016.

[132] S. M. K. Tabatabaei, S. Behbahani, and P. Rajaeipour, "Multi-objective shape design optimization of piezoelectric energy harvester using artificial immune system," *Microsyst. Technol.*, pp. 1–12, 2015.

[133] S. Nabavi and L. Zhang, "MEMS piezoelectric energy harvester design and optimization based on Genetic Algorithm," in *Proc. IEEE Ultrasonics Symposium (IUS)*, 2016, pp. 1–4.

[134] J. Kim, S. Park, W. Lim, J. Jang, T.H. Lee, Y. Song, "Design Optimization of PZT-Based Piezoelectric Cantilever Beam by Using Computational Experiments," *J. Electron. Mater.*, pp. 1–11, 2016.

[135] G. Ye, J. Yan, Z. J. Wong, K. Soga, and A. Seshia, "Optimisation of a piezoelectric system for energy harvesting from traffic vibrations," in *Proc. IEEE Ultrasonics Symposium (IUS)*, 2009, pp. 759–762.

[136] A. L. Araújo, V. S. Carvalho, C. M. M. Soares, J. Belinha, and A. J. M. Ferreira, "Vibration analysis of laminated soft core sandwich plates with piezoelectric sensors and actuators," *Compos. Struct.*, 2016.

[137] N. Chidambaram, A. Mazzalai, and P. Muralt, "Measurement of effective piezoelectric coefficients of PZT thin films for energy harvesting application with interdigitated electrodes," *IEEE Trans. Ultrason. Ferroelectr. Freq. Control*, vol. 59, no. 8, pp. 1624–1631, 2012.

[138] A. H. Meitzler, H. F. Tiersten, A. W. Warner, D. Berlincourt, G. A. Couqin, and F. S. Welsh III, "IEEE standard on piezoelectricity." Society, 1988.

[139] P. Janphuang, R. Lockhart, N. Uffer, D. Briand, and N. F. de Rooij, "Vibrational piezoelectric energy harvesters based on thinned bulk PZT sheets fabricated at the wafer level," *Sensors Actuators A Phys.*, vol. 210, pp. 1–9, 2014.

[140] J. I. Daniel, "Engineering vibration." Prentice-Hall, Inc., New Jersey, 2001.

[141] T. Eggborn, "Analytical models to predict power harvesting with piezoelectric materials," 2003.

[142] S.-H. Kim, J.-H. Ahn, H.-M. Chung, and H.-W. Kang, "Analysis of piezoelectric effects on various loading conditions for energy harvesting in a bridge system," *Sensors Actuators A*

Phys., vol. 167, no. 2, pp. 468–483, 2011.

[143] R. C. Hibbeler, "Mechanics of Materials, 1997." Prentice Hall.

[144] A. L. Herrera-May *et al.*, "Analytical modeling for the bending resonant frequency of sensors based on micro and nanoresonators with complex structural geometry," *IEEE Sens. J.*, vol. 11, no. 6, pp. 1361–1374, 2011.

[145] L. G. Villanueva, R. B. Karabalin, M. H. Matheny, D. Chi, J. E. Sader, and M. L. Roukes, "Nonlinearity in nanomechanical cantilevers," *Phys. Rev. B*, vol. 87, no. 2, p. 24304, 2013.

[146] S. Kumar, R. Srivastava, and R. K. Srivastava, "Design and analysis of smart piezo cantilever beam for energy harvesting," *Ferroelectrics*, vol. 505, no. 1, pp. 159–183, 2016.

[147] M. Mitchell, *An introduction to genetic algorithms*. MIT press, 1998.

[148] A. E. Eiben and J. E. Smith, *Introduction to evolutionary computing*, vol. 53. Springer, 2003.

[149] S. Nabavi and L. Zhang, "Design and Optimization of Wideband Multimode Piezoelectric MEMS Vibration Energy Harvesters," in *Proc. Eurosesnosors, Paris, France*, 2017, vol. 1, no. 4, p. 586.

[150] "COMSOL Optimization Module." [Online]. Available: https://www.comsol.com/optimization-module. [Accessed: 10-Apr-2017].

[151] N. A. Kong, D. S. Ha, A. Erturk, and D. J. Inman, "Resistive impedance matching circuit for piezoelectric energy harvesting," *J. Intell. Mater. Syst. Struct.*, 2010.

[152] S. Roundy, P. K. Wright, and J. Rabaey, "A study of low level vibrations as a power source for wireless sensor nodes," *Comput. Commun.*, vol. 26, no. 11, pp. 1131–1144, 2003.

[153] L. M. Miller, E. Halvorsen, T. Dong, and P. K. Wright, "Modeling and experimental verification of low-frequency MEMS energy harvesting from ambient vibrations," *J. Micromechanics Microengineering*, vol. 21, no. 4, p. 45029, 2011.

[154] A. Cammarano, S. A. Neild, S. G. Burrow, and D. J. Inman, "The bandwidth of optimized nonlinear vibration-based energy harvesters," *Smart Mater. Struct.*, vol. 23, no. 5, p. 55019, 2014.

[155] D. Shen, J.-H. Park, J. Ajitsaria, S.-Y. Choe, H. C. Wikle III, and D.-J. Kim, "The design, fabrication and evaluation of a MEMS PZT cantilever with an integrated Si proof mass for vibration energy harvesting," *J. Micromechanics Microengineering*, vol. 18, no. 5, p. 55017, 2008.

[156] R. Sriramdas and R. Pratap, "Scaling and Performance Analysis of MEMS Piezoelectric Energy Harvesters," *J. Microelectromechanical Syst.*, vol. 26, no. 3, pp. 679-690 2017.

[157] X. Li, W. Y. Shih, I. A. Aksay, and W.-H. Shih, "Electromechanical Behavior of PZT-Brass Unimorphs," *J. Am. Ceram. Soc.*, vol. 82, no. 7, pp. 1733–1740, 1999.

[158] S. Priya and D. J. Inman, *Energy harvesting technologies*, vol. 21. Springer, 2009.

[159] W. Thomson, *Theory of vibration with applications*. CRC Press, 1996.

[160] S. Du *et al.*, "A new electrode design method in piezoelectric vibration energy harvesters to maximize output power," *Sensors Actuators A Phys.*, vol. 263, pp. 693–701, 2017.

[161] "Virginia Semiconductor Inc." [Online]. Available: https://www.virginiasemi.com.

[162] Y. Jia and A. A. Seshia, "Five topologies of cantilever-based mems piezoelectric vibration energy harvesters: a numerical and experimental comparison," *Microsyst. Technol.*, vol. 22, no. 12, pp. 2841–2852, 2016.

[163] R. Andosca *et al.*, "Experimental and theoretical studies on MEMS piezoelectric vibrational energy harvesters with mass loading," *Sensors Actuators A Phys.*, vol. 178, pp. 76–87, 2012.

[164] S. Nabavi and L. Zhang, "Design and Optimization of Piezoelectric MEMS Vibration Energy Harvesters Based on Genetic Algorithm," *IEEE Sens. J.*, vol. 17, no. 22, pp. 7372–7382, 2017.

[165] Y. Tsujiura, E. Suwa, T. Nishi, F. Kurokawa, H. Hida, and I. Kanno, "Airflow energy harvester of piezoelectric thin-film bimorph using self-excited vibration," *Sensors Actuators A Phys.*, vol. 261, pp. 295–301, 2017.

[166] W. G. Li, S. He, and S. Yu, "Improving power density of a cantilever piezoelectric power harvester through a curved L-shaped proof mass," *IEEE Trans. Ind. Electron.*, vol. 57, no. 3, pp. 868–876, 2010.

[167] L. Gu, "Low-frequency piezoelectric energy harvesting prototype suitable for the MEMS implementation," *Microelectronics J.*, vol. 42, no. 2, pp. 277–282, 2011.

[168] R. Xu and S. G. Kim, "Low-frequency, low-G MEMS piezoelectric energy harvester," in *Journal of Physics: Conference Series*, 2015, vol. 660, no. 1, p. 12013.

[169] Y. Jia, S. Du, and A. A. Seshia, "Micromachined cantilevers-on-membrane topology for broadband vibration energy harvesting," *J. Micromechanics Microengineering*, vol. 26, no. 12, p. 124007, 2016.

[170] R. Elfrink *et al.*, "Vacuum-packaged piezoelectric vibration energy harvesters: damping contributions and autonomy for a wireless sensor system," *J. Micromechanics Microengineering*, vol. 20, no. 10, p. 104001, 2010.

[171] M. Wahbah, M. Alhawari, B. Mohammad, H. Saleh, and M. Ismail, "An AC--DC converter for human body-based vibration energy harvesting," *Microelectronics J.*, vol. 55, pp. 1–7, 2016.

[172] A. D. Schlichting, E. Fink, and E. Garcia, "A low-loss hybrid rectification technique for piezoelectric energy harvesting," *Smart Mater. Struct.*, vol. 22, no. 9, p. 95028, 2013.

[173] S. Du, Y. Jia, C. D. Do, and A. A. Seshia, "An Efficient SSHI Interface With Increased Input Range for Piezoelectric Energy Harvesting Under Variable Conditions," *IEEE J. Solid-State Circuits*, 2016.

[174] W. F. Stokey, "Vibration of systems having distributed mass and elasticity," *Shock Vib. Handb.*, pp. 1–7, 1988.

[175] "MEMSCAP." [Online]. Available: www.memscap.com. [Accessed: 10-Dec-2018].

[176] R. Gao, Y. Huang, X. Wen, J. Zhao, and S. Liu, "Method to further improve sensitivity for high order vibration mode mass sensors with stepped cantilevers," *Sensors*, vol. 17874, no. R1, p. 1, 2017.

[177] S. Nabavi and L. Zhang, "Frequency tuning and efficiency improvement of piezoelectric MEMS vibration energy harvesters," *J. Microelectromechanical Syst.*, vol. 28, no. 1, pp. 77-87, 2019.

[178] H. S. Kim, J.-H. Kim, and J. Kim, "A review of piezoelectric energy harvesting based on vibration," *Int. J. Precis. Eng. Manuf.*, vol. 12, no. 6, pp. 1129–1141, 2011.

[179] A. Abdelkefi, N. Barsallo, L. Tang, Y. Yang, and M. R. Hajj, "Modeling, validation, and performance of low-frequency piezoelectric energy harvesters," *J. Intell. Mater. Syst. Struct.*, vol. 25, no. 12, pp. 1429–1444, 2014.

[180] J.-Q. Liu *et al.*, "A MEMS-based piezoelectric power generator array for vibration energy harvesting," *Microelectronics J.*, vol. 39, no. 5, pp. 802–806, 2008.

[181] Z. Xiao, T. qing Yang, Y. Dong, and X. cai Wang, "Energy harvester array using piezoelectric circular diaphragm for broadband vibration," *Appl. Phys. Lett.*, vol. 104, no. 22, p. 223904, 2014.

[182] H. Liu, C. J. Tay, C. Quan, T. Kobayashi, and C. Lee, "Piezoelectric MEMS energy harvester for low-frequency vibrations with wideband operation range and steadily increased output power," *Microelectromechanical Syst. J.*, vol. 20, no. 5, pp. 1131–1142, 2011.

[183] W. Zhou, G. R. Penamalli, and L. Zuo, "An efficient vibration energy harvester with a multi-mode dynamic magnifier," *Smart Mater. Struct.*, vol. 21, no. 1, p. 15014, 2011.

[184] L. Dhakar, H. Liu, F. E. H. Tay, and C. Lee, "A new energy harvester design for high power output at low frequencies," *Sensors Actuators A Phys.*, vol. 199, pp. 344–352, 2013.

[185] R. L. Harne and K. W. Wang, "A review of the recent research on vibration energy harvesting via bistable systems," *Smart Mater. Struct.*, vol. 22, no. 2, p. 23001, 2013.

[186] Q. Tang and X. Li, "Two-stage wideband energy harvester driven by multimode coupled vibration," *IEEE/ASME Trans. Mechatronics*, vol. 20, no. 1, pp. 115–121, 2015.

[187] M. Rezaeisaray, M. El Gowini, D. Sameoto, D. Raboud, and W. Moussa, "Low frequency piezoelectric energy harvesting at multi vibration mode shapes," *Sensors Actuators A Phys.*, vol. 228, pp. 104–111, 2015.

[188] S. Nabavi and L. Zhang, "Design and optimization of MEMS piezoelectric energy harvesters for improved efficiency," in *Proc. IEEE SENSORS*, 2017, pp. 1–3.

[189] S. D. Senturia, *Microsystem design*. Springer Science & Business Media, 2007.

[190] W. Zhang, R. Baskaran, and K. L. Turner, "Effect of cubic nonlinearity on auto-parametrically amplified resonant MEMS mass sensor," *Sensors Actuators A Phys.*, vol. 102, no. 1, pp. 139–150, 2002.

[191] K. Deb and H. Jain, "An evolutionary many-objective optimization algorithm using reference-point-based nondominated sorting approach, part I: Solving problems with box constraints.," *IEEE Trans. Evol. Comput.*, vol. 18, no. 4, pp. 577–601, 2014.

[192] A. Konak, D. W. Coit, and A. E. Smith, "Multi-objective optimization using genetic algorithms: A tutorial," *Reliab. Eng. Syst. Saf.*, vol. 91, no. 9, pp. 992–1007, 2006.

[193] "COMSOL Multiphysics." [Online]. Available: https://www.comsol.com/. [Accessed: 10-Apr-2018].

[194] M. Rezaeisaray, "Investigation of Potential Platforms for Low Frequency MEMS-based Piezoelectric Energy Harvesting,", PhD Thesis, University of Alberta, 2014.

[195] H.-C. Song *et al.*, "Ultra-Low Resonant Piezoelectric MEMS Energy Harvester With High Power Density," *J. Microelectromechanical Syst.*, vol. 26, no. 6, pp. 1226–1234, 2017.

[196] D. S. Nguyen, E. Halvorsen, G. U. Jensen, and A. Vogl, "Fabrication and characterization of a wideband MEMS energy harvester utilizing nonlinear springs," *J. Micromechanics Microengineering*, vol. 20, no. 12, p. 125009, 2010.

[197] Y. Zhang, T. Wang, A. Luo, Y. Hu, X. Li, and F. Wang, "Micro electrostatic energy harvester with both broad bandwidth and high normalized power density," *Appl. Energy*, vol. 212, pp. 362–371, 2018.

[198] H. Liu, Y. Qian, and C. Lee, "A multi-frequency vibration-based MEMS electromagnetic energy harvesting device," *Sensors Actuators A Phys.*, vol. 204, pp. 37–43, 2013.

[199] D. Mallick, A. Amann, and S. Roy, "A nonlinear stretching based electromagnetic energy harvester on FR4 for wideband operation," *Smart Mater. Struct.*, vol. 24, no. 1, p. 15013, 2014.

[200] N. Wang *et al.*, "AlN wideband energy harvesters with wafer-level vacuum packaging utilizing three-wafer bonding," in *Proc. IEEE Micro Electro Mechanical Systems (MEMS)*, , 2017, pp. 841–844.

[201] S. Leadenham and A. Erturk, "Nonlinear M-shaped broadband piezoelectric energy harvester for very low base accelerations: primary and secondary resonances," *Smart Mater. Struct.*, vol. 24, no. 5, p. 55021, 2015.

[202] E. E. Aktakka and K. Najafi, "Three-axis piezoelectric vibration energy harvester," in *Proc. IEEE Micro Electro Mechanical Systems (MEMS)*, 2015, pp. 1141–1144.

[203] H. Liu, C. Lee, T. Kobayashi, C. J. Tay, and C. Quan, "Piezoelectric MEMS-based wideband energy harvesting systems using a frequency-up-conversion cantilever stopper,"

Sensors Actuators A Phys., vol. 186, pp. 242–248, 2012.

[204] J.-H. Park, M. S. Myung, and Y.-J. Kim, "Tensile and high cycle fatigue test of Al--3% Ti thin films," *Sensors Actuators A Phys.*, vol. 147, no. 2, pp. 561–569, 2008.

[205] "COMSOL Fatigue Module." [Online]. Available: https://www.comsol.com/fatigue-module. [Accessed: 10-Jun-2018].

Appendix: List of Publications

Journal Publications

[1] S. Nabavi and L. Zhang, "Portable Wind Energy Harvesters for Low Power Applications: A Survey", *Sensors*, vol. 16, no. 7, pp. 1101, 2016.

[2] S. Nabavi and L. Zhang. "Design and Optimization of Piezoelectric MEMS Vibration Energy Harvesters Based on Genetic Algorithm", *IEEE Sensors Journal*, vol. 17, pp.7372-7382, 2017.

[3] S. Nabavi and L. Zhang, "Frequency tuning and efficiency improvement of piezoelectric MEMS vibration energy harvesters," *J. Microelectromechanical Syst.*, vol. 28, no. 1, pp. 77-87, 2019.

[4] S. Nabavi and L. Zhang, "Nonlinear Multi-mode Wideband Piezoelectric MEMs Vibration Energy Harvester", *IEEE Sensors Journal*, (in press)

[5] S. Nabavi and L. Zhang. "T-shaped Piezoelectric Structure for High-performance MEMS Vibration Energy Harvesting", *IEEE/ASME Journal of Microelectromechanical Systems (JMEMS)*, (major revision submited).

Conference Publications

[1] S. Nabavi and L. Zhang, "MEMS piezoelectric energy harvester design and optimization based on Genetic Algorithm," in *Proc. IEEE International Ultrasonics Symposium (IUS)*, pp. 1–4. Tours, France, Sept. 2016.

[2] S. Nabavi and L. Zhang, "Design and Optimization of Wideband Multimode Piezoelectric MEMs Vibration Energy Harvesters," in *Proc. 31st Eurosensors,* pp. 586-590, Paris, France, Sept. 2017.

[3] S. Nabavi and L. Zhang, "Design and Optimization of MEMS Piezoelectric Energy Harvesters for Improved Efficiency", in *Proc. 16th IEEE SENSORS*, pp. 1–3, Glasgow, UK, Nov. 2017.

[4] S. Nabavi, A. Aljaroudi, L. Zhang, "T-shaped Piezoelectric MEMS Vibration Harvester with Integration of Highly Efficient Power Management System", in *Proc. 17th PowerMEMS,* vol. 1052, pp. 1202, Kanazawa, Japan, Nov. 2017.

[5] S. Nabavi and L. Zhang, "Design and Optimization of a Low-Resonant-Frequency Piezoelectric MEMS Energy Harvester Based on Artificial Intelligence" in *Proc. 32nd Eurosensors,* Graz, Austria, Sept. 2018.

[6] S. Nabavi and L. Zhang, "Curve-shaped Anchor for Durability and Efficiency Improvement of Piezoelectric MEMS Energy Harvesters", in *Proc. 17th IEEE SENSORS*, New Delhi, India, Oct. 2018.

Patent Applications

[1] L. Zhang and S. Nabavi, "Wideband Piezoelectric Vibratory MEMS Harvester", US Patent Application, No. 62/666,984, filed on May 5, 2018.

[2] L. Zhang and S. Nabavi, "Self-powered T-shaped Micro-cantilever Piezoelectric Biosensor", US Patent Application, (under review)